Institut für Energie- und Klimaforschung
Plasmaphysik (IEK-4)

Development and evaluation of a synthetic helium beam diagnostic for Wendelstein 7-X

Wladimir Zholobenko, Michael Rack, Detlev Reiter

Jül-4407

Mitglied der Helmholtz-Gemeinschaft

JÜLICH
Forschungszentrum

Institut für Energie- und Klimaforschung
Plasmaphysik (IEK-4)

Development and evaluation of a synthetic helium beam diagnostic for Wendelstein 7-X

Wladimir Zholobenko, Michael Rack, Detlev Reiter

Berichte des Forschungszentrums Jülich
Jül-4407 · ISSN 0944-2952
Institut für Energie- und Klimaforschung
Plasmaphysik (IEK-4)

Vollständig frei verfügbar über das Publikations-
portal des Forschungszentrums Jülich (JuSER)
unter www.fz-juelich.de/zb/openaccess

Forschungszentrum Jülich GmbH · 52425 Jülich
Zentralbibliothek, Verlag
Tel.: 02461 61-5220 · Fax: 02461 61-6103
zb-publikation@fz-juelich.de
www.fz-juelich.de/zb

Abstract

We report on recent advancements of the synthetic diagnostic module in the post processing part of of the 3D kinetic (neutral particle) transport code EIRENE (www.eirene.de). We also review and upgrade the underlying atomic helium data base, resorting to the most recent version of the Goto-Fujimoto collisional radiative helium code and a recommended reference cross section data set from an internationally coordinated (IAEA) evaluation activity.

Using both the upgraded transport code and data base, we then simulate the penetration of and radiation from helium used for beam emission spectroscopy, exemplarily for the configurational set up at the Wendelstein 7-X stellarator. This allows to analyse and evaluate the application of the diagnostic in different plasma backgrounds and with different atomic models. We simulate fully 3D resolved edge plasma backgrounds with the fluid edge plasma Monte Carlo code in three dimensions (EMC3) coupled to EIRENE. The sensitivity of the entire diagnostic concept to the underlying atomic data set, which is the key for a quantitative determination of electron density and temperature profiles, is discussed.

Keywords: synthetic diagnostic, He beam, collisional-radiative model, EIRENE code, Wendelstein 7-X

Contents

1 Introduction

This report aims at improving the helium beam emission spectroscopy (BES) [3] – an active (invasive) diagnostic for the determination of electron density and temperature in the plasma edge of magnetic fusion devices. Before it is completely ionized, neutral helium can penetrate several centimeters into the plasma [5] because of the high ionization potential (24.6 eV). The experimental setup is described in [6]. It is possible to obtain a high spatial and temporal resolution of the emitted radiation. The determination of plasma parameters from helium line emission, however, strongly relies on the available collisional-radiative model (CRM or CR model) and the underlying raw atomic collision cross section data in it.

A CRM consists of a set of coupled rate equations (1) for the electronic state population density distribution of one or multiple, atomic or molecular species coupled to a plasma. Thereby, it determines the collisional-radiative balance for given plasma parameters. The radiation emission profile for any transition line then depends on the local population density distribution. It is often possible to reverse the calculation and to determine the plasma parameters from spectroscopic measurements: we have to observe atomic transitions for which the model is bijective in the parameter range of interest.

For a CRM, atomic properties must be measured or calculated quantum-mechanically. These are e.g. energy levels, transition rates between them and ionization rates. However, taking as much as possible into account increases the complexity. A trade-off must be found between completeness and convenience which results in multiple approximations. CRMs heavily rely on the available atomic data and the approximations made in their processing.

Validation of a CRM against experiments is complicated firstly due to the often non-homogeneous, sometimes even instationary plasma conditions, but also due to uncertainty in both the underlying atomic data and the measured parameters. Our approach is to implement a synthetic diagnostic in the established 3D transport code package EMC3-EIRENE. This allows to test the CR model on a well characterized, simulated background plasma.

There exist comprehensive CRMs for helium for quite some time, probably starting with the pioneering work of Takashi Fujimoto 1979, so that we do not have to compile our own database. Decades ago, meta-stable state resolved condensed effective rate coefficients have already been produced by Fujimoto's CR code [2] (a program which solves the CRM numerically) and, in the eighties of the last century, these have been parametrized for the EIRENE [7] code – a Monte Carlo neutral particle transport solver. We will refer to this atomic data set as F1979. But Fujimoto's calculation was originally meant for a positive-column plasma and did not include magnetic field effects. A revised and upgraded helium CR model and code were published by Goto [1] – referred to as G2012, because the latest code version stems from 2012. It includes recent, internationally evaluated atomic cross section data and the singlet-triplet state mixing due to the spin-orbit interaction. The CR model is described in section 2. Section 3 deals with the underlying atomic database. The magnetic field dependence, as a result of the state mixing, is investigated in section 4.

The results of the CR model, so called collisional-radiative rates, can be compared and utilized by the HYDKIN web page [8] – an online atomic database and solver for reaction kinetics publicly exposing and processing all the atomic/molecular data used in EIRENE. This is the topic of section 5. The individual atomic data used by Goto's code were also made directly accessible for that web page and its online CR-equilibrium solver.

Since EIRENE is often coupled to plasma fluid codes (like B2 [9] or EMC3 [10]), we are interested in the plasma response to the neutrals. This is described in section 6.

Historically different CR models are applied in different experiments. For our synthetic diagnostic tool to be directly comparable to real experimental, we study the observables resulting from G2012 in section 7 - these are line intensity ratios as functions of plasma parameters. A comparison to those obtained in an earlier model, also derived from Fujimotos original work, by Brix [3] is given. We also study how line intensity ratios change if we select different atomic databases or alter the CR model approximations.

Section 8 describes the simulation of the helium beam in EIRENE. In contrast to the experimental application of the CR model, a synthetic diagnostic can be tested on a simulated plasma background. Many effects affecting the diagnostic can be taken into account one by one, such as 3D transport, non-equilibrated meta-stable states, or opacity.

Finally, section 9 describes the implementation of the synthetic diagnostic. An algorithm is presented which utilizes the synthetic diagnostic to evaluate the application of the diagnostic in specific conditions at Wendelstein 7-X (W7-X) in Greifswald – currently the worlds largest, optimized stellarator experiment.

2 Collisional-radiative model

This chapter mostly builds on [1] and [11]. The starting point for this present work is the set of linear ordinary differential equations (ODEs)

$$\frac{\mathrm{d}n(p)}{\mathrm{d}t} = -\left\{\sum_{q\neq p} C(p,q)n_\mathrm{e} + \sum_{q<p} A(p,q) + S(p)n_\mathrm{e}\right\} n(p) + \sum_{q\neq p}\{C(q,p)n_\mathrm{e} + A(q,p)\}\, n(q) + \{\alpha(p)n_\mathrm{e} + \beta(p) + \beta_\mathrm{d}(p)\}\, n_\mathrm{i}n_\mathrm{e}. \quad (1)$$

It describes the temporal change of the population density of neutral helium. $n(p)$ is the population density of a state $p = n^{2S+1}L$, determined by the principal quantum number n, spin S and angular momentum quantum number L. $q < p$ means that q lies energetically lower than p.

In these equations, $A(p,q)$ is the spontaneous transition probability from p to q (or Einstein's A coefficient), $C(p,q)$ and $S(p)$ are the rate coefficients for electron impact transition and ionization, and $\alpha(p)$, $\beta(p)$ and $\beta_\mathrm{d}(p)$ are the rate coefficients for three-body, radiative and dielectronic recombination, respectively. n_e is the electron density and n_i the hydrogen-like He^+ ion density. All rate coefficients (but not $A(p,q)$) have an electron temperature (T_e) dependency.

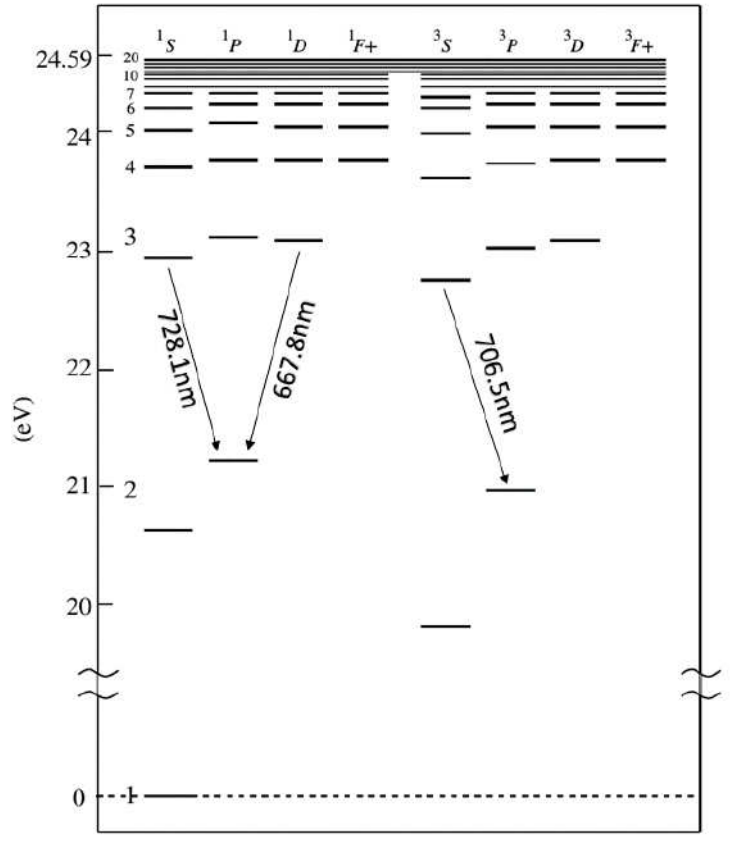

Figure 1: Energy level diagram of helium atom considered in the calculation. Lines used for the BES are implied. The labels $^{1,3}F+$ denote the levels which represent all the states with $L \geq 3$. Courtesy: [1].

In Figure 1 the energy level diagram is given. For convenience, only a limited number of levels is considered - which is however relatively large compared to [3]. In G2012 [1], levels up to $n = 26$ are included, whereby levels with $n \geq 21$ are assumed to be simply given by the Saha-Boltzmann equilibrium [2, eq. (3)]

$$n(p) = Z(p) n_\mathrm{i} n_\mathrm{e}, \qquad \text{where} \qquad Z(p) = \frac{g(p)}{2\omega_\mathrm{i}} \left(\frac{h^2}{2\pi m k_B T} \right)^{3/2} \exp\left(\frac{\chi(p)}{k_B T} \right). \tag{2}$$

There, $g(p)$ is the statistical weight of the level p, ω_i is the partition function of the ions, $\chi(p)$ is the ionization potential and other symbols as usual. Note: χ is related to the energy levels $E(p)$ in Figure 1 via $\chi(p) = 24.59\ \mathrm{eV} - E(p)$.

Several levels are grouped together: For small n, levels with $L \geq 3$ are bundled to a single level $F+$. For $n \geq 8$, the orbital quantum number is not resolved. The levels with $n \geq 11$ are approximated by the hydrogenic levels having statistical weights twice those of hydrogen. In total, there are 65 levels considered, 6 of which are given by (2).

The set is linear since a plasma background is assumed to be fixed: electron density n_e, electron temperature T_e, and hydrogenlike (helium) ion density n_i are taken to be externally given. The frequently employed normalisation to a constant total density, const $= n_{tot} = \sum n(p)$, summed over all states p, which produces a non-linear coupling between the p states, is also not made here. Therefore, with $p, q \in [1, 65]$, it can be written in vector notation as

$$\dot{\mathbf{n}} = \mathbf{M}(T_\mathrm{e}, n_\mathrm{e}) \cdot \mathbf{n} + \Gamma(T_\mathrm{e}, n_\mathrm{e}, n_\mathrm{i}), \quad \text{where} \tag{3}$$

$$\mathbf{M}_{pq} = \begin{cases} C(q,p) n_\mathrm{e} + A(q,p) & , \text{ if } p \neq q \\ -\sum\limits_{j \neq p} C(p,j) n_\mathrm{e} - \sum\limits_{j<p} A(p,j) - S(p) n_\mathrm{e} & , \text{ if } p = q \end{cases}$$

$$\text{and } \Gamma_p = [\alpha(p) n_\mathrm{e} + \beta(p) + \beta_\mathrm{d}(p)] \, n_\mathrm{i} n_\mathrm{e}.$$

2.1 Reducing the dimensionality

Equation (3) can be solved via e.g. eigenvalue decomposition or Laplace transformation. But in practice, the computational effort can be drastically reduced since the timescales for the development of different atomic states are very different. So, if diagnostics with finite temporal resolution are used, and no processes other than those in (1) are relevant on faster time scales, some of the states can be assumed stationary. The vector space of $\mathbf{n}$ can then be split in three,

$$\begin{pmatrix} \dot{\mathbf{n}}_P \\ \dot{\mathbf{n}}_Q \\ \dot{\mathbf{n}}_S \end{pmatrix} = \begin{pmatrix} \mathbf{M}_P & \mathbf{M}_{PQ} & \mathbf{M}_{PS} \\ \mathbf{M}_{QP} & \mathbf{M}_Q & \mathbf{M}_{QS} \\ \mathbf{M}_{SP} & \mathbf{M}_{SQ} & \mathbf{M}_S \end{pmatrix} \cdot \begin{pmatrix} \mathbf{n}_P \\ \mathbf{n}_Q \\ \mathbf{n}_S \end{pmatrix} + \begin{pmatrix} \Gamma_P \\ \Gamma_Q \\ \Gamma_S \end{pmatrix}, \tag{4}$$

where $\mathbf{n}_S$ is given by (2) and hence $\dot{\mathbf{n}}_S = 0$. We assume $\dot{\mathbf{n}}_Q = 0$ and immediately derive

$$\mathbf{n}_Q = -\mathbf{M}_Q^{-1} \left(\mathbf{M}_{QP} \mathbf{n}_P + \mathbf{M}_{QS} \mathbf{n}_S + \Gamma_Q \right), \tag{5}$$

$$\begin{aligned} \dot{\mathbf{n}}_P &= (\mathbf{M}_P - \mathbf{M}_{PQ} \mathbf{M}_Q^{-1} \mathbf{M}_{QP}) \mathbf{n}_P + (\mathbf{M}_{PS} - \mathbf{M}_{PQ} \mathbf{M}_Q^{-1} \mathbf{M}_{QS}) \mathbf{n}_S + \Gamma_P - \mathbf{M}_{PQ} \mathbf{M}_Q^{-1} \Gamma_Q \\ &= \mathbf{M}_\mathrm{eff} \mathbf{n}_P + \Gamma_\mathrm{eff}, \end{aligned} \tag{6}$$

which reduces the dimension of the ODE system to the dimension of the P space. In the last step we have used that both Γ and $\mathbf{n}_S$ are proportional to n_i and hence represent a source.

A more formal derivation is given in [12]. It yields a criterion for the validity of the CRM depending on the choice of the P and Q spaces.

2.2 Formulation I ("meta-stable resolved")

Taking only the ground and the two meta-stable states into the P space, hence assuming $\dot{n} = 0$ for all the other states, eq. (5) can be written for a state q as

$$\mathbf{n}_Q|_q = n(q) = r_0(q) n_\mathrm{e} n_\mathrm{i} + r_1(q) n_\mathrm{e} n(1^1S) + r_2(q) n_\mathrm{e} n(2^1S) + r_3(q) n_\mathrm{e} n(2^3S). \tag{7}$$

$r_j(q)$ are called population coefficients and depend on T_e and n_e. The subscripts $j \in \{0,1,2,3\}$ stand for the ion, the ground state 1^1S, and the meta-stable 2^1S and 2^3S states, respectively. For the P space, hence $p \in \{1,2,3\}$, eq. (6) becomes

$$\dot{\mathbf{n}}_P|_p = \frac{\mathrm{d}}{\mathrm{d}t} n(p) = \sum_{j \neq p, j \neq 0} k_{jp} n(j) n_\mathrm{e} - k_p n(p) n_\mathrm{e} + k_{0p} n_\mathrm{i} n_\mathrm{e}. \tag{8}$$

Notice that the constraint on ion density n_i in [1, eq. (25)] is only valid in a closed system. In EIRENE, it is usually additionally modified by plasma transport (on larger time scales) and other collision terms.

The k's are the CR coupling coefficients and are given explicitly in terms of the population coefficients in [1]. From (6) we see that $(\mathbf{M}_\mathrm{eff})_{pp} = -k_p n_\mathrm{e}$, $(\mathbf{M}_\mathrm{eff})_{pj} = k_{jp} n_\mathrm{e}$ and $\Gamma_\mathrm{eff}|_p = k_{0p} n_\mathrm{i} n_\mathrm{e}$.

2.3 Formulation II ("meta-stable unresolved")

If the quasi-steady-state (QSS) assumption also holds for the meta-stable states, they may be also moved into the Q space. The P space becomes one dimensional - it is the most simple choice. The excited level population is then given by

$$\mathbf{n}_Q|_q = n(q) = R_0(q) n_\mathrm{e} n_\mathrm{i} + R_1(q) n_\mathrm{e} n(1^1S). \tag{9}$$

$R_0(q)$ and $R_1(q)$ are also called population coefficients. They are associated with the recombining and the ionizing plasma component, respectively. The time evolution of the ground state is written in the reduced form as

$$\dot{\mathbf{n}}_P = \frac{\mathrm{d}}{\mathrm{d}t} n(1^1S) = -\frac{\mathrm{d}}{\mathrm{d}t} n_\mathrm{i} = -S_\mathrm{CR} n(1^1S) n_\mathrm{e} + \alpha_\mathrm{CR} n_\mathrm{i} n_\mathrm{e}. \tag{10}$$

S_CR and α_CR[†] are the CR ionization and recombination rate coefficients, respectively. S_CR, α_CR, $R_0(q)$ and $R_1(q)$ can be obtained directly from (5) and (6) or from k's and r's according to expressions given in [1, eq. (31-38)]. They are therefore functions of T_e and n_e.

2.4 Singlet–triplet wave function mixing

According to [1], corrections in the CR model due to mainly the spin–orbit interaction must be incorporated. The interaction leads to mixing between singlet and triplet fine-structure levels n^1L_L and n^3L_L. Their actual wave functions are expressed as

$$\Psi(n^1L_L) = \sqrt{1-\omega^2}\Psi^0(n^1L_L) - \omega\Psi^0(n^3L_L), \tag{11}$$

$$\Psi(n^3L_L) = \omega\Psi^0(n^1L_L) - \sqrt{1-\omega^2}\Psi^0(n^3L_L), \tag{12}$$

where Ψ^0 denotes the wave function for the pure $L-S$ fine-structure level. The mixing coefficient ω, calculated by [13], is significant for levels with $L \geq 3$. For these levels, the $L-S$

[†]Note that α_CR contains all recombination processes, not only the three-body recombination.

coupling scheme is inappropriate and the $j-j$ scheme should be used instead.

However, Goto enables us to stick to the established $L-S$ scheme by approximately manipulating the transition rate coefficients instead. For example, the ionization rate coefficient becomes

$$S(n^1L) = (1-\omega^2)S^0(n^1L) + \omega^2 S^0(n^3L), \tag{13}$$

$$S(n^3L) = \frac{\omega^2}{3}S^0(n^1L) + \left(1-\frac{\omega^2}{3}\right)S^0(n^3L). \tag{14}$$

Since $\omega = \omega(B)$, the rate coefficients become functions of the magnetic field. The consequences will be discussed in subsequent chapters.

2.5 Density and temperature validity range

The initial atomic data (reaction rate coefficients) depend only on temperature. The density dependence in the CR coefficients appears because of the reduction of the CR model dimension. Hence, as long as the required assumptions are valid, there is no limited density range for the model. However, at small and at high densities, it is reasonable to simplify the model by assuming an equilibrium - which is density independent. A detailed description of different equilibria is given in [14].

At lower density, $n_e \lesssim 10^{14}$ m^{-3}, three body recombination is negligible, so that electron impact ionization is balanced by radiative recombination. Radiative decay is the only significant de-excitation process, balancing electron impact excitation. This leads to the so called corona equilibrium, which is also present in the corona of the sun. In fact, at low enough densities CR coupling coefficients are found to automatically collapse to these corona values, constant in n_e.

On the other hand, at higher density, $n_e >> 10^{22}$ m^{-3}, radiative processes can be neglected. This also leads to a density independent equilibrium, the local thermal equilibrium (LTE). Typically (e.g. for hydrogen), CR coefficients are stored for 10^{14} m$^{-3} < n_e < 10^{22}$ m^{-3}, and a constant density dependence is assumed outside of the interval. While this is true at small densities, we still observe a significant density dependence around 10^{22} m^{-3} – hence, thermal equilibrium is still not reached there. According to [15, eq. (4.2.6), page 122], the necessary condition for LTE in a transparent plasma is $n_e[\text{cm}^{-3}] \geqq 1.4\cdot 10^{14}\sqrt{k_B T[\text{eV}]}\chi[\text{eV}]^3$. Its scaling with the third power of the ionization potential χ may explain why LTE is reached at higher densities for helium than for hydrogen. However, according to the formula, LTE for hydrogen at $n_e \gtrsim 10^{22}$ m^{-3} is only established at $T \lesssim 0.8$ meV, indicating that this estimate may be too restrictive.

The temperature validity range of the utilized CR model is difficult to specify, because it contains many atomic data from different sources. Their individual validity range must not overlap and we have no quality measure for the used extrapolations. In [1], the model is used for $T_e \in [0.1, 10^4]$ eV. However, electron impact transition cross sections are imprecise at $\lesssim 0.1$ eV (see chapter 3.2.3). Therefore, caution is recommended in the low temperature range.

In [1], no error margins are specified. This is unfortunate for experimental application. But, consequently, we also made no attempts to propagate uncertainties in EIRENE simulations in this present work. Nevertheless, error propagation from F1979 [2] to G2012 [1] by sensitivity analysis implemented in HYDKIN [8] is the topic of chapter 7.5.

3 Atomic data and database selection

3.1 Elementary processes

In this section, the underlying atomic processes for the CR model (1) are briefly explained, referring to [11]. The collection of data describing these processes quantitatively is subject of chapter 3.2.

Note that two different notations are in use. In brackets, we adopt the spectroscopic notation from [1]: $(q,p) = (q \to p)$ means a transition from q to p. In subscripts, we use the algebraic notation: $x_{pq} = x(q \to p)$, with an arbitrary quantity x dependent on that transition. If an electronic state p lies energetically higher than state q, we denote it by $p > q$. The excitation from q to p can be denoted by $\nearrow$ or $\nwarrow$, and the inverse de-excitation by $\searrow$ or $\swarrow$.

3.1.1 Spontaneous emission

Spontaneous emission can be understood as stimulated by electromagnetic vacuum fluctuations. Therefore, the decay rate (or Einstein's A coefficient) from a state p into state q,

$$A(p \searrow q) = \frac{2\omega_{qp}^3}{3h\varepsilon_0 c^3} g(q) d_{qp}^2, \tag{15}$$

mainly depends on the electric dipole matrix element (or dipole moment)

$$\mathbf{d}_{qp} = \langle p|\text{-}e\mathbf{r}|q\rangle = \text{-}e \int \Psi_p^*(\mathbf{r})\mathbf{r}\Psi_q(\mathbf{r}) d^3r. \tag{16}$$

Here, Ψ_q and Ψ_p are wave functions and $\mathbf{r}$ is the position vector. ω_{qp} is the angular frequency of the emitted radiation. $g(q)$ is the statistical weight of level q, and other symbols as usual.

Often, a dimensionless parameter is used to characterize the coupling of the atom to electromagnetic radiation - the oscillator strength

$$f_{qp} = \frac{8\pi^2 m_{\text{He}}}{3h^2 e^2} \Delta E_{qp} g(q) \mathbf{d}_{qp}^2. \tag{17}$$

m_{He} is the mass of the helium atom and $\Delta E_{pq} = |\chi(p) - \chi(q)| = \Delta E_{qp}$ is the energy difference between the state p and q.

3.1.2 Collisional processes

All other processes in the considered CR model can be regarded as electron collisions. Hence, they can be described by collisional cross sections

$$\sigma_{pq}(E) = \frac{2\pi}{\hbar} \frac{V}{v} \rho(E) \, |\langle q|H|p\rangle|^2 \tag{18}$$

according to Fermi's golden rule [16]. Here, $\rho(E)$ is the phase space density, H the interaction Hamiltonian and V the normalization volume. v is the relative velocity of colliding particles, but for He-e^- collisions the helium velocity is typically negligible. Therefore, $E = \frac{1}{2} m_e v^2$ is the kinetic energy of the electron.

For a Maxwellian velocity distribution of the electrons

$$f_M(v) = 4\pi v^2 \left(\frac{m}{2\pi k_B T}\right)^{3/2} \exp\left(-\frac{mv^2}{2k_B T}\right), \tag{19}$$

the rate coefficients are computed by averaging according to

$$\langle \sigma v \rangle (T) = \int \sigma(v) v f_M(v,T) \mathrm{d}v = 2\sqrt{\frac{2}{\pi m}} (k_B T)^{-3/2} \int_{\Delta E}^{\infty} \sigma(E) E \exp\left(-\frac{E}{k_B T}\right) \mathrm{d}E. \quad (20)$$

$E \in [\Delta E, \infty)$, where ΔE is the threshold energy for the process. For excitation and ionization, it is equal to the energy difference between the states ($\Delta E = E_{pq}$), while $\Delta E = 0$ for de-excitation and recombination.

3.1.3 Detailed balance

For some processes, the cross sections may be more complicated to obtain: for instance, the three-body recombination, since it involves three reaction partners. The principle of detailed balance can be used to simplify the derivation and reduce the size of the database in half. In thermodynamic equilibrium, forward and backward reactions are related via

$$\langle \sigma_{pq} v \rangle n_q n_e^a = \langle \sigma_{qp} v \rangle n_p n_e^b. \quad (21)$$

Let us assume w.l.o.g. $q < p$. $\langle \sigma_{pq} v \rangle$ is the rate coefficient for the reaction $q \nearrow p$ and $\langle \sigma_{qp} v \rangle$ for the inverse process $p \searrow q$. Actually, for the three-body recombination $\alpha(q) = \langle \sigma_{qp} v \rangle = \langle \langle \sigma_{qp}^{3b} v \rangle v \rangle$, where σ_{qp}^{3b} is averaged over the Maxwellian distributions of both electrons. q is an atomic state and p an ion state. The rate coefficient α can be obtained from the electron impact ionization rate coefficient $S(q) = \langle \sigma_{pq} v \rangle$ with $a = 1$ and $b = 2$. Using (2), this results in $\alpha(q) = S(q) \cdot Z(q)$.

For all other electron collision processes, $a = b = 1$. n_q and n_p are given by (2), hence

$$\langle \sigma_{pq} v \rangle g(q) = \langle \sigma_{qp} v \rangle g(p) \exp(-\Delta E_{qp}/T). \quad (22)$$

The detailed balance principle can be also derived for cross sections. While more cumbersome for three-body-interactions like ionization and recombination, it is straight forward for two-body-interactions like excitation and de-excitation: first, we apply (20) to (22). Notice that the integrals are identical up to the lower integration limit: $\Delta E = 0$ for $p \searrow q$ and $\Delta E = E_{pq}$ for $q \nearrow p$. By substituting $E' = E - \Delta E$, we derive for the expression under the integral

$$\sigma_{pq}(E + \Delta E_{pq}) g(q) (E + \Delta E_{pq}) = \sigma_{qp}(E) g(p) E, \ \forall E > 0. \quad (23)$$

3.1.4 Collision strength

The excitation cross section is often represented via the collision strength $\Omega(x) = \Omega(E/\Delta E_{pq})$, [4],

$$\sigma_{pq}(E, \Delta E_{pq}) = \begin{cases} \pi a_0^2 \frac{Ry}{g(q)E} \Omega_{pq}\left(\frac{E}{\Delta E_{pq}}\right) & \text{for } E \geq \Delta E_{pq} \\ 0 & \text{for } E < \Delta E_{pq} \end{cases} \quad (24)$$

with collision energy E, energy difference ΔE_{pq}, Rydberg energy $Ry = 13.6057$ eV and Bohr radius a_0. Inserting (24) into (23) and substituting $x = E/\Delta E_{pq}$ results in the detailed balance for collision strengths

$$\Omega_{p \nwarrow q}(x+1) = \Omega_{q \swarrow p}(x) \ \forall x \in [0, \infty). \quad (25)$$

Inserting (24) into (20) gives

$$\langle \sigma v \rangle_{p \nwarrow q} = C_1 \cdot C_2(T,q) \int_1^{\infty} \Omega_{p \nwarrow q}(x) \exp\left(-x \frac{\Delta E_{pq}}{T}\right) \mathrm{d}x, \quad (26)$$

with $C_1 \equiv \pi a_0^2 Ry \cdot 2\sqrt{\frac{2}{m\pi}}$ and $C_2(T,q) = \Delta E_{pq} / \left[g(q) \, (k_B T)^{3/2} \right]$.

Note that e^{-x} decreases monotonically with x, so that near threshold values $\Omega(x \approx 1)$ can give a very important contribution to the integral (depending on Ω). With increasing electron temperature T, $e^{-x/T}$ falls less quick, so that the contribution of $\Omega(x)$ at larger x becomes more important at higher temperatures.

For the inverse process, using (25) and $x' = x + 1$, we obtain

$$\langle \sigma v \rangle_{q \swarrow p} = C_1 \cdot C_2(T,p) \int_0^\infty \Omega_{q \swarrow p}(x) \exp\left(-x \frac{\Delta E_{pq}}{T} \right) \mathrm{d}x \tag{27}$$

$$= C_1 \cdot C_2(T,p) \int_0^\infty \Omega_{p \nwarrow q}(x+1) \exp\left(-x \frac{\Delta E_{pq}}{T} \right) \mathrm{d}x \tag{28}$$

$$= C_1 \cdot C_2(T,p) \int_1^\infty \Omega_{p \nwarrow q}(x') \exp\left(-(x'-1) \frac{\Delta E_{pq}}{T} \right) \mathrm{d}x' \tag{29}$$

$$= \exp\left(\frac{\Delta E_{pq}}{T} \right) \frac{g(q)}{g(p)} \langle \sigma v \rangle_{p \nwarrow q} \tag{30}$$

$$= \frac{Z(q)}{Z(p)} \langle \sigma v \rangle_{p \nwarrow q} \tag{31}$$

with the Saha-Boltzmann equilibrium values $Z(p)$ given by equation (2). In the CR code [1] expression (29) is evaluated for de-excitation $\langle \sigma v \rangle_{q \swarrow p}$ by numerical integration, and the corresponding excitation rate coefficient $\langle \sigma v \rangle_{p \nwarrow q}$ is then found from relation (31).

3.2 Database G2012 [1]

In section 3.1 we have discussed how reaction rates in equation (1) relate to elementary processes, radiative and collisional, which must be described according to the laws of quantum mechanics. The quantitative theoretical calculation or experimental measurement of these processes is not subject of the present work. Instead, we rely on the work of other authors who have compiled atomic databases (of oscillator strengths, cross sections etc.) for public usage. The CR model G2012 by Goto [1] contains a complete collection of atomic data from a number of databases. Due to its size (of 65 energy eigenstates) it is quite heterogeneous. In the following, we will briefly discuss the collection and point out its pros and cons.

One outstanding advantage of the data set is its comprehensiveness: due to the large number of energy eigenstates, with principal quantum number up to $n = 26$, inclusion of recombination processes and a broad range of validity, it has a wide scope of application. This is important for a multi-purpose code such as EIRENE. Nevertheless, limitations will be pointed out.

The atomic data set is based upon the predecessor CR model F1979 [2]. In fact, both the model structure as well as a part of the database remain the same. Among these data are the hydrogenic approximation for $n > 10$, radiative and dielectronic recombination rates. For the recombination rates, issues are discussed in chapter 6. Most other processes were reassessed. Data are still insufficient for higher excited states ($n \gtrsim 5$). The importance of high $n-$states is shown in chapter 7.2. Fortunately, scaling relations can be used for some of them.

The spontaneous transition probabilities, incorporated from [13], are stored in form of oscillator strengths f_{pq}.

Note that both radiative and electron collision processes are affected by the singlet-triplet mixing (see chap. 2.4 and 4), newly incorporated in the present model [1], as compared to [2].

Two different basic atomic data sets are available for electron impact transitions: one contains fits of collision strengths from the report by Ralchenko et al. [4], which is based on CCC-89[†] [17] calculations, benchmarked and internationally evaluated. We will refer to this data set as R2008. The other set contains tabulated collision strength and cross sections, which have been provided privately by [18]. We will refer to it as V2005. Unfortunately, no reference nor a public exposition of this data set existed until now. We made the set accessible at the HYDKIN web page [8].

3.2.1 Ionization cross sections

At the time of Fujimoto's original work [2], experimental cross sections were only available for the 1^1S and 2^3S levels, while for others the hydrogenic approximation was adopted. It is therefore not surprising that newer data are quite different: Figure 2 depicts the difference between both models [1] and [2] for $n \leq 7$.

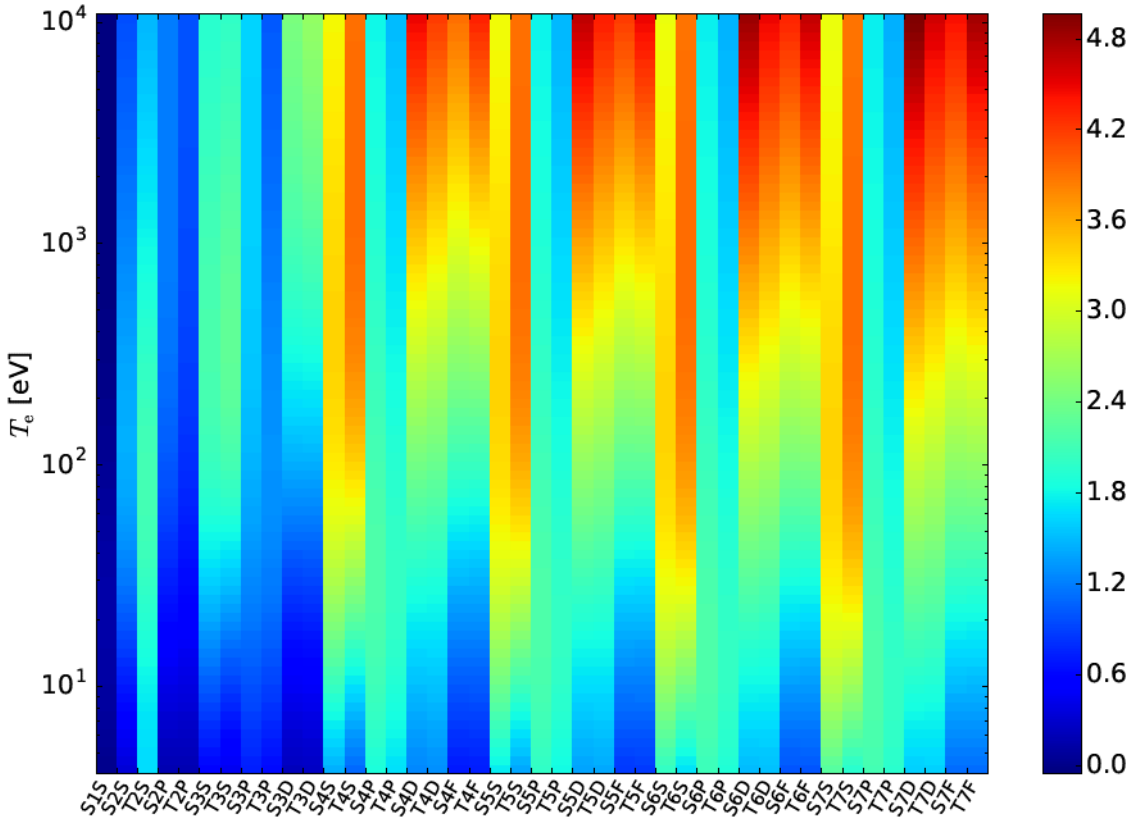

Figure 2: Relative difference in ionization rates between [1] and [2], $\Delta S/S = S_{\mathrm{F1979}}/S_{\mathrm{G2012}} - 1$. Horizontal axis corresponds to different initial states $p = \tilde{S}nL$, with $\tilde{S}$ =S for singlet and $\tilde{S}$ =T for triplet.

In our current model G2012, the internationally evaluated and recommended cross sections by Ralchenko et al. [4] (R2008) are adopted for $n \leq 4$ via analytic fits of the form

$$\sigma_p(E) = \frac{10^{-13}}{\chi(p)E}\left[A_1(p)\ln\frac{E}{\chi(p)} + \sum_{i=2}^{6} A_i(p)\left(1-\frac{\chi(p)}{E}\right)^{i-1}\right] \quad (\mathrm{cm}^2). \tag{32}$$

[†]convergent close coupling (CCC) method implementing 89 coupled states (CCC-89)

Here, E [eV] is the kinetic energy of the colliding electron, χ [eV] the ionization potential for state p, and A_i are fitting coefficients, stored in an ASCII file. For $5 \leq n \leq 7$, the classical scaling law

$$\sigma_{n^{1,3}L}(E) = \left(\frac{\chi_{4^{1,3}L}}{\chi_{n^{1,3}L}}\right)^2 \sigma_{4^{1,3}L}\left(\frac{\chi_{4^{1,3}L}}{\chi_{n^{1,3}L}}E\right) \tag{33}$$

is applied. This explains the (approximate) periodicity in fig. 2. The hydrogenic approximation is kept for $n \geq 8$.

The ground state ionization cross section agrees well with theory and experimental data, and so the rates are quite equal in G2012 and F1979 codes. But there was a long lasting debate about the 2^3S ionization cross section: while different theoretical calculations agreed well among themselves, "there has been only one experiment spanning a significant energy range, performed more than 40 years ago [19, number different in original] and whose results are in sharp disagreement with the most accurate calculations performed over the past 20 years" [20]. According to Génévriez et al. [20], this was due to the difficulty of the experimental setup. They recently repeated the measurement of that cross section, and these new experimental results now agree and fully confirm the theoretical CCC-89 calculations. Although not very explicit from the text, the data set R2008 [4] was fortunately already based on the theoretical CCC-89 calculations, including ionization from 2^3S. This explains the huge difference in the resulting reaction rates $S(2^3S)$ between [1] and [2] (seen in fig. 2), since the latter used the old experimental data from [19].

3.2.2 Electron impact transition data set V2005 [18]

The user of the CR code G2012 [1] may switch between the data sets, but the default model activated (since March 29, 2012) was V2005 [18]. It was therefore retained for most calculations in the current work.

One large benefit of the data set V2005 is its comprehensiveness: it contains excitation collision strength / cross sections for initial $n_i \leq 5$ and final $n_f \leq 6$, which are in total 567 transitions (disregarding inverse processes, obtained through detailed balance).

Additionally, an extrapolation to $n_f = 7$ with $C(n_i, n_f = 7) = C(n_i, n_f = 6) \cdot \left(\frac{6}{7}\right)^3$ is applied. For other transitions, the old F1979 model [2] is retained.

The data are stored on an energy grid between $E_{\min} \approx \Delta E = \Delta E_{pq}$ and $E_{\max} \approx 500$ eV. On average, 25 grid points are used, although up to 73 for some ground state transitions. Excitation rate coefficients are calculated according to (26): integration starts at $E_{\min}$, $\Omega(x)$ is interpolated linearly between grid points, and for $E_{\max} < E < \infty$ an extrapolation is employed. De-excitation rate coefficients are calculated by the detailed balance (22).

The first grid point $E_{\min}$ at which Ω is stored is not ΔE, hence $x_{\min} \neq 1$. Since integration starts at $x_{\min}$, it can be regarded as effective threshold $E_{\min} = \Delta E_{\text{eff}}$. The values of the effective threshold energies for all transitions in V2005 are listed in table 1. Numerical uncertainty is a possible reason for the deviation, since larger $x_{\min}$ are usually encountered for small ΔE, but a systematic deviation is also possible.

The exact effect on the reaction rates due to $x_{\min} \neq 1$ is difficult to estimate universally. The threshold region is important, since the exponential factor in the integral (26) is maximal there.

Table 1: Normalized effective threshold energies $x_{\min} = \Delta E_{\text{eff}}/\Delta E$ in the V2005 [18] data set.

$x_{\min}$ range	number of transitions
0.96 - 1	138
1 - 1.1	271
1.1 - 1.5	122
1.5 - 2	11
2 - 3	10
3 - 10	2
10 - 100	10
≈ 177	1
≈ 6770	2

However, the energy interval, where the discrepancy occurs, is rather small. Therefore, we expect no large impact, as long as $\Omega(x)$ stays "reasonable" in that interval. "Reasonable" means, the integral over that interval must be sufficiently small compared to the whole integral.

The largest drawback of the data set is the lack of a reliable reference, meaning there is no estimate for its validity. To enable falsifiability of the current work, the data (cross sections) were made publicly accessible at the HYDKIN web page [8].

3.2.3 Electron impact transition data set R2008 [4]

Due to the lack of a clear reference for the default model V2005 [18], we decided to switch back to electron impact transition cross sections from R2008 [4][†]. This seemed easy on first sight, since the option was already pre-programmed in the CR code (routine 'ralchenko.c'). But it turned out, there had been good reasons why this option had been de-activated. The issues were found and cured, now allowing the utilization of the full data set. The issues are discussed in this chapter. Additionally, the original cross sections from [4] were made accessible at the HYDKIN web page [8].

The data are based on the CCC-89 method [17], which yields cross sections for discrete energies. For a compact representation over the whole energy range, including proper high energy asymptotics, analytic fit functions are adapted in R2008 [4] for the three excitation groups:

(i) Dipole-allowed ($\Delta S = 0$, $\Delta L = \pm 1$)

$$\Omega(x) = \left(A_1 \ln(x) + A_2 + \frac{A_3}{x} + \frac{A_4}{x^2} + \frac{A_5}{x^3}\right)\left(\frac{x+1}{x+A_6}\right), \tag{34}$$

(ii) Dipole-forbidden ($\Delta S = 0$, $\Delta L \neq \pm 1$)

$$\Omega(x) = \left(A_1 + \frac{A_2}{x} + \frac{A_3}{x^2} + \frac{A_4}{x^3}\right)\left(\frac{x^2}{x^2+A_5}\right), \tag{35}$$

(iii) Spin-forbidden ($\Delta S \neq 0$)

$$\Omega(x) = \left(A_1 + \frac{A_2}{x} + \frac{A_3}{x^2} + \frac{A_4}{x^3}\right)\left(\frac{1}{x^2+A_5}\right). \tag{36}$$

[†]In the code, originally, the data set 'R2000' [21] was implemented, later exchanged by V2005.

These fit expressions were supposed to be convenient to integrate to rate coefficients. Note, however, that in the routine 'ralchenko.c' of the CR code de-excitation rate coefficients are calculated first according to eq. (29). Excitation rate coefficients are then calculated from the detailed balance for rates (22).

The data set R2008 covers all transitions with n_i, $n_f \leq 4$, which are 171 in total (disregarding, again, inverse processes). Hence, it is less comprehensive than V2005 but fully reproducible. For $n_i \leq 3$ and $5 \leq n_f \leq 7$, the scaling law

$$\Omega_{pq}\left(\frac{E}{\Delta E_{pq}}\right) = \left(\frac{4}{n_f}\right)^3 \frac{\Delta E_{pq}}{\Delta E_{4q}} \Omega_{4q}\left(\frac{E}{\Delta E_{pq}}\right) \tag{37}$$

is applied. It means (by abuse of language), that instead of the unknown collision strength for the transition $q \to p$, $p = n_f^{2S+1}L$, the collision strength for $p' = 4^{2S+1}L$ is evaluated, but with the correct threshold energy. It is then scaled by the threshold energy and the principle quantum number ratio cubed. For other transitions, again the F1979 [2] model is retained.

Unfortunately, it turned out that the data utilized by the routine (fit coefficients $A_1 - A_6$) have not all been exactly those from the Ralchenko et al. [4] paper either. Their sources in the original code are depicted in Figure 3.

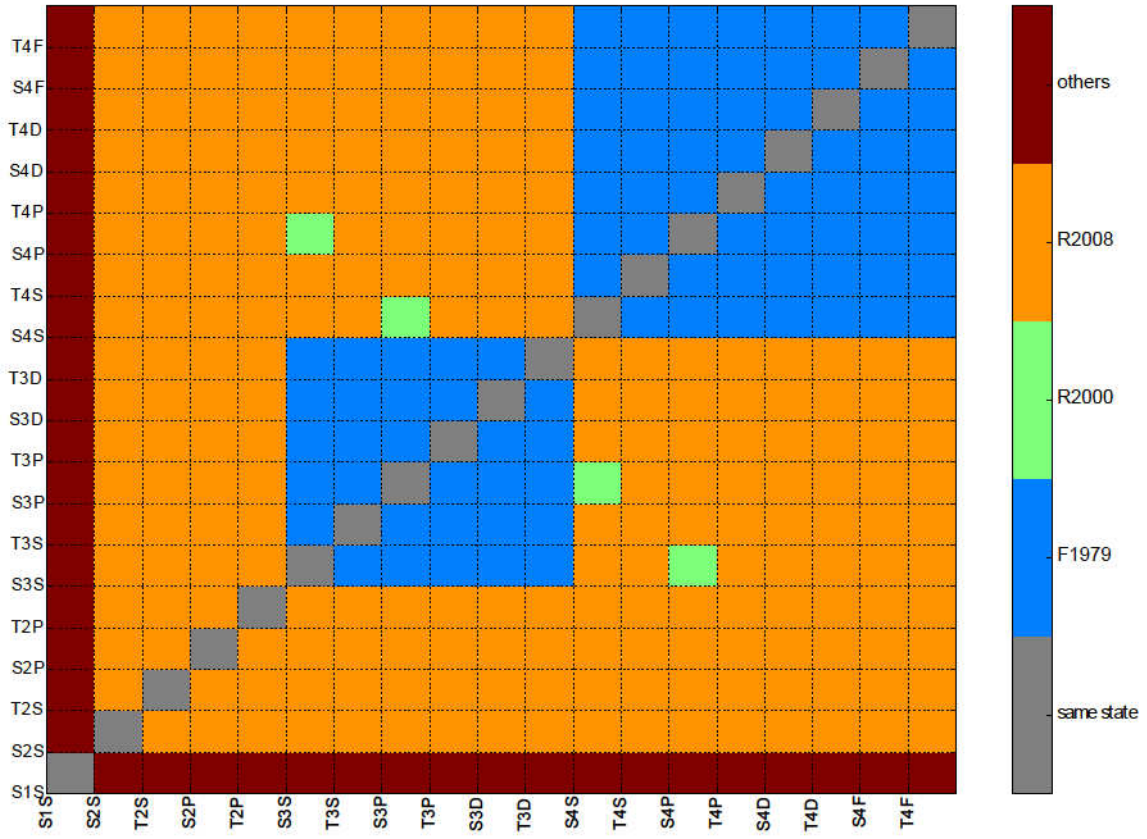

Figure 3: Cross section data originally utilized by the CR model G2012 [1] in the 'ralchenko.c' routine. Axes labels correspond to states $p = \tilde{S}nL$, with $\tilde{S}$ =S for singlet and $\tilde{S}$ =T for triplet. Each square is a transition between the state on the vertical axis and the state on the horizontal axis. The symmetry is due to detailed balance (22). The references are: F1979 [2], R2000 [21], R2008 [4], others - no known reference.

We could not fully identify why different expressions were used for ground state excitation. However, the fits were very close to the ones in [4], so that we now simply replaced them by

the presumably improved ones from R2008, see Figure 4 for an example. For two transitions,

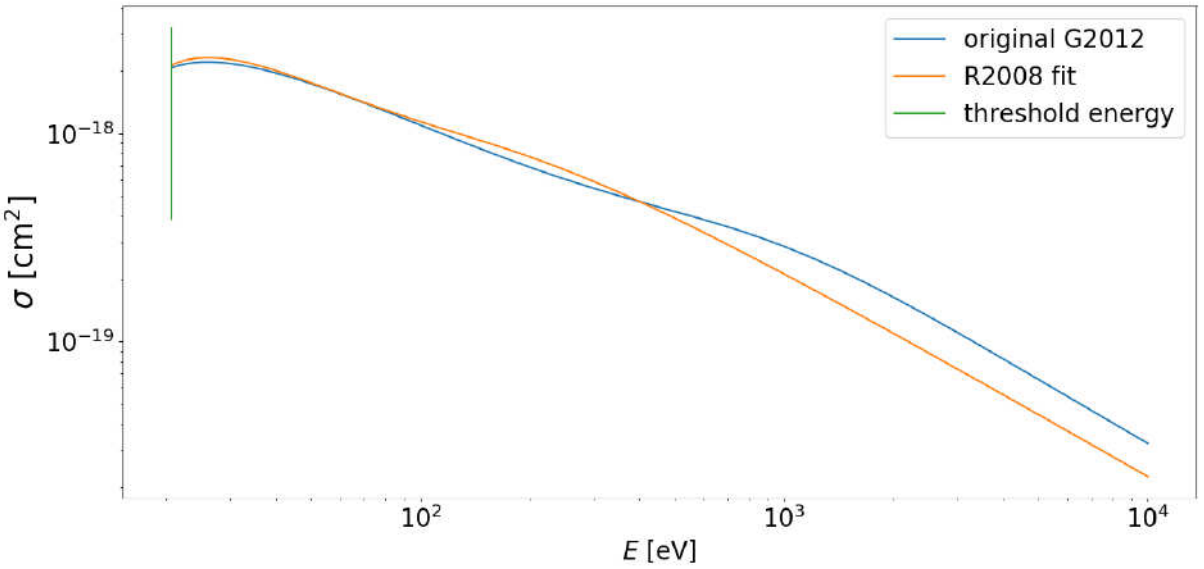

Figure 4: Cross section data originally utilized by the CR model G2012 [1] in the 'ralchenko.c' routine for the ground state excitation to $p = 2^1S$, blue curve, and (improved) fit from R2008 [4] (red curve) for the same transition.

marked in light green in Figure 3 the data base update from R2000 [21] to R2008 [4] was simply missed out, and so we now updated these data. These changes did not have any significant impact on line intensity ratios (in chapter 7.3). Hence, only one class of differences between the reference [4] and the actual CR model remained: the $n_i = n_f = 3$ and $n_i = n_f = 4$ transition collision strengths were not used at all in the CR model, the old data from F1979 [2] were kept instead. Also this issue is now resolved, as we will discuss next, so that now the full R2008 dataset, for all transitions, is made available in the CR code.

It turns out (see chap. 7.3) that this difference in the l-mixing collisions within n=3 and n=4 states, in fact, is quite significant. Therefore, we started analyzing individual collision strength fits, as well as their numerical integration. The conclusion: some fits show an unphysical increase with $1 \leftarrow x$, close to the threshold. Moreover, the applied integration routine seems to be not optimal for the problem. The combination of both issues made their identification difficult[†].

We contacted the first author of [4] (Y. Ralchenko, NIST), who confirmed that the fits for transitions with the smallest thresholds have a poor near-threshold behavior. In fact, for the transition $3^3D \rightarrow 3^1D$ (with $\Delta E \approx 0.4$ meV) recently the collision strength up to the threshold was recalculated, and a new fit, based on that data, behaves very differently (see fig. 5) [22].

In [4] it was actually already recommended to use the original (discrete) data for the lowest energies, at least for these very low threshold processes $\Delta E \ll 1$ eV, rather than the fits. Unfortunately, the original data seem to be not available any more.

Another possible solution (proposed by Ralchenko [22]) would be to simply apply a linear extrapolation from the last valid point at 0.1 eV down to ΔE (i.e. to $x = 1$) whenever the threshold energy is smaller than 0.1 eV

$$\Omega(x) = ax + b, \forall x \in [1, x_0), x_0 = 0.1/\Delta E$$

[†]Maybe this is the reason for the change from R2000 [21] to the V2005 [18] data set in the G2012 CR code?

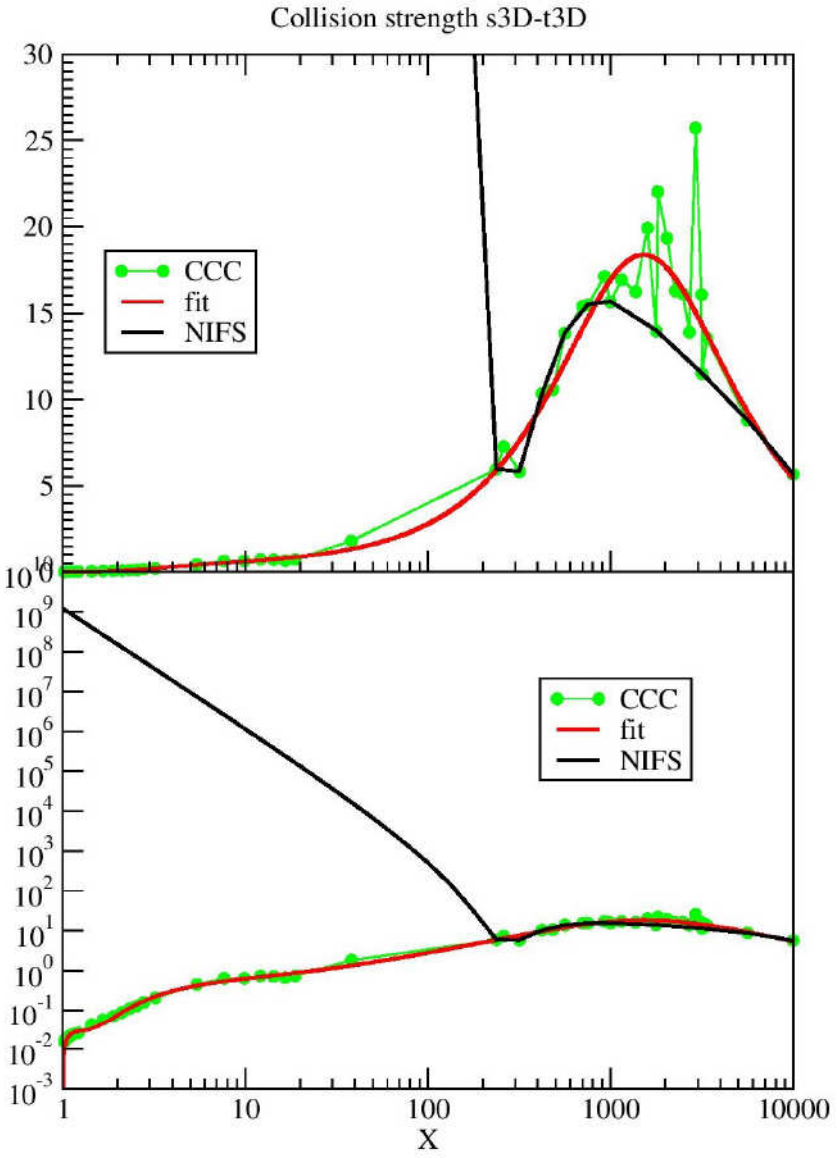

Figure 5: Collision strength for the electron impact transition $3^3D \rightarrow 3^1D$, with linear y-scale on top and logarithmic y-scale at the bottom. R2008 fit [4] (NIFS, black) is compared with newer data (CCC, green) and a newer fit (red) [22]. When producing the R2008 fit (NIFS), data had been only available down to 0.1 eV (i.e. starting at reduced energy $x \sim 250$ for this particular process) [22].

with a and b fixed by $\Omega(1) = 0$ and $\Omega(x_0) = ax_0 + b$ (continuity). This seems reasonable, because we would not expect a significant contribution to the integral from this small energy interval anyway – except if the collision strength is orders of magnitude too large.

Besides unphysical near-threshold behaviour of the fits, there were convergence issues in the numerical integration, even for transitions with seemingly correct fits (compared e.g. to V2005 data tables [18]). In the 'ralchenko.c' routine [1], the integration algorithm for equation (29) is 'gsl_integration_qagiu' from the GNU Scientific Library [23]. It is a powerful generic tool for adaptive integration on infinite intervals: first, the interval in mapped from $x' \in [1,\infty)$ onto $t \in [1,0)$ via $x' = 1 + (1-t)/t$. Then, the integral is computed via adaptive bisection (Gauss-Kronrod 21-point integration rule) supplemented by the Wynn epsilon-algorithm.

The convergence issues could be bypassed for $T_e < 200$ eV by adjusting the linear extrapolation beyond the physically justified limit. For the transition $4^1D \rightarrow 4^1F$, $x_0 = 0.6$ eV / ΔE was nec-

essary, and for the $4^3D \rightarrow 4^3F$ transition $x_0 = 0.192$ eV / ΔE. This, without any extrapolation for other transitions, led to Figure 17. Additionally, we could apply the extrapolation for all other transitions for which $x_0 = 0.1$ eV / ΔE exceeds the value one, except for $4^3F \rightarrow 4^1F$. For the latter, $\Delta E \approx 2$ μeV and the fit looks fine starting already from 1 meV, so that we set $x_0 = 1$ meV / ΔE. This led to Figure 18.

However, the above corrective procedure still did not work universally (i.e. for all transitions) for $T_e > 200$ eV. This suggests that the gsl integration routine is inappropriate for the task, as long as it is applied, without modification, for all three types of processes (dipole-allowed, dipole-forbidden, spin-forbidden) mentioned earlier. Due to their fundamentally different high energy asymptotic behaviours this is also to be expected. Asymptotically correct analytical expressions, one for each of these three types of processes, are already implemented in case of the (tabulated) V2005 data tables, for the high energy range contributions beyond the last data point. But these are not jet available in the code when the R2008 data fits are used.

On the other hand, for a multi-purpose code like EIRENE, coverage of a wide parameter range with one single data format is highly preferable to avoid a large number of special case data sets, which would make the database less transparent. Therefore, we replaced the integration routine for the R2008 data base.

We note that it is possible to fully exploit the presence of the Boltzmann factor in the integral by utilization of the Gauss–Laguerre quadrature [24]. First, we rewrite equation (29) as

$$\begin{aligned}\langle\sigma v\rangle_{q\swarrow p} &= C_1 \cdot C_2(T,p) \int_1^\infty \Omega_{p\nwarrow q}(x') \exp\left(-(x'-1)\frac{\Delta E_{pq}}{T}\right) \mathrm{d}x' \\ &= C_1 \cdot C_2(T,p) \int_0^\infty \Omega_{p\nwarrow q}(x+1) \exp\left(-x\frac{\Delta E_{pq}}{T}\right) \mathrm{d}x \\ &= C_1 \cdot C_2(T,p) \frac{T}{\Delta E_{pq}} \int_0^\infty \Omega_{p\nwarrow q}\left(\tilde{x}\frac{T}{\Delta E_{pq}} + 1\right) \mathrm{e}^{-\tilde{x}} \mathrm{d}\tilde{x}. \end{aligned} \tag{38}$$

The solution for the integral in (38) can be approximated via

$$\langle\sigma v\rangle_{q\swarrow p} \approx C_1 \cdot C_2(T,p) \frac{T}{\Delta E_{pq}} \left[\sum_{i=1}^{n} \Omega_{p\nwarrow q}\left(x_i \frac{T}{\Delta E_{pq}} + 1\right) \cdot \alpha_i\right], \tag{39}$$

with Gauss-Laguerre nodes x_i (i-th root of Laguerre polynomial $L_n(x)$) and weights α_i. As in the HYDKIN online tool we use $n = 64$. Gauss-Laguerre nodes and weights are also given, for example, in [25]. The resulting integration procedure turned out to be far more robust and gives very reasonable results, although we have not carried out an integration error estimate, e.g. by varying the number of Gauss-Laguerre nodes to 16 and 32 spot checks for accuracy and Richardson extrapolation.

Near threshold linear extrapolation is also applied for the above Gauss-Laguerre integration procedure, for the nodes $x_i \frac{T_e}{\Delta E} + 1 < \frac{0.1\ \mathrm{eV}}{\Delta E}$. Since x_1 is fixed for a given number n of Gauss-Laguerre nodes (e.g., to $x_1 = 2.24 \times 10^{-2}$ for $n = 64$), the condition is equivalent to $\Delta E < 0.1$ eV$-x_1 \cdot min\{T_e\}$. The resulting line intensity ratios are in excellent agreement with those of Figure 18. The rate coefficients C as well as collisional-radiative rate coefficients k, S_{CR} and α_{CR} could be obtained for $T_e \in [0.3, 10^4]$ eV and were made accessible at the HYDKIN web page [8].

Interestingly, the above Gauss-Laguerre integration also works without correction of the fits below 0.1 eV. The resulting line intensity ratios are even quite close to those of Figure 18. This

might be due to the fact that $\Omega(x_i)$ is now only evaluated at discrete points x_i, mostly avoiding the spurious near threshold divergence of the fits. Nevertheless, at very small T_e the effect from spurious fits can be seen in some individual reaction rates C with small ΔE (at HYDKIN): while the integrated reaction rates contain the linear near threshold corrective extrapolation in collision strengths, we have also stored the original cross sections from fits in R2008 [4], without the asymptotic near threshold correction. Therefor Maxwellian average integrals from the real time (online) evaluation can thus be slightly different at very small temperatures and thresholds.

3.2.4 Conclusion on atomic data

The helium CR model G2012 appears to be well suited for the application in the experiment, or in its simulation. Its large advantage is that (a large part of) its underlying atomic cross section data base was internationally evaluated and today provides a "golden standard". We have reviewed the remaining issues, and were able to fix the most important ones. The remaining open points are well known and could (and should) be reexamined by the atomic physics community in future.

Issues with the radiative and dielectronic recombination rates are discussed in chapter 6. Fortunately, they do not concern the helium beam diagnostic, since recombination can be assumed to be negligible within the Helium beam there.

Owing to the recent work [20], remaining discrepancies between theory and experiment concerning ionization cross sections could be resolved - confirming the theoretical CCC data. Therefore, the data from [4] appear to be trustworthy. Similar data for higher principle quantum number states are desirable, their importance will be demonstrated in chapter 7.2.

For the electron impact transition cross sections, we have implemented a robust integration routine for the reaction rate coefficients, allowing full utilization of the R2008 data set [4] in a broad parameter range. Flaws of the fit expressions for collision strengths at energies $\lesssim 0.1$ eV were identified, so that we currently cannot recommend utilization of the data set below 2-5 eV temperature, until the very low threshold processes have been corrected. In fact, in [4] it is recommended to use the original (discrete) CCC-89 data in the critical energy range - but these data appear to be, unfortunately, lost.

Alternatively, the V2005 [18] (tabulated) database is available in the code. In fact, it was probably used for most parts in the past and also in the present work, mainly because a reliable integration of R2008 data was added only now. It was also significantly more comprehensive. Certainly, due to the lack of any reliable reference regarding the origin of the data, now usage of the full R2008 data is recommended.

Since correct atomic data are essential for the application in the experiment, we compare resulting line intensity ratios from R2008 transition data [4] to the previously activated model V2005 in chapter 7.3. However, results from chapter 9 should not depend on the underlying data set, as long as the transport calculations and synthetic diagnostic are self consistent with repect to the data used. This is the case, if the same data are used both in the backward calculation (plasma parameter reconstruction) and in the forward calculation (synthetic spectra generation).

To ensure "falsifiability" of the current work, all unprocessed (cross section) data were made publicly accessible at the HYDKIN web page [8].

4 Effect of the magnetic field

In Goto's CR model, transition rate coefficients vary with the magnetic field due to the singlet-triplet wavefunction mixing introduced in chapter 2.4. This dependence propagates to the CR coefficients and population coefficients. CR rate and coupling coefficients are plotted, for relevant plasma parameters, in Figure 6, normalized to their value at 0 tesla. Note: in this chapter, V2005 electron impact transition rates from [18] were used. R2008 [4] data may change the numbers a little, but since the mixing itself does not depend on the data, the overall behavior should be the same.

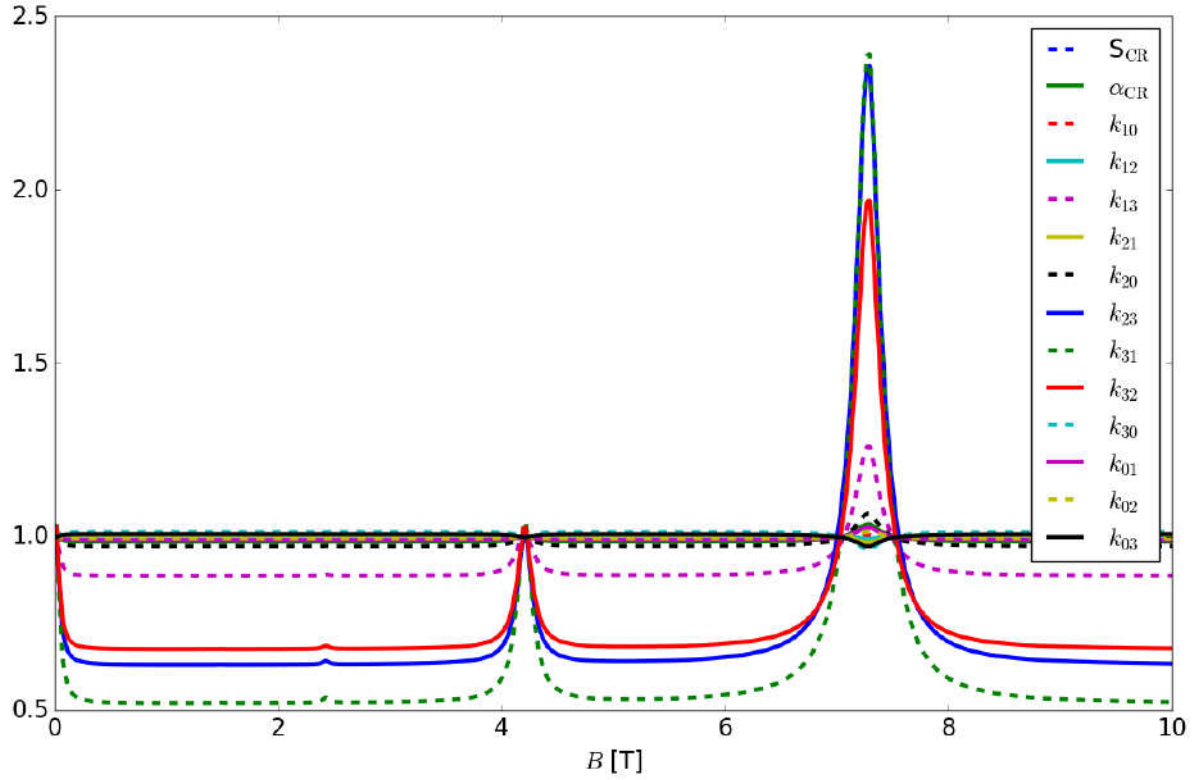

Figure 6: Dependence of the CR rate and coupling coefficients on the magnetic field, normalized to their value at 0 tesla. Plasma parameters are $T_e = 200$ eV and $n_e = 10^{20}$ m^{-3}.

A resonance-like behavior is observed, with peaks at 0 T, 2.4 T, 4.2 T and 7.3 T. The peak positions are independent of plasma temperature and density, but their magnitudes do vary with both.

For the CR rate coefficients S_{CR} and α_{CR} (formulation II), no significant change can be observed: S_{CR} varies for less than 1%, α_{CR} has a 1% peak at 0 tesla and a 4% peak at 7.3 tesla.

CR coupling coefficients (k's from formulation I) are much stronger influenced: the coupling of the triplet meta-stable state 2^3S to the singlet meta-stable 2^1S and ground state 1^1S is significantly reduced by the magnetic field between the resonances and enhanced at 7.3 T.

The temperature dependence of the offset between B = 0 T and B = 1 T is displayed in Figure 7 for a few CR coupling and population coefficients. At $T_e > 200$ eV, the resonances saturate. The reduction of the k_{31} coefficient is relevant already at a few eV. The magnetic field effect on the population coefficients $R_1(3^1S)$, $R_1(3^3S)$ and $R_1(3^1D)$ is comparatively small, espe-

cially at $T_e < 50$ eV. These are relevant for the established helium beam diagnostic (see chapter 7). States with higher orbital quantum number L are more affected by the singlet-triplet state mixing, hence, population coefficients of such states ($R_1(4^1F)$) vary much stronger with the magnetic field.

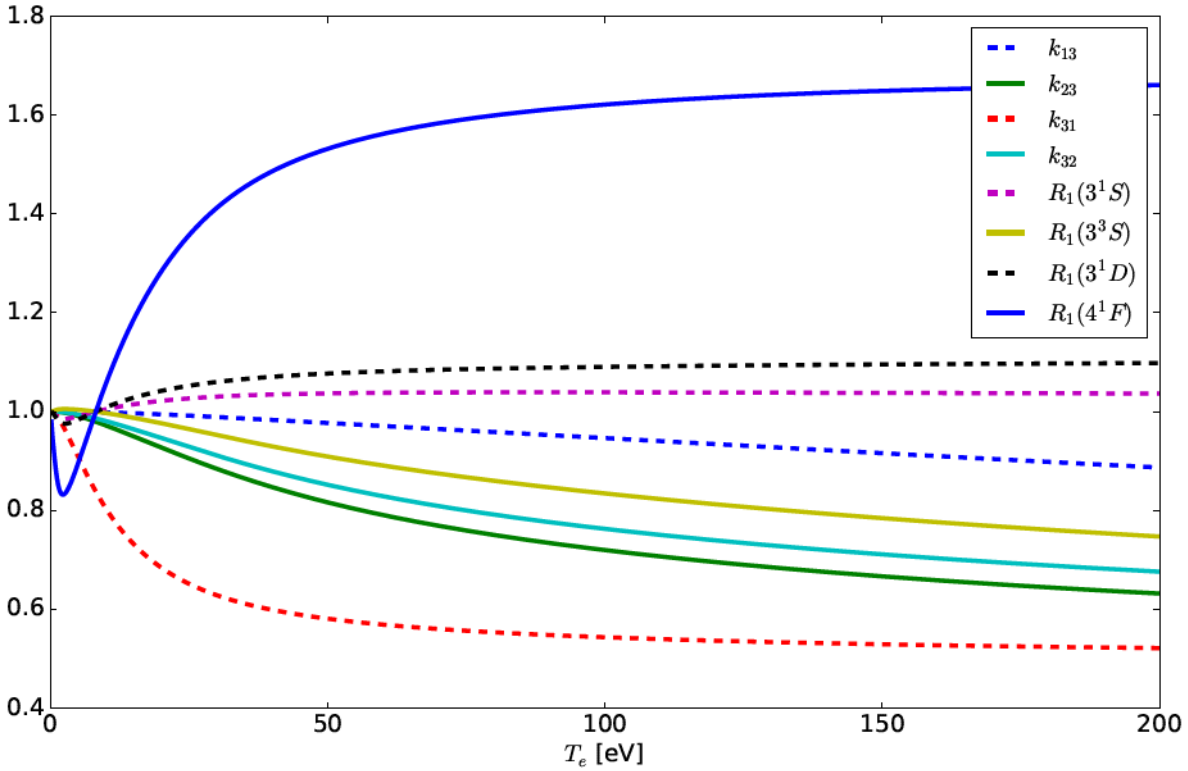

Figure 7: Temperature dependence of the offset between $B = 0$ T and $B = 1$ T for CR coupling and (form. II) population coefficients at $n_e = 10^{20}$ m^{-3}.

In Figure 8, dependence of the (form. II) population coefficients and their ratios on the magnetic field is displayed, normalized to their value at 0 T. At $B < 4$ T, the density sensitive ratio $R_1(3^1D)/R_1(3^1S)$ changes for less than 10% even at $T_e = 200$ eV because both coefficients become larger. The temperature sensitive ratio $R_1(3^1S)/R_1(3^3S)$ changes for up to 40% at high T_e because of the opposite sign of the triplet population coefficient offset. A large resonance is observed at 7.3 T. In contrast to Figure 7, here the singlet population coefficients also change at $T_e < 5$ eV, leading to a density ratio change of 15% and temperature ratio change of 30% at 4 eV. At lower densities, the magnetic field effect is smaller.

In conclusion, different aspects of the CR model require the consideration of the singlet-triplet state mixing: it is negligible for the CR rate coefficients in formulation II, but not for the population of higher states in this formulation and generally not for formulation I. S_{CR} and α_{CR} are probably unaffected because they combine the singlet and triplet state dynamic, while the mixing only leads to linear combination of initial singlet and triplet rates.

Luckily, there is nearly no variation with the magnetic field in between the resonance peaks. This can be used to omit the explicit $B-$dependence. Especially smaller experiments with $0.2 < B < 3.7$ T, including the stellarator W7-X, can simply use atomic data at e.g. $B = 1$ T, since the effect of the resonance at 2.4 T is very small.

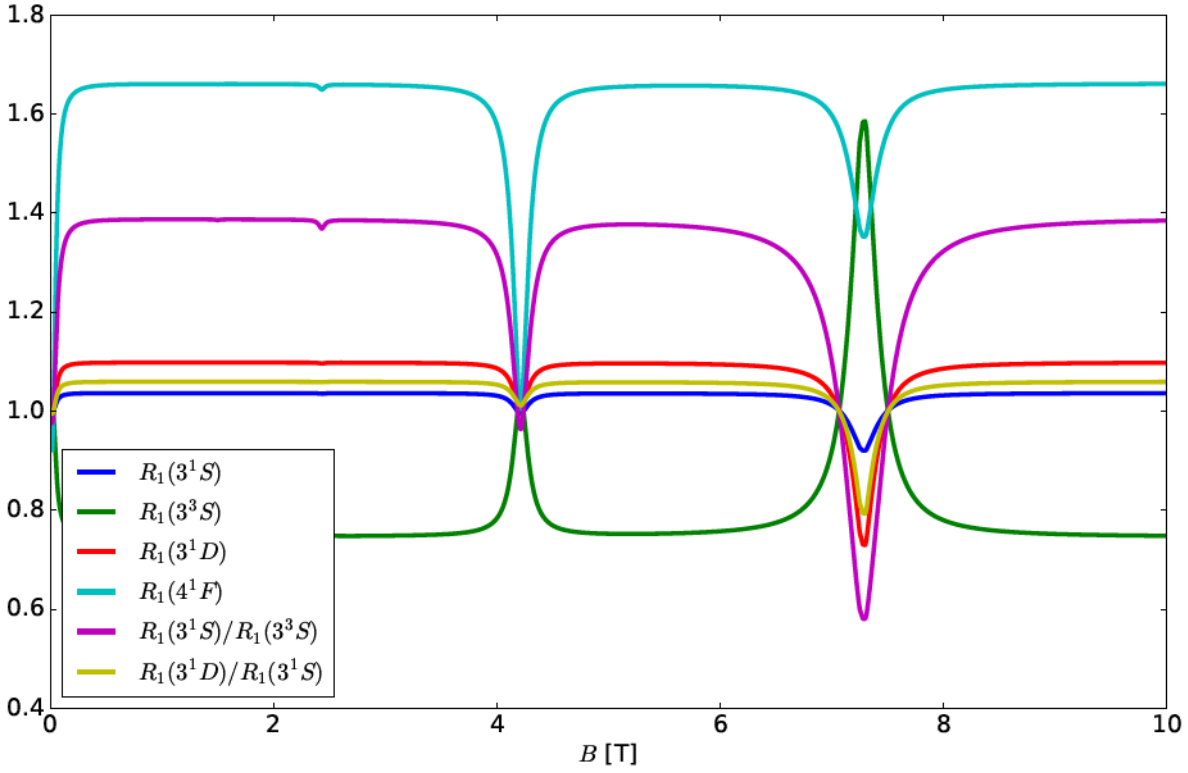

Figure 8: Dependence of the (form. II) population coefficients and their ratios on the magnetic field, normalized to their value at 0 tesla. Plasma parameters are $T_e = 200$ eV and $n_e = 10^{20}$ m^{-3}.

In experiments with $B > 3.7$ T, like ITER, it may be necessary to take the magnetic field dependence into account explicitly.

5 Evaluation of atomic data via HYDKIN

Condensed collisional-radiative coefficients (with both V2005 [18] and R2008 [4] sets of electron impact transition cross sections) were made accessible online at the HYDKIN web page [8]. There, they can be compared to the original F1979 [2] data, ADAS [26], etc. The page also contains a solver for reaction kinetics, with which the data can be directly utilized. E.g., in combination with an additional model for the hydrogenlike helium ions [27], they can be used for 0D estimations of conditions in helium plasmas [28].

Besides that, Weger [29] has implemented a flexible tool at the web page for dimension reduction of master rate equations. It can be used to further simplify the calculations for more complex plasma-chemical processes. The tool grants its users high flexibility by allowing them to decide about the P and Q space dimension during run time. A criterion for the validity of the choice is also given.

The tool is also able to reproduce the CR coefficients from the CR code [1] from initial atomic data used. The fully state resolved data therefor were also made accessible at the web page. Hence, the user can choose to use form. I or II, or define any other P space.

5.1 Test particle coupling coefficients

The Monte-Carlo code EIRENE [7, 9] tracks so called "test particles": they may belong to different species. Thereby, for a physical particle with multiple possible (quantum-mechanical) states, each tracked state would belong to a distinct species. On their trajectories, test particles undergo chemical reactions for which the program requires reaction rates: from the initially tracked state into every possible final state. This means, the particles change their species. Hence, the reaction rates must specify the initial and the final species.

In contrast, the rate equation (8) describes the density change of a state p by certain source terms and a loss term – but the loss term does not specify the final state. However, the losses must balance the sources, hence

$$k_p = \sum_{j \neq p} k_{pj}. \tag{40}$$

The subscripts $j, l \in \{0, 1, 2, 3\}$ stand for the ion, the ground state 1^1S, and the meta-stable 2^1S and 2^3S states, respectively, and $p \in \{1, 2, 3\}$. Hence, the loss term can be equivalently split into three reaction rates. More precisely, we replace the loss rate k_p with the ionization rate k_{p0}, not present in equation (8). Both EIRENE and HYDKIN get as input these reaction rates k_{jl}, which describe the reactions between two species.

5.2 Data format

According to chapter 4, the atomic data for HYDKIN were produced at $B = 2.5$ T. Therefore, they are valid for $B \in [0.2, 3.7]$ T and suited for all medium-sized fusion experiments with $B < 3.7$ T, in particular for W7-X.

5.2.1 Fully state resolved reaction rates (1D)

Although HYDKIN is able to calculate reaction rates from cross sections and the detailed balance principle, the fully state resolved helium model includes thousands of reactions, and a simpler data format was chosen for the temperature dependent reaction rates: they were stored

on a (decadic) logarithmic temperature grid for $T_e \in [0.3, 10^4]$ eV. In between, they are interpolated exponentially (i.e. linear interpolation on a log-log scale). The value for $T_e \in [T_m, T_{m+1}]$ between two grid points m and $m+1$ is given by

$$\langle \sigma v \rangle (T) = \langle \sigma v \rangle_m \left(\frac{\langle \sigma v \rangle_{m+1}}{\langle \sigma v \rangle_m} \right)^{\frac{T - T_m}{T_{m+1} - T_m}}. \tag{41}$$

The error of such a scheme is difficult to estimate for unknown functions. The interpolation is exact for exponential functions. But for $\langle \sigma v \rangle \sim \exp(-\frac{a}{T})$, the error may become large for smaller T_e. The grid should therefore be not too sparse. In our case, 100 points were chosen.

Outside of the storage interval, the last value is kept by HYDKIN. Certainly this must be replaced by a proper physically correct extrapolation scheme, in the future.

5.2.2 CR coefficients (2D)

For form. I and II, the CR coefficients k_{ij}, S_{CR} and α_{CR} depend on both T_e and n_e. They were therefore stored on a 2D grid. To preserve the uniformity of the database, the ADAS ADF11 format was used. It is well documented on the OPEN-ADAS web-page [26]. Between the grid points, data are interpolated according to (41) in both dimensions. Note that in ADF11, for both the grid points and the CR coefficients the decadic logarithm is stored, as opposed to the 1D data format. Outside of the storage interval, an exponential extrapolation scheme is used by HYDKIN for T_e. For n_e, the last value is kept, hence a constant relation is assumed.

5.3 Comparison with original data set F1979 [2]

Naturally, the new CR coefficients from G2012 [1] should be compared to their older versions. For transition cross sections, the V2005 [18] data set was used here. However, the difference between V2005 and R2008 [4] is generally significantly smaller than the differences when compared to F1979.

We observe the largest relative difference for the k_{32} rate: at higher temperatures it changed by more than one order of magnitude. Comparing to other coupling coefficients, we find k_{32} has little influence on the depopulation of 2^3S. But it changes the population of 2^1S: all coefficients for the population of 2^1S can be compared in Figure 9.

Other k_{3x} coefficients changed less, but also noticeably. This influences the population of 2^3S, which is important for spectroscopy.

At smaller densities ($n_e < 10^{20}$ m^{-3}), the change of the recombination coefficients k_{0x} and α_{CR} is remarkable: α_{CR} is plotted in Figure 10 for both models.

We should point out that the coefficients from the CR code F1979 [2] were fitted, for use in EIRENE, by polynomial functions

$$\ln \langle \sigma v \rangle = \sum_{n=0}^{8} \sum_{m=0}^{8} a_{nm} (\ln T_e)^n (\ln n_e)^m, \tag{42}$$

instead of storing them on a grid for interpolation. But the fits for recombination had a poorer quality, with errors up to 22%[†]. This probably enhances the difference seen in Figure 10: the fit function flattens the extrema and slightly oscillates around the actual path.

[†]This is because of the pronounced extrema at lower densities. The extrema occur due to the combination of

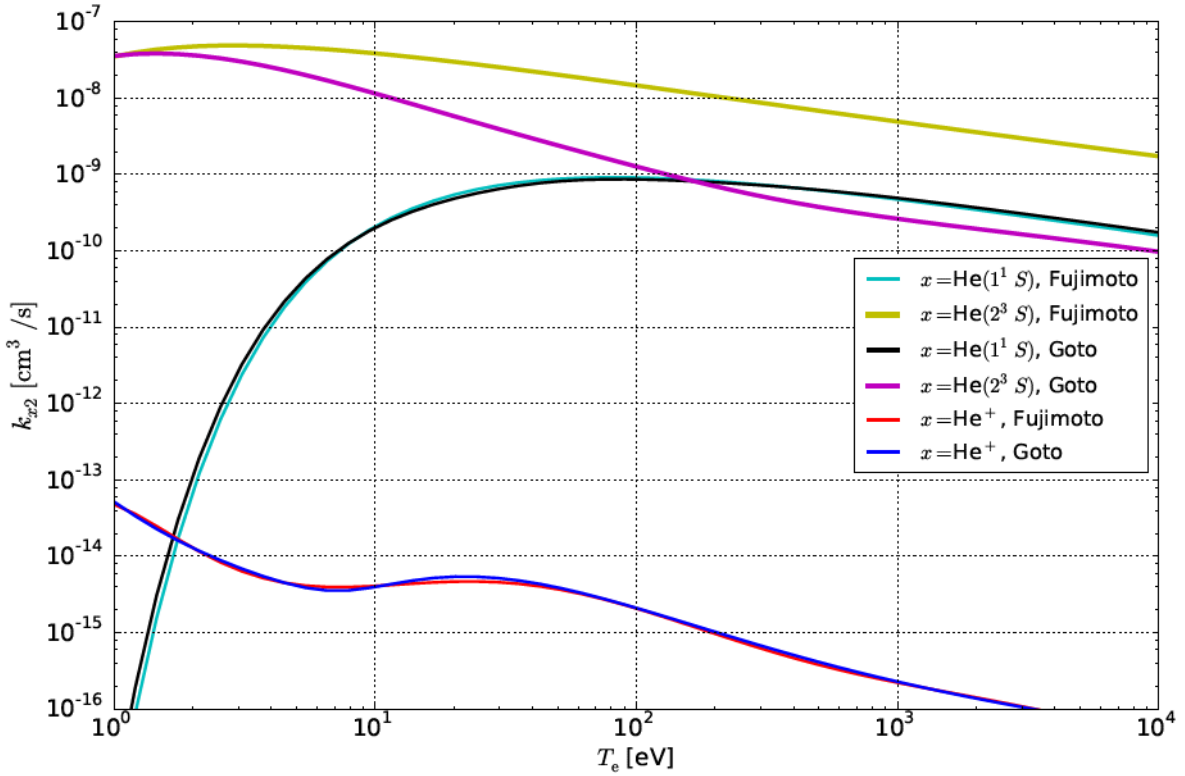

Figure 9: CR coupling coefficients k_{x2} for reactions $x \rightarrow$He(2^1S). Calculated at $n_e = 10^{20}$ m^{-3} by HYDKIN [8]. In formulation I, these are all processes participating in the population of 2^1S.

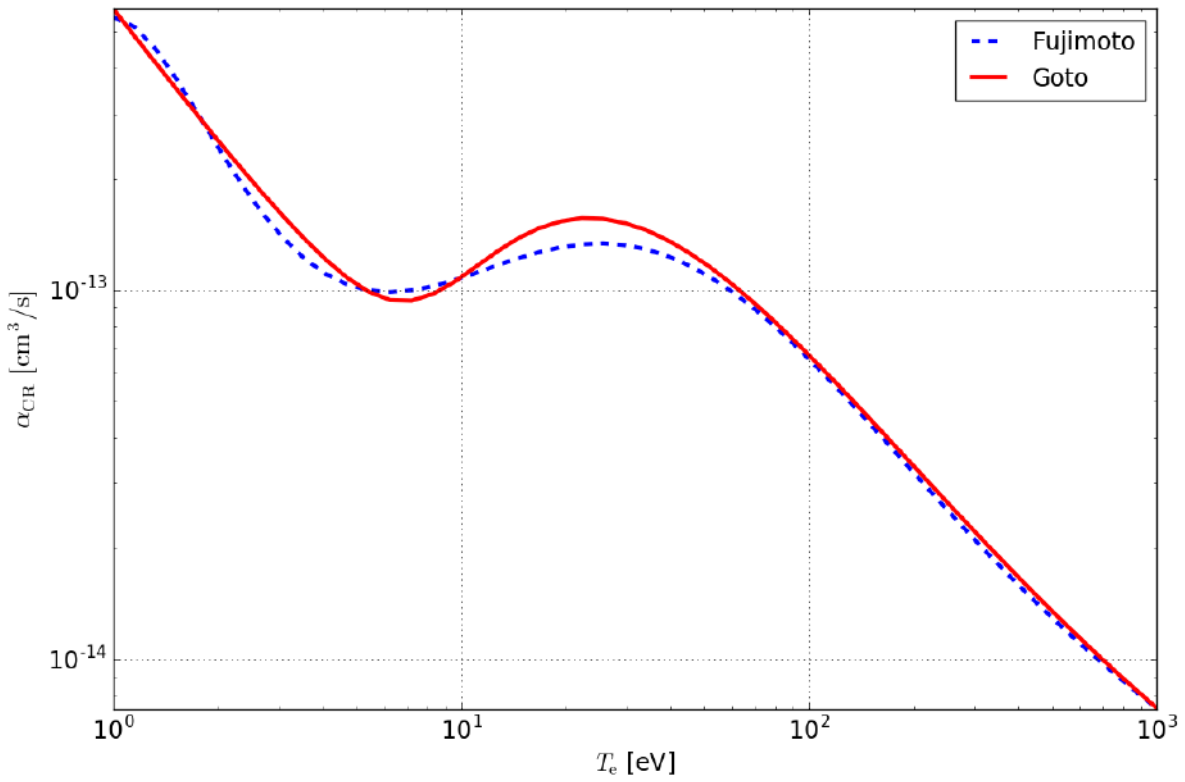

Figure 10: CR recombination coefficient α_{CR} (form. II). Calculated at $n_e = 10^{18}$ m^{-3} by HYDKIN [8].

5.4 Linear sensitivity analysis, error and uncertainty propagation

The equilibrium solution for the collisional-radiative model does not depend on initial conditions. It is rather determined by the reaction rates. For helium, these can be calculated ab initio. However, up to now there is no absolute certainty, especially for higher excited states. The selection and evaluation of the quality of a data set is complicated by the size of the system of equations: with 65 included states, there are 4225 reaction rates, which originate from multiple rate coefficients due to different included processes. This makes a systematic approach necessary.

The simplest model which allows such analysis is the linear error propagation: for a small change in the reaction rates (or generally model parameters) κ_i, the change of the population density of state k is approximated by (the linear therm of the Taylor series)

$$\Delta n_k = \sum_i \frac{\partial n_k}{\partial \kappa_i} \Delta \kappa_i. \tag{43}$$

Eq. (43) already allows the study of propagation of errors in spectral models. But to have a better assessment of the roles of individual parameters, it is advisable to write it in dimensionless units:

$$\frac{\Delta n_k}{n_k} = \sum_i \frac{\kappa_i}{n_k} \frac{\partial n_k}{\partial \kappa_i} \frac{\Delta \kappa_i}{\kappa_i} = \sum_i \varsigma_{ki} \frac{\Delta \kappa_i}{\kappa_i}. \tag{44}$$

In (44), ς_{ki} is called the sensitivity of state k to parameter i. Relative change of the density in state k is given by relative change of all parameters κ_i and the corresponding sensitivities. The $\varsigma_{ki}(t)$ for all 8776 parameters in the He CR model can be calculated analytically by HYDKIN for a homogenious plasma as a function of time [30, 8]: they are derived analytically from the explicit solution of (1). This allows to quantitatively identify most important parameters in a CR model.

While fixed errors with known sign, e.g. real changes between two subsequent models, may be explained with (44), the treatment of uncertainties requires an additional thought. We may assume there exist "real" parameters κ_i with fixed values. Calculations or measurements of these parameters have random errors, so that they are normally distributed around the "real" values. Consequently, uncertainties of a recommended set of κ_i, obtained from many measurements and calculations, lead to an uncertainty of population densities according to

$$\left(\frac{\Delta n_k}{n_k}\right)^2 = \sum_i \varsigma_{ki}^2 \left(\frac{\Delta \kappa_i}{\kappa_i}\right)^2. \tag{45}$$

A linear approach is justified as long as the $\Delta\kappa_i$ are small, and as long as the parameters κ_i are mutually independent. This is certainly not the case, e.g. detailed balance relates the direct and inverse rates. For example, electron impact transition rates are not independent, since $C(p,q)Z(p) = C(q,p)Z(q)$. Certainly, in future, correlations amongst the different reaction rates should be taken into account. For a more detailed model, see [31].

different recombination processes into α_{CR}. In principle, the precision can be drastically increased by separate fitting of dielectronic recombination and others. It is possible, since the CRM is linear.

6 Electron cooling rates

Often, EIRENE [7] is coupled to a plasma fluid code like B2 [9] or EMC3 (edge Monte Carlo 3D) [10] to describe the coupling of the plasma to neutrals. It acts then as a source (and sink) of the fluid due to neutrals, e.g. due to ionization (and recombination) - calculated with a CR model.

It also provides a source (and sink) for the fluid energy and momentum due to the exchange with neutrals. Here, only electron collisions are considered for helium: since $m_e \ll m_i$, momentum exchange can be neglected. The change in energy is expressed with the electron cooling rate density

$$W = \sum_p \Big\{ \chi(p) S(p) n_\mathrm{e} n(p) + \sum_{q \neq p} [\chi(q) - \chi(p)] C(q,p) n_\mathrm{e} n(q) \\ - \chi(p) \alpha(p) n_\mathrm{e}^2 n_\mathrm{i} + W_\beta(p) n_\mathrm{e} n_\mathrm{i} + W_{\beta_\mathrm{d}}(p) n_\mathrm{e} n_\mathrm{i} \Big\}. \tag{46}$$

It has the dimension "energy per time and volume". p and q are hereby energy states of the helium atom as in (1) and χ the ionization potential. $W_\beta(p)$ and $W_{\beta_\mathrm{d}}(p)$ are the rate coefficients associated with the radiative and dielectronic recombination into state p.

The first three terms in (46) are straight forward to explain:

- An electron looses $\chi(p)$ thermal energy by ionizing an atom in state p.
- It looses or gains $\chi(q) - \chi(p)$ thermal energy through a collision, depending on whether it excites or deexcites the atom.
- In the three-body recombination process, one electron recombines with the atom, while the other one gains $\chi(p)$ thermal energy.

The remaining two terms are less obvious. They will be discussed in the following section.

6.1 Cooling due to radiative and dielectronic recombination

In both cases, energy is emitted via photons – but not only the binding energy $\chi(p)$. The fluid also loses heat equal to the kinetic energy of the now bound electrons. We can express β and β_d with (20). The according, ensemble averaged cooling rate coefficients are therefore

$$W_\beta(p) = \langle E_\mathrm{kin} \sigma_\beta(p) v \rangle = \frac{1}{2} m_\mathrm{e} \int \sigma_\beta(p) v^3 f_M(v) \mathrm{d}v, \tag{47}$$

and similarly for $W_{\beta_\mathrm{d}}(p)$ with $\sigma_{\beta_\mathrm{d}}(p)$.

Now, looking at equation (19) we notice

$$\frac{\partial f_M}{\partial T} = \left(\frac{m v^2}{2T^2} - \frac{3}{2} \frac{1}{T} \right) f_M$$

and therefore

$$\frac{\partial \langle \sigma v \rangle}{\partial T} = \int \sigma v \frac{\partial f_M}{\partial T} \mathrm{d}v = \frac{\langle E_\mathrm{kin} \sigma v \rangle}{T^2} - \frac{3}{2} \frac{1}{T} \langle \sigma v \rangle, \tag{48}$$

hence (ln being the natural logarithm)

$$\langle E_{\rm kin}\sigma v\rangle = \frac{3}{2}T\langle\sigma v\rangle + T^2\frac{\partial\langle\sigma v\rangle}{\partial T} = \langle\sigma v\rangle T\left[\frac{3}{2}+\frac{\partial\ln\langle\sigma v\rangle}{\partial\ln T}\right]. \tag{49}$$

We can therefore express (47) as

$$W_\beta(p) = T\left[\frac{3}{2}+\frac{\partial\ln\beta(p)}{\partial\ln T}\right]\beta(p), \tag{50}$$

a relation which is widely used in the EIRENE code for electron energy sink term estimation.

6.1.1 Dielectronic cooling

In the atomic data G2012 [1], we have (with $Ry =$ the Rydberg constant)

$$\beta_{\rm d}(p) \sim T^{-\frac{3}{2}}\exp\left(\frac{\chi(p)-3Ry}{T}\right) \Rightarrow \frac{3}{2}+\frac{\partial\ln\beta_{\rm d}(p)}{\partial\ln T} = \frac{3Ry-\chi(p)}{T}, \tag{51}$$

and therefore simply

$$W_{\beta_{\rm d}}(p) = \left[3Ry-\chi(p)\right]\beta_{\rm d}(p). \tag{52}$$

6.1.2 Radiative cooling

The dependence of the radiative recombination on temperature is more difficult. Therefore, another approach was taken: the rate was fitted logarithmically by an eighth order polynomial

$$\ln\beta(p) = \sum_{n=0}^{8} a_n(p)\,(\ln T)^n. \tag{53}$$

The fit was easily done using numpy.polyfit[†], with mean error below $5\cdot10^{-6}$ and maximal error of 1%. It is then simple to derive

$$W_\beta(p) = T\left[\frac{3}{2}+\sum_{n=1}^{8} a_n(p)n\,(\ln T)^{n-1}\right]\beta(p). \tag{54}$$

However, it turns out that often $W_\beta(p) < 0$ above a certain temperature. For some states p, the zero point temperature is even below 10 eV. This is non-physical, because all quantities in (47) are positive: since continuum electrons have positive energy, we expect cooling (and not heating) if they are lost. The ensemble averaging gives wrong results when

$$\frac{\partial\ln\beta(p)}{\partial\ln T} < -\frac{3}{2}. \tag{55}$$

Apparently, the cross section gradients are too steep for higher temperatures. Assuming only moderate errors, we set $W_\beta(p,T) = 0$ in such cases. However, a verification of the atomic cross sections is needed.

[†]NumPy is a package for scientific computing with Python, see `https://docs.scipy.org/doc/numpy/reference/generated/numpy.polyfit.html` (last visited on 28.03.17).

6.2 Cooling in formulation I and II, comparison to F1979 [2]

6.2.1 Derivation

Having the expression in (46) fully defined, we notice that it depends on the helium population (and ion) density. Hence, a solution for the rate equation (1) is required. Naturally, we want to use the approximate solutions from formulation I or II: we insert (2) for $n \geq 21$ (Saha states), for $n < 21$ and $q \notin \{1^1S, 2^1S, 2^3S\}$ we use (7) in form. I or (9) for $q \neq 1^1S$ in form. II. We obtain

$$W = W_0^{\mathrm{I}} n_e n_i + W_1^{\mathrm{I}} n_e n(1^1S) + W_2^{\mathrm{I}} n_e n(2^1S) + W_3^{\mathrm{I}} n_e n(2^3S) \tag{56}$$

in formulation I and

$$W = W_0^{\mathrm{II}} n_e n_i + W_1^{\mathrm{II}} n_e n(1^1S) \tag{57}$$

in formulation II.

Explicitly, in form. I the cooling rate coefficients are

$$W_j^{\mathrm{I}} = \sum_p \left\{ \chi(p) S(p) n_e r_j(p) + \sum_{\substack{q \neq p \\ n<21}} [\chi(q) - \chi(p)] C(q,p) n_e r_j(p) \right\} \text{ for } j \in \{1,2,3\}, \tag{58}$$

$$\begin{aligned} \text{and } W_0^{\mathrm{I}} = \sum_p \Bigg\{ & \chi(p) S(p) n_e r_0(p) + \sum_{\substack{q \neq p \\ n<21}} [\chi(q) - \chi(p)] C(q,p) n_e r_0(p) \\ & - \chi(p) \alpha(p) n_e + W_\beta(p) + W_{\beta_\mathrm{d}}(p) + \sum_{\substack{q \neq p \\ n \geq 21}} [\chi(q) - \chi(p)] C(q,p) n_e Z(q) \Bigg\}. \end{aligned} \tag{59}$$

In form. II, $W_0^{\mathrm{II}} \mathrel{\hat{=}} W_0^{\mathrm{I}}$ with $R_0(p)$ instead of $r_0(p)$, and $W_1^{\mathrm{II}} \mathrel{\hat{=}} W_j^{\mathrm{I}}$ with $R_1(p)$ instead of $r_j(p)$.

6.2.2 Temperature dependence

The cooling rate coefficients for both formulations are plotted on a temperature scale in Figure 11. Note: for electron impact transition rates, the database V2005 [18] was used. Ion cooling W_0 changes the sign at low T_e (below the "resonance") and high n_e due to three-body recombination heating. The meta-stable cooling rates $W_{2,3}^{\mathrm{I}}$ also become negative at low T_e. Therefore, (in the logarithmic plot) we display their absolute value.

The increase of the ion cooling at higher temperatures is unexpected, since the rates fall off exponentially. According to chapter 6.1.2, we set $W_\beta = 0$ above a certain temperature, so that the cause can only lie in dielectronic recombination. This indicates, that the dielectronic recombination data may also be inappropriate for higher temperatures.

We notice that $W_0 \ll W_j \; \forall \; T_\mathrm{e} > 1$ eV. Hence, ion cooling is only important if $n_\mathrm{i} \gg n_j$.

Further, we note that $W_1^{\mathrm{II}} \approx W_1^{\mathrm{I}} \; \forall \; T_\mathrm{e}$ and $W_0^{\mathrm{II}} \approx W_0^{\mathrm{I}} \; \forall \; T_\mathrm{e} > 10$ eV. This is because $n(2^{1,3}S) \ll n(1^1S)$ holds for most near equilibrium situations. Thus formulation II is a very appropriate approximation. Yet, since $W_{2,3} > W_1 \; \forall \; T_\mathrm{e} > 1$ eV, formulation I should be used in non-equilibrium cases.

6.2.3 Comparison with original data set F1979 [2]

Since the model in [1] is an update of [2], it is natural to compare the two. In general, the difference is small: for $T_\mathrm{e} > 10$, we observe a 5% difference for W_0 and W_1, and 20% for W_2 and

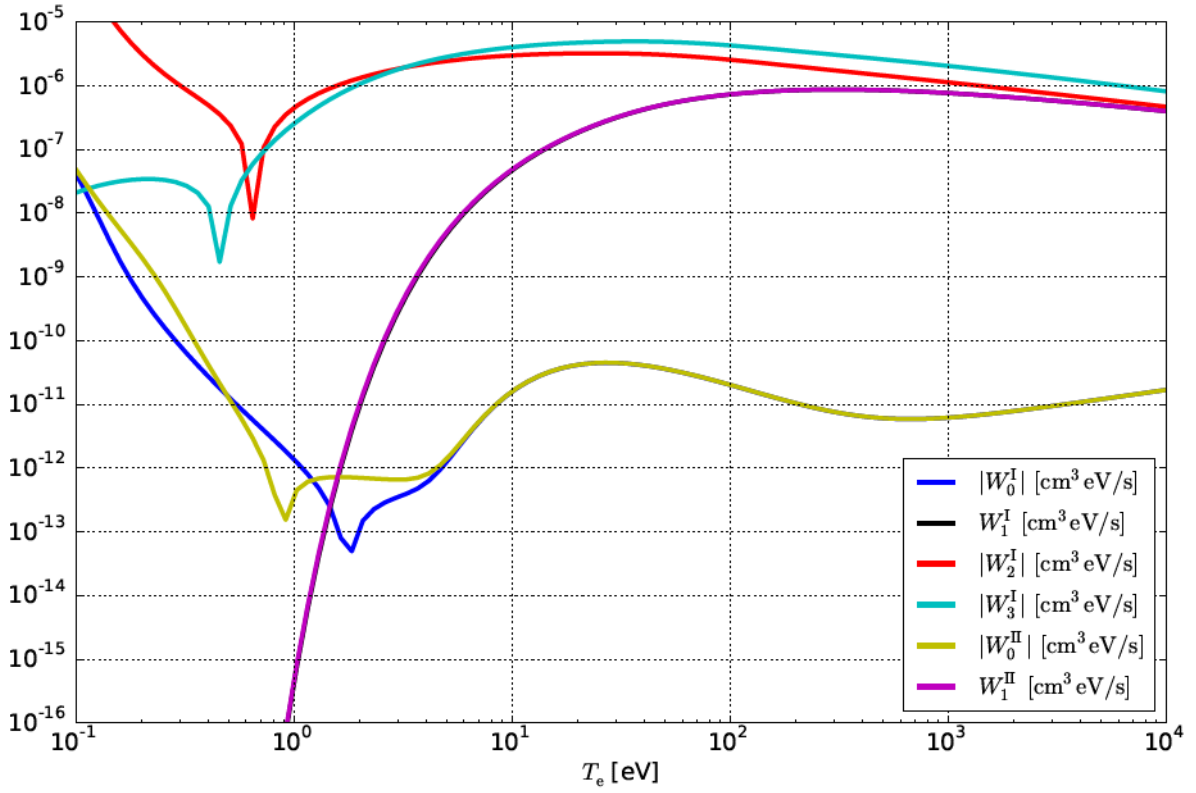

Figure 11: Cooling rate coefficients in formulations I and II. $n_e = 10^{20}$ m^{-3}. $W_{1,2,3}$ are nearly constant in n_e. W_0 varies with n_e at small temperatures, because of the n_e^2 dependency of three-body recombination. For electron impact transition rates, the V2005 [18] database was used.

W_3. The singlet meta-stable coefficient is plotted in Figure 12. We do not expect any change for plasma cooling calculations because W_0 and W_1 are usually the dominant cooling processes.

An important note is further, that the singlet-triplet state mixing implemented in G2012 [1] does not seem to noticeably affect the cooling rates. W_3 changes the most by 2% at 7.3 T, but otherwise the difference is below 1%.

6.3 Radiative loss rates

Similarly to the cooling rate, we can define the radiative loss rate

$$W_{\mathrm{rad}} = \sum_p \left\{ \sum_{q>p} [\chi(q) - \chi(p)] A(q,p) n(q) - \left\langle (\frac{1}{2} m_e v^2 + \chi(p))(\sigma_\beta + \sigma_{\beta_d}) v \right\rangle \right\}. \tag{60}$$

$q > p$ means that state q lies energetically higher than state p. The second term accounts for the photons mentioned in chapter 6.1. Note: $W_{\mathrm{rad}} < 0$. Like the cooling rate, it can be computed using formulation I or II, hence

$$W_{\mathrm{rad}} = W^{\mathrm{I}}_{\mathrm{rad}_0} n_e n_i + W^{\mathrm{I}}_{\mathrm{rad}_1} n_e n(1^1S) + W^{\mathrm{I}}_{\mathrm{rad}_2} n_e n(2^1S) + W^{\mathrm{I}}_{\mathrm{rad}_3} n_e n(2^3S) \tag{61}$$

and

$$W_{\mathrm{rad}} = W^{\mathrm{II}}_{\mathrm{rad}_0} n_e n_i + W^{\mathrm{II}}_{\mathrm{rad}_1} n_e n(1^1S). \tag{62}$$

Due to energy conservation, the plasma's thermal energy change (cooling/heating) must be balanced by change of the internal state (atomic level transition) and radiation. This also holds in the reduced formulations, hence

$$W_i = \sum_{j \neq i} [\chi(i) - \chi(j)] k_{ij} - W_{\mathrm{rad}_i}. \tag{63}$$

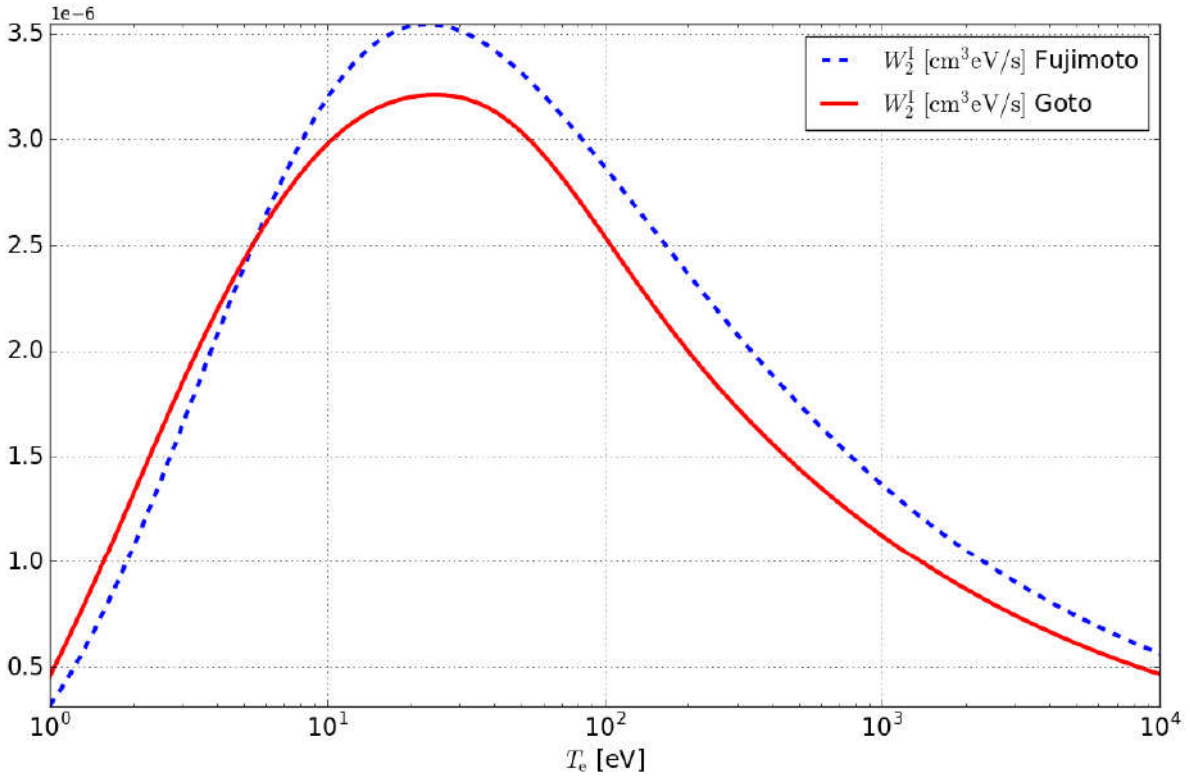

Figure 12: Singlet meta-stable cooling rate coefficient in formulation I, by Fujimoto [2] and by Goto [1]. $n_e = 10^{20}$ m^{-3}. In G2012 [1], for electron impact transition rates, the V2005 database [18] was used.

In form. II, S_{CR} and α_{CR} are meant by k_{ij}.

For small temperatures, W_0 and $W^I_{2,3}$ may change their sign. This is unfortunate if the rates should be stored logarithmically. Therefore, $-W_{\mathrm{rad}_{0,2,3}}$ is stored instead, which is equivalent due to (63) and always positive.

6.3.1 Verification of the code

Relation (63) was used in the original F1979 code [2] to verify the implementation. At least for formulation II, it also holds in the new implementation in G2012 [1]. Besides, the results were compared between the codes, using the same atomic data, and were found to agree. Therefore, the implementation is verified.

7 Application to beam emission spectroscopy

7.1 Line intensity ratios from formulation II

The goal of the beam emission spectroscopy (BES) is to determine plasma parameters T_e and n_e from the radiation emitted by the beam during ionization. The observed line intensity (in photons per second) for a transition $p \to q$ is given by

$$I(p,q) = n(p)A(p,q)V(\mathrm{d}\Omega/4\pi) \quad [11]. \tag{64}$$

$V(\mathrm{d}\Omega/4\pi)$ is the observed plasma volume. It depends on the angle $\mathrm{d}\Omega$ given by the optics. To make the diagnostic less vulnerable to the calibration of the optical system, it is convenient to use intensity ratios between neighboring lines

$$R_I = \frac{n(p_1)A(p_1,q_1)}{n(p_2)A(p_2,q_2)}. \tag{65}$$

Ideally, one finds two ratios which predominantly depend on only one different plasma parameter. A common choice, proposed by [5], is

$$R_{T_e} = \frac{I(728.1\,\mathrm{nm})}{I(706.5\,\mathrm{nm})} = \frac{n(3^1S)A(3^1S \to 2^1P)}{n(3^3S)A(3^3S \to 2^3P)} \tag{66}$$

and

$$R_{n_e} = \frac{I(667.8\,\mathrm{nm})}{I(728.1\,\mathrm{nm})} = \frac{n(3^1D)A(3^1D \to 2^1P)}{n(3^1S)A(3^1S \to 2^1P)}. \tag{67}$$

Since $A(p,q)$ is constant in T_e and n_e, important for the determination of these parameters is actually the proportionality to $n(p_1,T_e,n_e)/n(p_2,T_e,n_e)$. The population densities can be computed using equations (7) or (9). However, therefor the P space densities must be known. They can be obtained in a simulation, e.g. using the EMC3/EIRENE [10] code, but in the experiment usually additional approximations are used:

- Quasi-steady-state is assumed for the meta-stable states, allowing to use formulation II. This is often justified with long enough camera integration times, but can become difficult if additional effects on smaller time scales must be considered.
- Ionizing plasma is assumed, allowing to neglect $R_0(q)n_en_i$ in (9). This is justified for a helium beam in the hydrogen scrape-off layer (SOL) plasma, since $R_0 << R_1$ in a wide parameter range and accumulation of He^+ ions is limited by transport losses. However, it might be a problem in a recombining divertor plasma, where $R_0 \approx R_1$.

These assumptions allow us to write

$$R_I = \frac{A(p_1,q_1)R_1(p_1)}{A(p_2,q_2)R_1(p_2)}. \tag{68}$$

In eq. (68) even the ground state dependence cancels. This means, the solution is determined only by the system of linear equations (SLE) - it is computationally undemanding, but also completely stationary. An easy way to relax this condition is to incorporate the QSS assumption for the ground state into the SLE.

Because of the above assumptions, we can set $R_0(q) = 0$ in eq. (9) and $\alpha_{CR} = 0$ in eq. (10). The solution for (10) is then simply

$$n_{1^1S}(t) = n_0 e^{-S_{CR}n_e t} \tag{69}$$

and with it from (9) follows

$$\dot{n}(q) = -S_{\mathrm{CR}} n_{\mathrm{e}} n(q). \tag{70}$$

This conclusion is valid if formulation II with the above assumptions can be used and $n(1^1S)$ is given by (69). It is similar to the assumption by Brix [3, eq. (2.12)]. But, it is not true for eq. (68) since the ground state dependence cancels there. The behaviour in (70) can be enforced for the intensity ratios in the same way as in [3] by

$$\mathbf{M} \rightarrow \mathbf{M} + S_{\mathrm{CR}} n_{\mathrm{e}}. \tag{71}$$

The results of G2012 CR code in formulation II are then the same as from [3, eq. (2.13)]. Only then, assuming eq. (69) is valid, the line intensity ratios given by (68) are correctly coupled to the ground state. In contrast to [3, eq. (2.12)], by using S_{CR} instead of $S(1^1S)$ the procedure is also valid below 10 eV.

7.2 Results and comparison to [3]

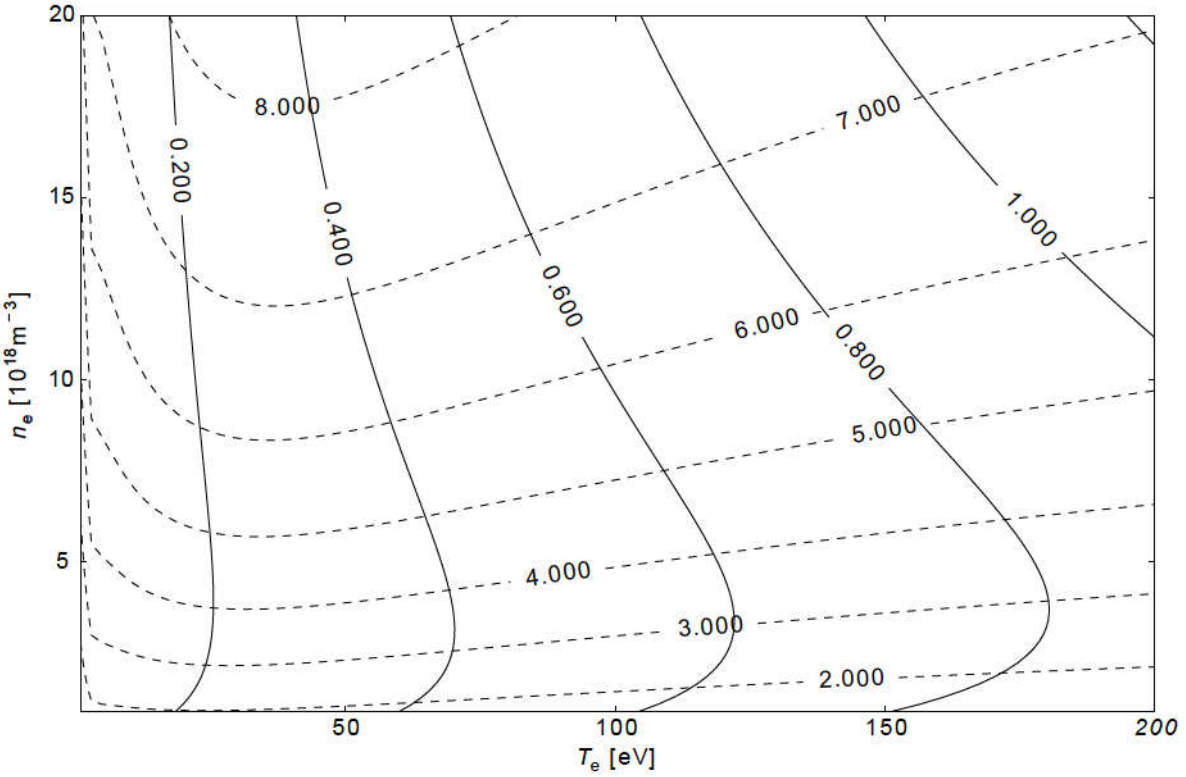

Figure 13: Line intensity ratios computed from G2012 CR model [1] at $B = 2.5$ T, formulation II, modified by eq. (71). Solid line – $R_{T_e} = I(728.1\,\mathrm{nm})/I(706.5\,\mathrm{nm})$, dashed – $R_{n_e} = I(667.8\,\mathrm{nm})/I(728.1\,\mathrm{nm})$. For electron impact transition rates, the database V2005 [18] was used in G2012.

In Figure 13, the temperature and density dependent line intensity ratios R_{T_e} and R_{n_e} are plotted. They were computed according to chapter 7.1 in the same plasma parameter range as in [3]. The magnetic field is set to $B = 2.5$ T, according to the conclusions drawn from chapter 4 for W7-X. For electron impact transition rates, the database V2005 [18] was used here.

A significant discrepancy, compared to Figure 14 from [3, fig. 2.4], is observed, especially in R_{T_e}. At $B = 0$, it would be even a little larger. Omitting the correction from equation (71) would lead to slightly better agreement. In [32] it is reported that model [3] may underestimate the

plasma parameters, compared to a newer CR model by Muñoz Burgos [33], due to different atomic data.

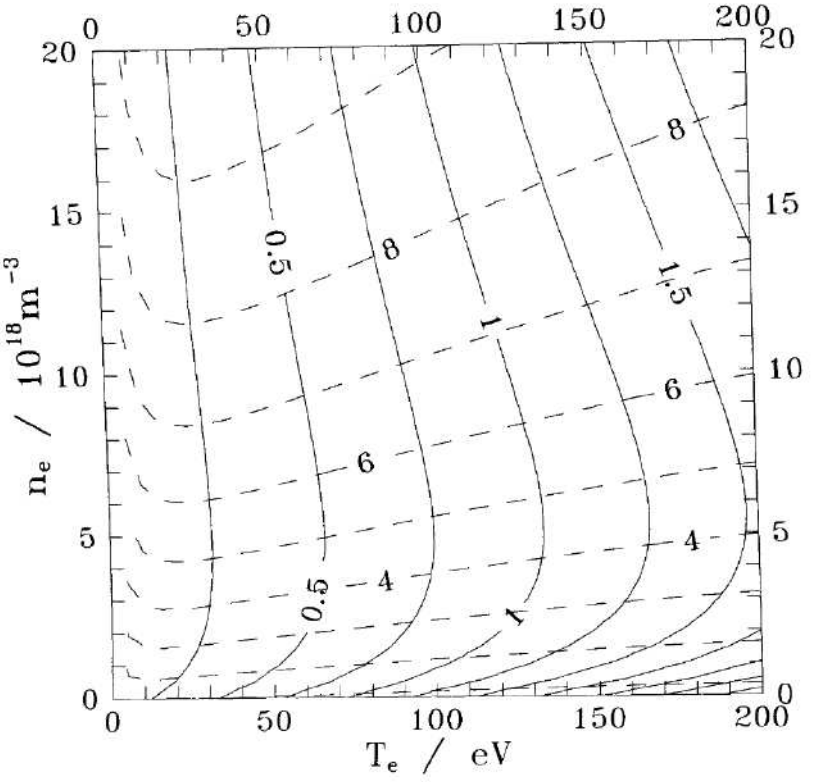

Figure 14: Line intensity ratios from [3, fig. 2.4]. Solid line – $R_{T_e} = I(728.1\,\text{nm})/I(706.5\,\text{nm})$, dashed – $R_{n_e} = I(667.8\,\text{nm})/I(728.1\,\text{nm})$.

The discrepancy becomes even larger if we consider the same number of 29 atomic levels as in [3]. Since higher L states are grouped together in our model, we include the first 27 states up to $n = 5$. This leads to Figure 15: at $R_{n_e} = 7.5$ and $R_{T_e} = 0.5$ we see a factor 3 difference in T_e. The only significant difference to Figure 14 are the atomic data.

These results demonstrate the importance of higher n states. In fact, adding subsequent n shells one by one (from $n = 5$ to $n = 26$) continuously turns fig. 15 into fig. 13.

From this we conclude that the deviation in atomic data between [3] and newer CR models may have been underestimated due to additional effects incorporated in those. Especially, the inclusion of higher n levels in [1] seems to partially disguise the impact of newer atomic data. Omitting the correction from equation (71) (which is not recommended for BES) and including singlet-triplet state mixing (recommended) further (coincidentally?) reduces the discrepancy.

To calculate R_{T_e} and R_{n_e} without knowledge about the actual ground state population density we assumed ionizing plasma. A significant recombining plasma component is actually very unfavorable for the BES: in Figure 16, line intensity ratios are plotted for a purely recombining plasma. They can be computed by exchanging $R_1(p)$ by $R_0(p)$ in (68). The determination of T_e and n_e from such spectra becomes very imprecise or even ambiguous, because the line ratios are not orthogonal any more. To determine whether the recombining plasma component becomes important, the actual population density of ground state helium compared to helium ion density must be known - it can be determined by a synthetic diagnostic, but may be difficult to measure.

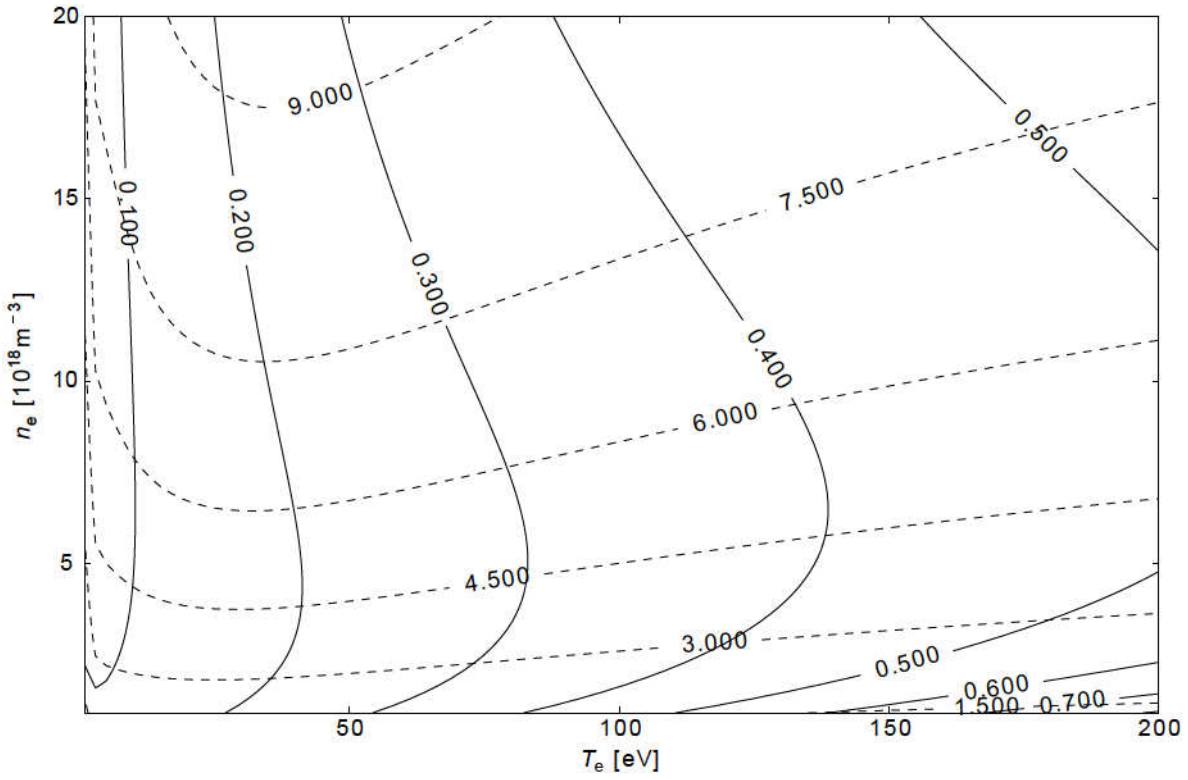

Figure 15: Line intensity ratios with only 29 helium states, compared to Figure 13. Solid line – $R_{T_e} = I(728.1\,\text{nm})/I(706.5\,\text{nm})$, dashed – $R_{n_e} = I(667.8\,\text{nm})/I(728.1\,\text{nm})$.

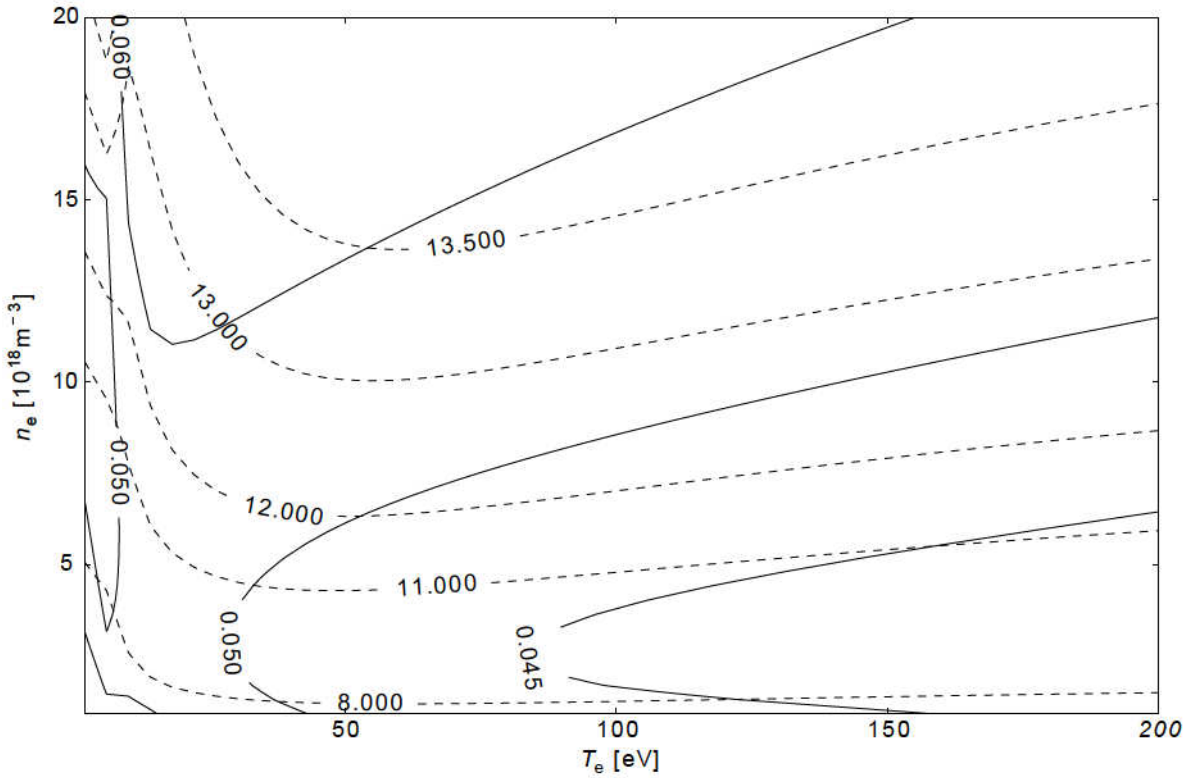

Figure 16: Line intensity ratios for the recombining plasma component $R_0(p)$. Computed from G2012 CR model [1] at $B = 2.5$ T, formulation II, modified by eq. (71). Solid line – $R_{T_e} = I(728.1\,\text{nm})/I(706.5\,\text{nm})$, dashed – $R_{n_e} = I(667.8\,\text{nm})/I(728.1\,\text{nm})$. For electron impact transition rates, the database V2005 [18] was used in G2012.

7.3 Results with electron impact transition data R2008 [4]

As described in chapter 3.2, results obtained with electron impact transition data V2005 [18] are not satisfying since we could not obtain a reliable reference for them. Instead, recently, we were able to reliably integrate the full set of cross section data R2008 [4] and we recommend to use them in the experimental studies. The impact of the choice of the underlying database can be well demonstrated with line intensity ratios, and hence, this is done in this section.

As described in section 3.2.3, the first step was to make the complete data set from [4] integrable. For $T_e < 200$ eV, this was possible with the pre-implemented 'gsl_integration_qagiu' routine [23] by applying linear extrapolation with $x_0 = 0.6$ eV / ΔE for the transition $4^1D \rightarrow 4^1F$, and $x_0 = 0.192$ eV / ΔE for $4^3D \rightarrow 4^3F$. The result is depicted in fig. 17, with a logarithmic density scale. Such a CR model would not be applicable in the experiment, because it is not reversible at all for $T_e < 30$ eV (due to the non-monotonous temperature dependence of the 'density-dependent' line ratio).

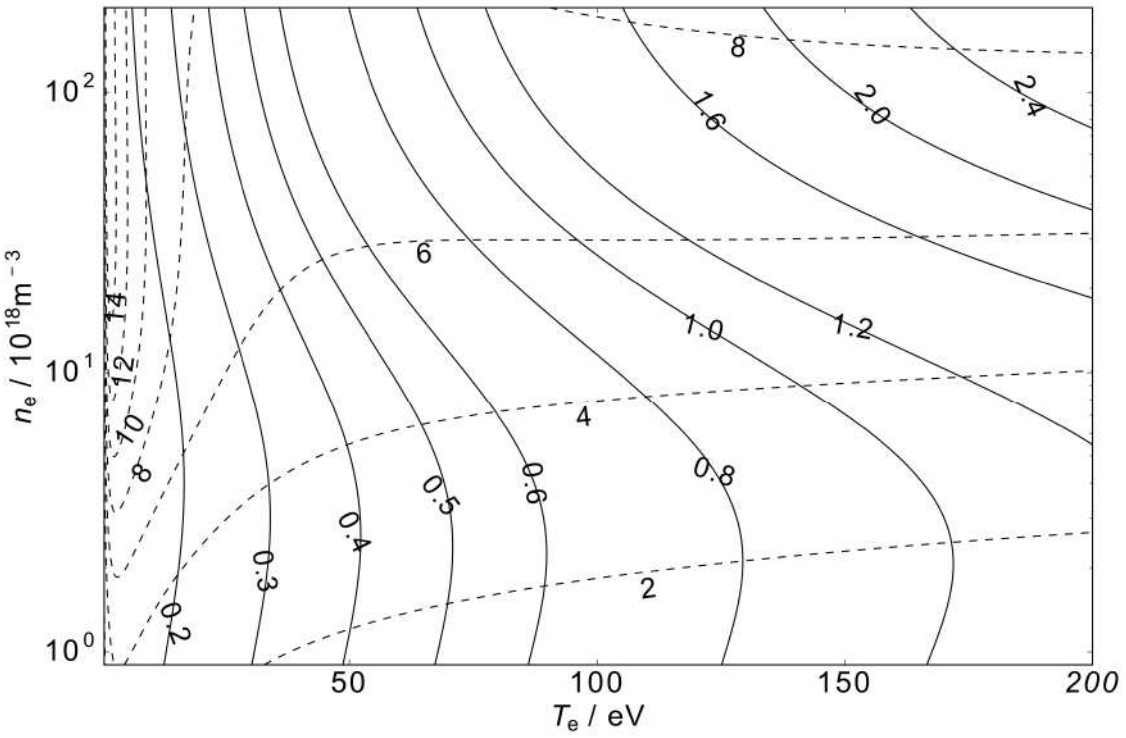

Figure 17: Line intensity ratios computed from G2012 CR model [1] at $B = 2.5$ T, formulation II, modified by eq. (71). Solid line – $R_{T_e} = I(728.1\,\text{nm})/I(706.5\,\text{nm})$, dashed – $R_{n_e} = I(667.8\,\text{nm})/I(728.1\,\text{nm})$. For electron impact transition rates, the R2008 [4] database was used. $4^{1,3}D \rightarrow 4^{1,3}F$ transition rates modified below 1 eV to allow integration with the 'gsl_integration_qagiu' routine.

While investigating the behavior of the line intensity ratios in Figure 17, we found two 'bugs' in the CR model: the electron impact transition cross sections were indeed corrupted at $E \lesssim 0.1$ eV, and the integration routine 'gsl_integration_qagiu' from the GSL library [23] was not optimal for their integration. Therefore, we have applied a linear extrapolation for the fits below 0.1 eV, and have implemented 64-points Gauss-Laguerre integration. This is described in chapter 3.2.3 in more detail. The resulting line intensity ratios are depicted in Figure 18 and are much better suited for the experimental application.

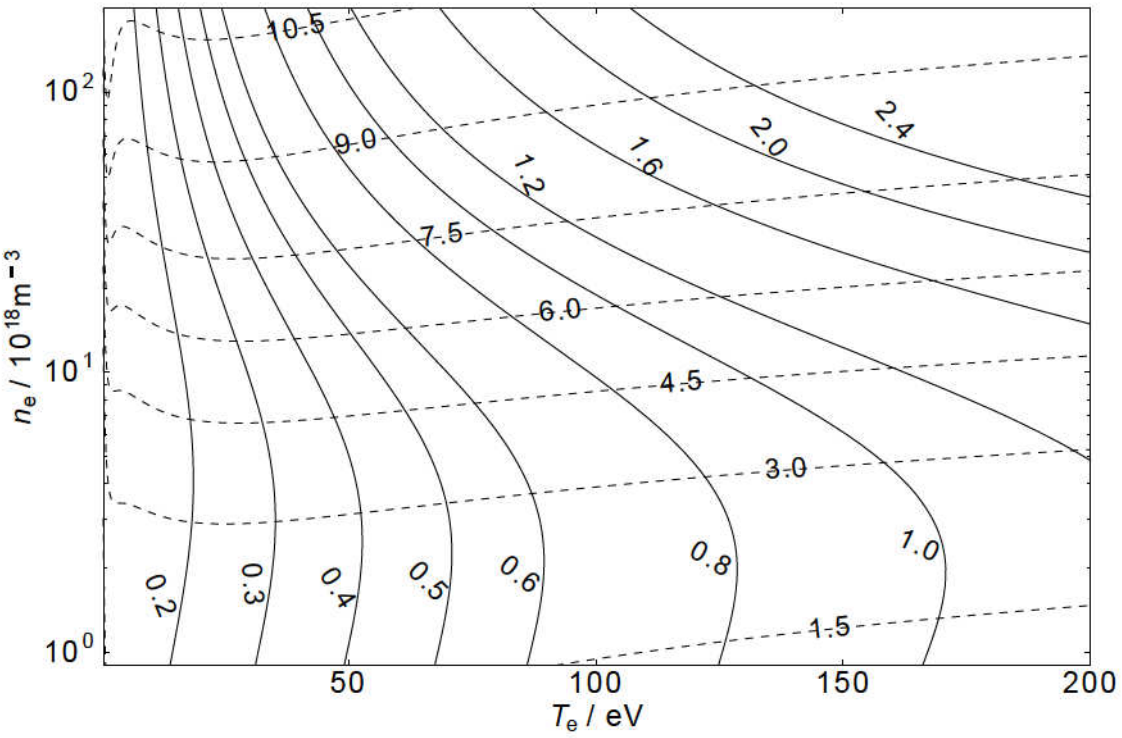

Figure 18: Line intensity ratios computed from G2012 CR model [1] at $B = 2.5$ T, formulation II, modified by eq. (71). Solid line – $R_{T_e} = I(728.1\,\text{nm})/I(706.5\,\text{nm})$, dashed – $R_{n_e} = I(667.8\,\text{nm})/I(728.1\,\text{nm})$. For electron impact transition rates, the R2008 [4] database was used. Collision strength fits were corrected below 0.1 eV. For integration, Gauss-Laguerre quadrature is suggested. Same results can be obtained with GSL integration (not recommended) – but minor additional changes to fits are necessary (see chapter 3.2.3).

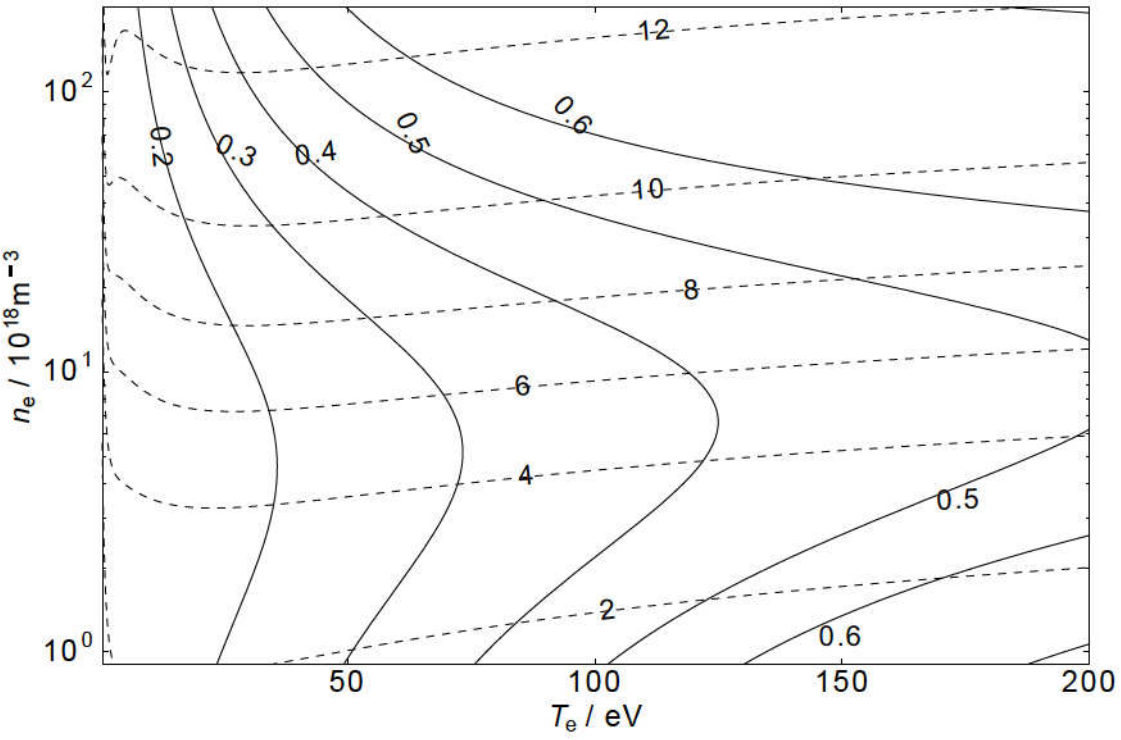

Figure 19: Line intensity ratios with only 29 helium states, compared to Figure 18. Solid line – $R_{T_e} = I(728.1\,\text{nm})/I(706.5\,\text{nm})$, dashed – $R_{n_e} = I(667.8\,\text{nm})/I(728.1\,\text{nm})$.

The difference to CR model [3] (between Figure 18 and 14) in R_{T_e} is now smaller, compared to when data set V2005 is used (Figure 13). But the discrepancy in R_{n_e} is now larger: looking at $n_e \approx 10^{19}$ m^{-3}, we have $R_{n_e} \approx 7$ in fig. 14 (from [3, fig. 2.4]), $R_{n_e} \approx 6$ in fig. 13 (G2012 with C rates V2005) and $R_{n_e} \approx 5$ in fig. 18 (G2012 with C rates R2008). Which one is closer to reality can not be determined in the present work. It is difficult to determine in the experiment either, since many other factors can cause a deviation from theory, too.

The discrepancy in R_{n_e} between [3, fig. 2.4], G2012 with V2005 data and G2012 with R2008 data becomes significantly smaller, if in the latter two only the lowest 29 energy eigenstates are retained. However, Figure 19 demonstrates that, also with electron impact transition rates from [4], the reduction of the number of energy eigenstates messes up the temperature dependent line ratio R_{T_e}.

7.4 Line intensity ratios from formulation I

If the assumptions for form. II are not fulfilled, a more complicated model must be used. It is often observed in plasmas with smaller collisionalities that the triplet-meta-stable state is not in equilibrium [3, 2, 33, 34] - which in our CR model calls for the use of formulation I.

Unfortunately, even if recombination is negligible, the ground state dependence does not cancel in this case:

$$R_I = \frac{A(p_1,q_1)}{A(p_2,q_2)} \frac{r_0(p_1) n_e n_i + r_1(p_1) n_e n(1^1S) + r_2(p_1) n_e n(2^1S) + r_3(p_1) n_e n(2^3S)}{r_0(p_2) n_e n_i + r_1(p_2) n_e n(1^1S) + r_2(p_2) n_e n(2^1S) + r_3(p_2) n_e n(2^3S)} \tag{72}$$

$$\approx \frac{A(p_1,q_1)}{A(p_2,q_2)} \frac{r_1(p_1) + r_2(p_1) n(2^1S)/n(1^1S) + r_3(p_1) n(2^3S)/n(1^1S)}{r_1(p_2) + r_2(p_2) n(2^1S)/n(1^1S) + r_3(p_2) n(2^3S)/n(1^1S)}. \tag{73}$$

Apart from T_e and n_e, this model now has two additional parameters: relative population densities of the meta-stable states, $n(2^1S)/n(1^1S)$ and $n(2^3S)/n(1^1S)$. Since in form. I we explicitly state that the meta-stable states are not in equilibrium with the ground state, these ratios are not easy to determine. Therefore, the results cannot be illustrated as in section 7.2.

7.5 Identifying crucial transitions via error propagation

The sensitivity analysis introduced in chapter 5.4 can be also done for line intensity ratios. This is independent of approximations which lead to form. I or II, since HYDKIN computes sensitivities ς_{ki} from an analytic solution of (1). The correlation between $A(p,q)$ and the population densities would make the approach tricky. But the uncertainty in the Einstein's coefficients is very small, compared to those of electron impact processes. Therefore, we assume $\Delta A(p_1,q_1)/A(p_1,q_1) \approx 0$. Then, we simply apply the chain rule to eq. (65) and use (44):

$$\frac{\Delta R_I}{R_I} = \frac{n(p_1)}{R_I} \frac{\partial R_I}{\partial n(p_1)} \frac{\Delta n(p_1)}{n(p_1)} + \frac{n(p_2)}{R_I} \frac{\partial R_I}{\partial n(p_2)} \frac{\Delta n(p_2)}{n(p_2)}$$

$$= \sum_i (\varsigma_{p_1 i} - \varsigma_{p_2 i}) \frac{\Delta \kappa_i}{\kappa_i}. \tag{74}$$

In (74), the correlation between $n(p_1)$ and $n(p_2)$ was also neglected. The propagation of uncertainties can be calculated via

$$\left(\frac{\Delta R_I}{R_I}\right)^2 = \sum_i (\varsigma_{p_1 i} - \varsigma_{p_2 i})^2 \left(\frac{\Delta \kappa_i}{\kappa_i}\right)^2, \tag{75}$$

but was not undertaken so far due to technical reasons.

One possible application of such a sensitivity analysis is the investigation of differences between different models: it allows us to track the differences in the experimental application (line intensity ratios) explicitly back to individual reaction rates. This is demonstrated here for the CR models F1979 [2] and G2012 [1].

At $T_e = 175$ eV and $n_e = 10^{19}$ m^{-3} we have $\Delta R_{T_e}/R_{T_e} = (R_{T_e,\mathrm{F1979}} - R_{T_e,\mathrm{G2012}})/R_{T_e,\mathrm{G2012}} = 0.77$. Now we calculate relative sensitivities $\Delta\varsigma_i = \varsigma_{3^1S,i} - \varsigma_{3^3S,i}$ and the differences in reaction rates $\Delta\kappa_i/\kappa_i = (\Delta\kappa_{i,\mathrm{F1979}} - \Delta\kappa_{i,\mathrm{G2012}})/\Delta\kappa_{i,\mathrm{G2012}}$. Investigating individual terms i tells us about the individual reaction rates, responsible for the deviation. Here, we focus on ionization rates, because they have changed most significantly (see chapter 3.2.1): in fact, the sum over i in fig. 20 according to (74) already gives 0.67.

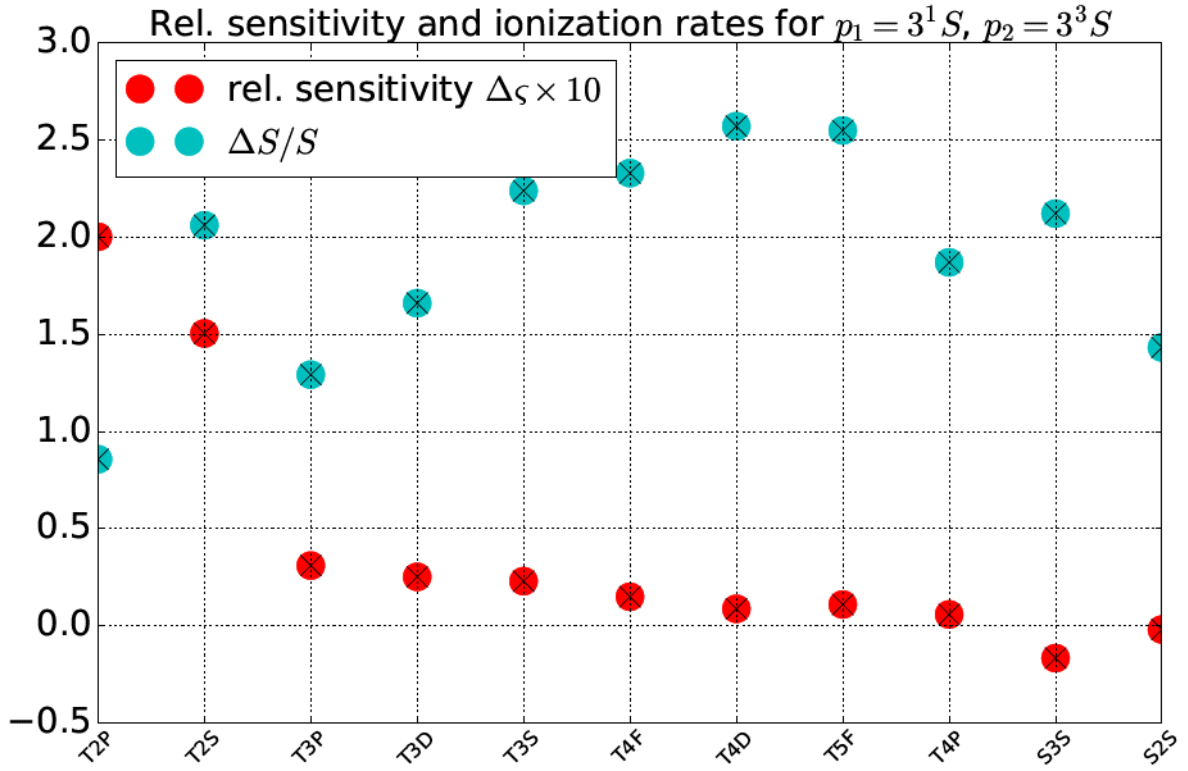

Figure 20: Sensitivity analysis at $T_e = 175$ eV and $n_e = 10^{19}$ m^{-3}. $\Delta\varsigma_i = \varsigma_{3^1S,i} - \varsigma_{3^3S,i}$ is scaled by a factor 10. $i = \tilde{S}nL$, with $\tilde{S}$ =S for singlet and $\tilde{S}$ =T for triplet, is on the x-axis. $\Delta S/S = (S_{\mathrm{F1979}} - S_{\mathrm{G2012}})/S_{\mathrm{G2012}}$.

The analysis reveals that 0.48 of the deviation in the temperature dependent line intensity ratio (62%) is caused by two reaction rates: the ionization from 2^3P and 2^3S. Another 0.19 come together due to other ionization rates, mainly in the triplet system, as shown in fig. 20. The remaining 0.1 are due to other reaction rates.

Note that the sensitivities were computed with reaction rates from G2012 with V2005. The linear approximation demands only small $\Delta\kappa/\kappa$, which is not true here. Since with significantly different reaction rates also the sensitivities change, our approach may give imprecise results.

Nevertheless, it appears to be helpful in comparing different CR models. The difference to model [3], discussed in chapter 7.2, may be investigated in this way, too, if the model could be obtained.

7.6 Inverse problem: T_e and n_e from line intensity ratios

The CR model provides line intensity ratios for given T_e and n_e. Ultimately, the diagnostic is applied to obtain electron temperatures and densities from measured line intensity ratios, $R^m_{T_e}$ and $R^m_{n_e}$. Hence, in the experiment, the inverse calculation has to be performed.

More precisely, we have to find T_e and n_e such that $R_{T_e}(T_e, n_e) = R^m_{T_e}$ and $R_{n_e}(T_e, n_e) = R^m_{n_e}$, which is a root finding problem. Similar as in [1], we can also formulate this as a minimizing procedure: the function to be minimized is

$$f(T_e, n_e) = \left(1 - \frac{R^m_{T_e}}{R_{T_e}(T_e, n_e)}\right)^2 + \left(1 - \frac{R^m_{n_e}}{R_{n_e}(T_e, n_e)}\right)^2. \tag{76}$$

Conveniently, the function gives the relative deviation between theory and experiment, providing a measure for the obtained precision. For minimizing, we use the algorithm from the GSL library 'gsl_multimin_fminimizer_nmsimplex2' [23], since it does not require a gradient.

T_e and n_e are the only parameters to be fitted in formulation II when recombination is neglected. In formulation I, the relative meta-stable state densities are additional free parameters (see section 7.4). They can be fitted, too, as in [34]. However, it is not clear whether the fit is unique in the four dimensional parameter space. Instead, a forward calculation in EIRENE can be used, which will be discussed in section 9.3.

Uncertainty propagation in the inverse calculation should involve Bayes' theorem and is significantly more complicated. Commonly, Monte Carlo procedures are applied, see e.g. [35].

8 Thermal He beam simulation with (EMC3-)EIRENE

In this section, the simulation of a helium beam in hydrogen plasma is described and the underlying EIRENE model is introduced briefly. A comprehensive description of EIRENE is given in the manual, available at [7]. The EMC3 (edge Monte Carlo 3D [10]) model is not touched, because we do not consider the effect of the He beam on the plasma in this framework. Hence, EMC3 "only" provides input parameters like T_e, T_i, n_e, n_i on a grid and the vessel geometry.

8.1 EIRENE model

8.1.1 Boltzmann equation

In the EIRENE model, the neutral gas is described by the phase space density function, in short "pdf", $f(\mathbf{r},\mathbf{v},t,s)$: $\mathbf{r}$ is the position vector, $\mathbf{v}$ the velocity vector, t is the time coordinate and s refers to chemical species, including different internal quantum states. It tells us the number of particles of species s in the phase space volume $\mathrm{d}^3r\,\mathrm{d}^3v$ at time t. Let us write $x=(\mathbf{r},\mathbf{v},t,s)$. Observable quantities are "moments" or "responses" of $f(x)$,

$$R =< f|g >= \int \mathrm{d}x f(x)\cdot g(x), \tag{77}$$

with an appropriate detector function $g(x)$. For example, the number density is

$$n_s(\mathrm{r},t) = \int \mathrm{d}^3v f(\mathbf{r},\mathbf{v},t,s). \tag{78}$$

The pdf $f(x)$ can be found by solving the Wang Chang-Uhlenbeck (WCU) equation - a semi-classical Boltzmann-type equation, which includes chemical reactions, particle splitting, absorption etc. It is a linear master equation when allowing collisions only between two disjunct classes of particles: "test" particles and "bulk" or "background" particles. Thereby, the background particle pdf $f_b(x)$ is assumed to be known and remains fixed. The equation for an elastic collision between a single test particle species s and a bulk particle species b is then

$$\begin{aligned} D_t^s f_s(\mathbf{r},\mathbf{v},t) = &\left[\frac{\partial}{\partial t}+\mathbf{v}\cdot\nabla_{\mathbf{r}}+\frac{\mathbf{F}_s(\mathbf{r},\mathbf{v},t)}{m_s}\cdot\nabla_{\mathbf{v}}\right] f_s(\mathbf{r},\mathbf{v},t) = Q_s(\mathbf{r},\mathbf{v},t) \\ &+\int \mathrm{d}^3v' \int \mathrm{d}^3V' \int \mathrm{d}^3V\ \sigma_{sb}(\mathbf{v}',\mathbf{V}'\to\mathbf{v},\mathbf{V})\left|\mathbf{v}'-\mathbf{V}'\right| f_s(\mathbf{v}')f_b(\mathbf{V}') \\ &-\int \mathrm{d}^3v' \int \mathrm{d}^3V' \int \mathrm{d}^3V\ \sigma_{sb}(\mathbf{v},\mathbf{V}\to\mathbf{v}',\mathbf{V}')\left|\mathbf{v}-\mathbf{V}\right| f_s(\mathbf{v})f_b(\mathbf{V}), \end{aligned} \tag{79}$$

with test particle mass m_s, volume force field $\mathbf{F}_s(\mathbf{r},\mathbf{v},t)$ and external source $Q_s(\mathbf{r},\mathbf{v},t)$. The cross section $\sigma_{sb}(\mathbf{v}',\mathbf{V}'\to\mathbf{v},\mathbf{V})$ times $|\mathbf{v}'-\mathbf{V}'|$ is the reaction rate from pre-collision velocities $\mathbf{v}',\mathbf{V}'$ and pre-collision pdf $f_s(\mathbf{v}')f_b(\mathbf{V}')$ into post-collision state. Both cross sections are related via the detailed balance principle. The velocities are further constrained via momentum and energy conservation. For inelastic collisions, usually the species s changes and there is a kinetic energy release or cost. Both types of collisions, elastic and in-elastic, lead to sources for particle, energy and momentum for the bulk species and their distribution f_b (more details in the manual [7]).

The second term on the right hand side, the second row, may be written as

$$\left.\frac{\delta f_s(\mathbf{v})}{\delta t}\right|_{gain} = \int \mathrm{d}^3v'\, C_{sb}(\mathbf{v}'\to\mathbf{v})|\mathbf{v}'|f_s(\mathbf{v}'), \tag{80}$$

with the collision kernel C [7].

In the third term on the right hand side, $f_s(\mathbf{v})$ can be taken out of the integral, allowing us to write the third row as

$$\left.\frac{\delta f_s(\mathbf{v})}{\delta t}\right|_{loss} = \Sigma_t(\mathbf{r},\mathbf{v},\sigma_{sb},f_b)|\mathbf{v}|f_s(\mathbf{v}) =: \Psi(x), \tag{81}$$

with the total macroscopic cross section Σ_t [1/cm], which is the inverse local mean free path.

This allows us to write eq. (79) as

$$\left[\frac{\partial}{\partial t} + \mathbf{v}\cdot\nabla_{\mathbf{r}} + \frac{\mathbf{F}_s(\mathbf{r},\mathbf{v},t)}{m_s}\cdot\nabla_{\mathbf{v}}\right] f_s(\mathbf{r},\mathbf{v},t) + \Sigma_t(\mathbf{r},\mathbf{v},\sigma_{sb},f_b)|\mathbf{v}|f_s(\mathbf{v}) = \int \mathrm{d}^3v'\, C_{sb}(\mathbf{v}'\to\mathbf{v})|\mathbf{v}'|f_s(\mathbf{v}') + Q_s(\mathbf{r},\mathbf{v},t) \tag{82}$$

8.1.2 Transport equation

In the common case, for neutral particles in a fusion edge plasma, $\partial/\partial t = 0$ and $\mathbf{F} = 0$ can be assumed. Then, for the transport flux $\Phi(\mathbf{r},\mathbf{v},s) := |\mathbf{v}|\cdot f(\mathbf{r},\mathbf{v},s)$ we deduce from (82)

$$\frac{\mathbf{v}}{|\mathbf{v}|}\cdot\nabla_{\mathbf{r}}\Phi(\mathbf{r},\mathbf{v},s) + \Sigma_t(\mathbf{r},\mathbf{v},s)\Phi(\mathbf{r},\mathbf{v},s) = Q(\mathbf{r},\mathbf{v},s) + \int \mathrm{d}^3v'\, C(\mathbf{r},s;\mathbf{v}'\to\mathbf{v})\cdot\Phi(\mathbf{r},\mathbf{v}',s). \tag{83}$$

The solution to (83) with the right hand side replaced by a "delta"-point source at $x = (\mathbf{r}',\mathbf{v},s)$ is the Green's function

$$G(\mathbf{v},s;\mathbf{r}'\to\mathbf{r}) = \mathrm{e}^{-\alpha(\mathbf{v},\mathbf{r}',\mathbf{r})}\cdot H(\Omega(\mathbf{r}-\mathbf{r}'))\cdot\delta(\Omega'(\mathbf{r}-\mathbf{r}'))\cdot\delta(\Omega''(\mathbf{r}-\mathbf{r}')), \tag{84}$$

with Heaviside step function H and the optical thickness

$$\alpha(l) = \int_0^{\Omega(\mathbf{r}-\mathbf{r}')} \mathrm{d}l'\,\Sigma_t(\mathbf{r}'+l'\Omega) = \int_0^l \mathrm{d}l'\,\Sigma_t(l'). \tag{85}$$

Here, $\Omega = \mathbf{v}/|\mathbf{v}|$ is the unit vector in the direction of particle flight, Ω' and Ω'' are two further unit vectors such that these three form an ortho-normal basis at $\mathbf{r}'$. l is the distance for a free flight starting from $\mathbf{r}'$ to the next point of collision $\mathbf{r} = \mathbf{r}' + l\Omega$.

Multiplying eq. (83) with G and Σ_t (non-vanishing collisionality, i.e. $\Sigma_t \neq 0$ everywhere, assumed) and integrating over $\mathbf{r}'$ results in the linear non-homogeneous Fredholm integral equation (FIE) of 2nd kind [7] for the (pre-) collision density

$$\Psi(x) = S(x) + \int \mathrm{d}x'\,\Psi(x')\cdot K(x'\to x). \tag{86}$$

The transition kernel K is usually decomposed into a collision- and a transport kernel

$$K(\mathbf{r}',\mathbf{v}',s'\to\mathbf{r},\mathbf{v},s) = C(\mathbf{r}';\mathbf{v}',s'\to\mathbf{v},s)\cdot T(\mathbf{v},s;\mathbf{r}'\to\mathbf{r}). \tag{87}$$

The transport kernel $T(\mathbf{v},s;\mathbf{r}'\to\mathbf{r}) = \Sigma_t(\mathbf{r},\mathbf{v},s)G(\mathbf{v},s;\mathbf{r}'\to\mathbf{r})$ describes the motion of test particles between collision events. In a finite medium,

$$T(l) = \begin{cases} \Sigma_t(l) & \cdot\mathrm{e}^{-\alpha(l)} & \text{, if } l < l_{max} \\ \delta(l-l_{max}) & \cdot\mathrm{e}^{-\alpha(l_{max})} & \text{, if } l \geq l_{max} \end{cases}, \tag{88}$$

with distance l_{max} to the surface at which the test flight shall be stopped, e.g. a cell boundary.

For elastic collisions, the collision kernel contains the new velocity distribution $\mathbf{v}$, given the incident velocity $\mathbf{v}'$. For inelastic collisions, it also contains the new species distribution s, given the incident species s'. It can be further decomposed into

$$C(\mathbf{r}';\mathbf{v}',s' \to \mathbf{v},s) = \sum_k p_k C_k(\mathbf{r}';\mathbf{v}',s' \to \mathbf{v},s),\ p_k = \frac{\Sigma_k}{\Sigma_t}, \tag{89}$$

with p_k defined as the conditional probability for a collision to be of type k. The mean number of secondaries for this collision process is given by

$$c_k(x') = \sum_s \int \mathrm{d}^3 v\, C_k(\mathbf{r}';\mathbf{v}',s' \to \mathbf{v},s). \tag{90}$$

In (86), the inhomogeneity

$$S(x) = \int \mathrm{d}x'\, Q(x') \cdot T(x' \to x) \tag{91}$$

is, excluding normalization, the distribution density of first collisions, whereas the integral term describes the contribution to Ψ from all higher generations.

8.1.3 Solution by the Monte-Carlo method

It is important that $f(x)$ and $\Psi(x)$ can also be interpreted as probability density functions. Hence, $\Psi(x)$ can be found by a Monte-Carlo procedure. A discrete Markov chain with histories $\omega^n = (x_0, x_1, x_2, ..., x_n)$ is generated for each test particle, with x_n being the first state after transition into the absorbing (limbo) state x_a. x_0 is the initial state, sampled from Q. x_1 is sampled from QT. The transition probability for $x_j \to x_{j+1}$ is sampled from $K = C \cdot T$. Machine generated (pseudo-) random numbers are converted into numbers with distributions Q, T and C. The length n of the chain ω^n is a random variable itself. It can be shown [7] that

$$R = \int \mathrm{d}x f(x) \cdot g_f(x) = \int \mathrm{d}x \Psi(x) \cdot g_c(x) \stackrel{!}{=} \int \mathrm{d}(\omega) X_g(\omega) h(\omega) = E(X_g), \tag{92}$$

with $h(\omega)$ being the probability density for finding a chain ω from the Markov process and X_g an estimator for the detector function. The expectation value can now be approximated with

$$E(X_g) \approx \frac{1}{N} \sum_{i=1}^{N} X_g(\omega_i), \tag{93}$$

by computing N test particle histories[†]. A possible choice for $X_g(\omega)$ is the "collision estimator"

$$X_c(\omega_i^n) = \sum_{l=1}^{n} g_c(x_l) \cdot \prod_{j=1}^{l-1} \frac{c(x_j)}{1 - p_a(x_j)}. \tag{94}$$

It evaluates the function g_c at the points of collisions. The factors in the product account for particle absorption and multiplication: $c(x)$ is defined in (90) - the index k is dropped because different types of collisions are possible at different collision points - and $p_a(x)$ is the absorption probability. Other estimators are also employed frequently and are described in the manual [7].

The Monte-Carlo method also provides an obvious estimate of its precision: the empirical variance (valid for large N)

$$s_N^2(X_g) = \frac{1}{N(N-1)} \left(\sum_{i=1}^{N} X_g^2(\omega_i) - \frac{1}{N} \left[\sum_{i=1}^{N} X_g(\omega_i) \right]^2 \right) \approx \sigma^2(X_g). \tag{95}$$

[†]The index i counts test particles. Their species may change during the flight.

8.2 Source specification

An important part of the beam simulation is the specification of the source term $Q(\mathbf{r}, \mathbf{v})$. The geometry of the setup is displayed in Figure 21: helium is injected through one or multiple gas nozzles and observed with the endoscopes, with the goal to reconstruct T_e, n_e at the divertor. While the figure shows the lower divertor, we simulate the beam at the upper one, since helium experiments are performed there [32].

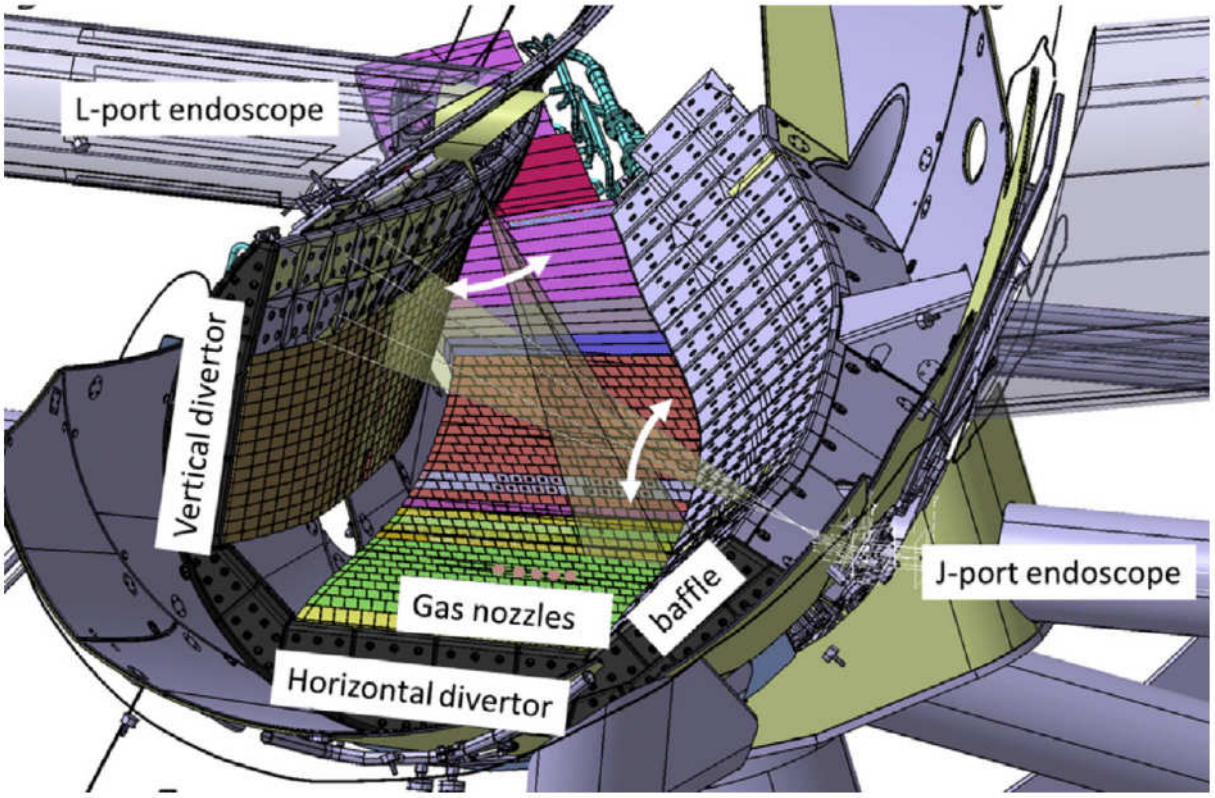

Figure 21: Gas inlets and observation geometry for spectroscopy in a lower divertor. Courtesy: [36].

While the computational implementation is described in part 2.7 of the manual [7] ("input block 7"), the actual experimental parameters are extracted from [32, 37, 38]. These are

- capillary nozzles diameter ∅,
- positions and orientation of the gas nozzles,
- particle flux,
- particle velocity distribution and
- beam angular distribution.

They will be discussed in subsequent sections together with consequential EIRENE input parameters.

8.2.1 Spacial source distribution and particle flux

The diameter of the capillary nozzles is $\varnothing = 0.6$ mm [32], which is smaller than the endoscope camera resolution of ~ 1 mm [36]. Therefore, we describe the He source in EIRENE as a point source, neglecting the uncertainty due to underestimation of initial source size (in mm range).

The location of the valves was obtained from the engineering design of the system [37]: the central nozzle entrance is placed at $\mathbf{r}_\pi = (271.2, -463.8, 101.1)$ cm, with the origin of the coordinates at machine center. The distance between neighboring nozzles is 2.55 cm. The direction of beam propagation is given by the orientation of the capillaries, which is $\hat{e}_\pi = (0.094, -0.144, -0.985)$.

Let us describe the spacial source distribution in commonly used cylindrical coordinates: radial distance from the machine center $R = \sqrt{x^2+y^2}$, toroidal angle φ and height (from machine center) z. The location of the valves then is $R = 537.3$ cm, $\varphi = 300.3°$ and $z = 101.1$ cm.

Notice, that the direction of beam propagation lies in the poloidal plane: the poloidal normal vector is $\hat{e}_\varphi = (-\sin(\varphi), \cos(\varphi), 0) = (0.86, 0.50, 0)$, hence $\hat{e}_\varphi \cdot \hat{e}_\pi = 0.0085$ and the angle between the two is nearly 90°.

Since EMC3-EIRENE only simulates 1/10 of the machine (see chap. 8.4), a map of the gas injection system into the computational domain is necessary. It results in
$\hat{e}_\pi = (0.167, 0.0455, -0.985)$ and $\varphi = 12.32°$.

Note also, that $\mathbf{r}_\pi$ has to be inside the vessel: since no entrance is specified through the divertor, particles would be reflected from it otherwise. The uncertainty in the divertor boundary location and the point source approximation can lead to a slightly outside location of $\mathbf{r}_\pi$. Therefore, it may need to be shifted inside the starting mesh cell, which in the current work is on the order of < 0.5 cm.

The particle flux is set to $\dot{N} = 1.5 \times 10^{19}$ atoms/s according to [32].

8.2.2 Velocity and angular distribution

In the current setup, a thermal He beam is used with a mean velocity of $v_{th} \sim 1.5$ km/s [32]. Unfortunately, to our knowledge, there is no unique definition of a mean velocity for a thermal velocity distribution. We assume, that the commonly encountered relation

$$\frac{3}{2} k_B T_{\mathrm{He}} = \frac{1}{2} m_{\mathrm{He}} v_{th}^2 \tag{96}$$

is meant, hence v_{th} is the root mean square speed of the isotropic Maxwellian distribution. Then, $T_{\mathrm{He}} \approx 0.03$ eV $= 75$ °C, which is close to the operational limit of the valve of 80 °C [38].

Since we want to model the thermal expansion of the gas, an isotropic velocity distribution is not appropriate. Instead, we use the one-sided Maxwellian flux distribution (see manual [7] chap. 1.5.1)

$$\Gamma(\mathbf{v}) = \Gamma(v_1)\Gamma(v_2)\Gamma(v_\pi), \tag{97}$$

$$\Gamma(v_\pi) = \frac{2}{v_T^2} v_\pi \mathrm{e}^{-v_\pi^2/v_T^2},\ v_T = \sqrt{\frac{2k_B T_{\mathrm{He}}}{m_{\mathrm{He}}}},\ v_\pi > 0, \tag{98}$$

$$\Gamma(v_i) = \frac{1}{\sqrt{\pi} v_T} \mathrm{e}^{-v_i^2/v_T^2},\ i \in \{1,2\},\ v_i \in (-\infty, \infty). \tag{99}$$

Here, v_π is the velocity in $\hat{e}_\pi$ direction and $v_{1,2,\pi}$ are orthogonal to each other. Hence, we use the orthonormal basis vectors $\hat{e}_1, \hat{e}_2, \hat{e}_\pi$.

Instead of sampling from $\Gamma(\mathbf{v})$, v_π is obtained from $\Gamma(v_\pi)$ and the polar angle against $\hat{e}_\pi$ is sampled from a Gaussian distribution with zero mean value and standard deviation α. Indeed, according to [38], the gas density perpendicular to the beam axis has a Gaussian distribution with the half angle of beam spread $\alpha \approx 20°$[†]. Physically, the angle is determined by elastic He-He collisions, the capillary width and length.

8.3 Relevant atomic processes

A crucial ingredient in neutral transport modeling is the atomic database: it defines quantitatively the allowed processes for the modeled atoms, molecules, ions and the background species. Hence, it determines the collision kernel C and the total macroscopic cross section Σ_t. The data include interaction potentials, cross sections, reaction rates, population coefficients etc. The EIRENE database (e.g. Amjuel) can be downloaded via the "A&M Data" section at the home page [7] and viewed online at the HYDKIN web page [8].

The default hydrogen model includes the neutral atom H, bulk ion H^+, molecule H_2 and molecular test ion H_2^+. For helium, typically, only the ground state atom He and bulk ion He^+ are tracked explicitly, while other quantum states are coupled to the two implicitly via the effective CR ionization and recombination rate coefficients S_{CR} and α_{CR} from formulation II (see chapter 2.3). Until now, these rate coefficients were obtained in an EIRENE run from the evaluation of double polynomials with coefficients imported from the Amjuel database. The coefficients were obtained through fits from the CR model F1979 [2].

In this work, the newer CR model G2012 [1] is used, with an appropriate treatment of the magnetic field. The ADAS ADF11 table format [26] is used instead of the fits to allow flexible exchange of the data. Contrary to HYDKIN (see chap. 5.2.2), no extrapolation scheme is implemented so far. This remains to be done, referring to chap. 2.5.

Further, it is investigated whether meta-stable helium states must be included explicitly. To allow this, CR coupling coefficients were tabulated. Note that EIRENE expects one input file per reaction - therefore, instead of using the "resolved" ADF11 QCD format for meta-stable cross-coupling coefficients, each coefficient is stored in an own file.

Currently, ionizing plasma is assumed (as typical for the diagnostic), and recombination is neglected. Hence, in form. II the only reaction is ionization. However, in W7-X the diagnostic is applied to the divertor region. In detached conditions, volumetric recombination may become necessary to consider. To allow such studies, both ionization and recombination rate coefficients were tabulated. Since (69) is not necessarily fulfilled, (71) was not incorporated - this allows small discrepancies to the experiment ($< 10\%$ [3]) in the high temperature region ($T_e > 100$ eV), but is better suited for low temperature detachment conditions.

There are, in principle, processes in a He-H plasma apart from those in the considered CR model: charge exchange, formation of molecules, elastic scattering, radiation trapping, quenching etc. Some can be considered irrelevant (for the current experiment), e.g. charge exchange should be negligible due to the low He^+ concentration (charge exchange rates with hydrogen ions are extremely low). Others, e.g. formation of He-H molecules, were not investigated so far. The influence of such processes can be readily studied in future with EIRENE thanks to its

[†]Note: with distance z from source along $\hat{e}_\pi$, the standard deviation of the Gaussian gas density distribution perpendicular to $\hat{e}_\pi$ is $\sigma = z \cdot \tan\alpha / \sqrt{2\ln 2}$ (see [38]).

generic chemistry handling - provided appropriate atomic data are available.

One process which definitely takes place is the elastic scattering of He atoms on protons. It was activated in the current study and is described in the following section. Afterwards, the relevance of radiation trapping and quenching is briefly discussed.

8.3.1 Elastic scattering

The proton pressure close to the divertor is considerable due to their high temperature compared to T_{He}. This leads, depending on p-density or equivalently n_e, to a broadening of the He-beam. Since the inner structure of atoms is not affected by elastic collisions, they do not concern the CR model. Therefore, they can be easily incorporated into the simulation in EIRENE by utilization of the corresponding reaction data from the Amjuel database: interaction potential, cross section and reaction rate. The resulting beam broadening will be discussed in section 9.

8.3.2 Radiation trapping

So far, we have assumed that any radiation emitted by the helium atoms immediately escapes the volume: we have included (spontaneous) radiative decay in the CR model, but no radiative excitation or ionization. Consideration of the latter would require the treatment of the radiation field, coupled to the helium beam, which makes the model and therefore the diagnostic significantly more complex. However, there are indications in the literature that it might be necessary [39, 34]. In the following, we want to estimate the importance of the effect for the current work.

In a homogeneous medium, we could assume a constant absorption coefficient κ. Then, the propagation of radiation through the helium beam for a single mode in one dimension is described by

$$\mathrm{d}I(x) = -\kappa I(x)\mathrm{d}x \quad [11], \tag{100}$$

with the solution

$$I(x) = I_0 \cdot \exp(-\kappa x). \tag{101}$$

The dimensionless quantity $\tau = \kappa x$ is called optical thickness. For a Doppler-broadened transition $p \rightarrow q$ it can be estimated, at the line center, according to [40] by

$$\tau = 5.4 \cdot 10^{-9} f_{pq} \lambda \sqrt{\frac{\mu}{T_{\mathrm{He}}}} n(p) x, \tag{102}$$

with oscillator strength f_{pq}, line center wavelength λ [cm], scaled mass $\mu = m_{\mathrm{He}}/m_p \approx 4$, beam temperature T_{He} [eV], density of the absorbing state $n(p)$ [cm^{-3}] and beam diameter x [cm].

The plasma is called optically thin if $\tau < 1$ [40]. Now let us estimate τ for the current work: re-absorption of photons first becomes relevant for the ground state, since its population is orders of magnitude greater than that of the excited states. With the above specified source and an electron density of $\sim 3 \cdot 10^{13}$ cm^{-3} in front of the limiter ($5 \cdot 10^{13}$ cm^{-3} upstream plasma density), we find $\max(n(1^1S))$=$6 \cdot 10^{13}$ cm^{-3}.

For T_{He} we assume 0.03 eV, the initial beam temperature. Note that the beam is cooled through its expansion and heated by the plasma, and it is not in thermal equilibrium, so that it is difficult to define a correct temperature here.

In following chapters, it will become evident that x is of the order of a few cm. For the transition $1^1S \rightarrow 2^1P$, $f = 0.276$ and $\lambda \approx 60$ nm.

Inserting all this into (102) gives $\tau \approx 6 \cdot x$ [cm] > 1. This shows, that also for the He beam diagnostic at W7-X opacity may already play an important role. Especially, because even higher Helium densities are expected in the experiment at least locally.

This would make the CR model and its application in the experiment much more complex. More quantitative investigations are needed on this topic, like e.g. in [34], to find the correct operational regime. An even better assessment would be possible applying the radiation transport module of EIRENE, which would enable treating resonance radiation line transport explicitly. This lies outside of the scope of the current work, so that opacity was neglected here.

8.3.3 Quenching

By quenching we mean here the coupling of orbital angular momentum states of helium, which would lead to an l-degeneracy. This can be partly due to the spin-orbit coupling, discussed in chapters 2.4 and 4. But additionally, this can also happen due to heavy particle collisions [41].

Heavy particle (proton and deuteron) collisions were discussed in [42] in order to estimate their importance for the CR model [3]. It seemed that the effect on line intensity ratios from a He beam is minor, especially at lower temperatures, and so it was henceforth neglected.

Unfortunately, in an arbitrary plasma, the effect is difficult to account for, since it makes the CR model also dependent on heavy particle density and temperature. Usually, the parameters are only estimated. But, they can be obtained by EMC3-EIRENE, so that with appropriate atomic data for p-He inelastic collisions the effect may be taken into account. This could allow to better quantify quenching for the He CR model. Although it seems to be unimportant for the parameters studied in [42], it may not be negligible in a different parameter range, e.g. at higher densities, or for a different experiment, which one may want to model with EIRENE.

8.4 Background plasma and grid from EMC3

Although the EMC3 model is not touched in this report, its coupling to EIRENE is crucial to provide meaningful plasma profiles in the correct geometry for the He beam simulation. Two coupled EMC3-EIRENE runs in divertor geometry were carried out[†] to provide test cases for the current work: one with $P_{\mathrm{SOL}} = 10$ MW heating power and $\langle n_{\mathrm{e}} \rangle_{\mathrm{LCFS}} = 5 \cdot 10^{13}$ cm^{-3} upstream density (high density case), and one with $P_{\mathrm{SOL}} = 1$ MW and $\langle n_{\mathrm{e}} \rangle_{\mathrm{LCFS}} = 5 \cdot 10^{12}$ cm^{-3} (low density case). The total plasma energy is nearly the same in both cases, so that they mainly differ in the n_{e} profile - see fig. 22. Other parameters, including transport coefficients, are the same as in [28]. This turns out to be a good testbed for formulations I and II of the CR model.

To save computational resources, EMC3-EIRENE does not run on a toroidally periodic grid. Instead, it utilizes the five-fold discrete symmetry of W7-X - "the magnetic field is invariant under rotation around the z-axis by 360°/5=72°" [43]. An additional reduction of the computational domain by a factor 2 is possible due to stellarator symmetry [44]: at the poloidal boundary planes of the 36° domain, particle z-coordinate and $\hat{e}_\varphi$-velocity are mirrored.

[†]Many thanks to Dr. Michael Rack.

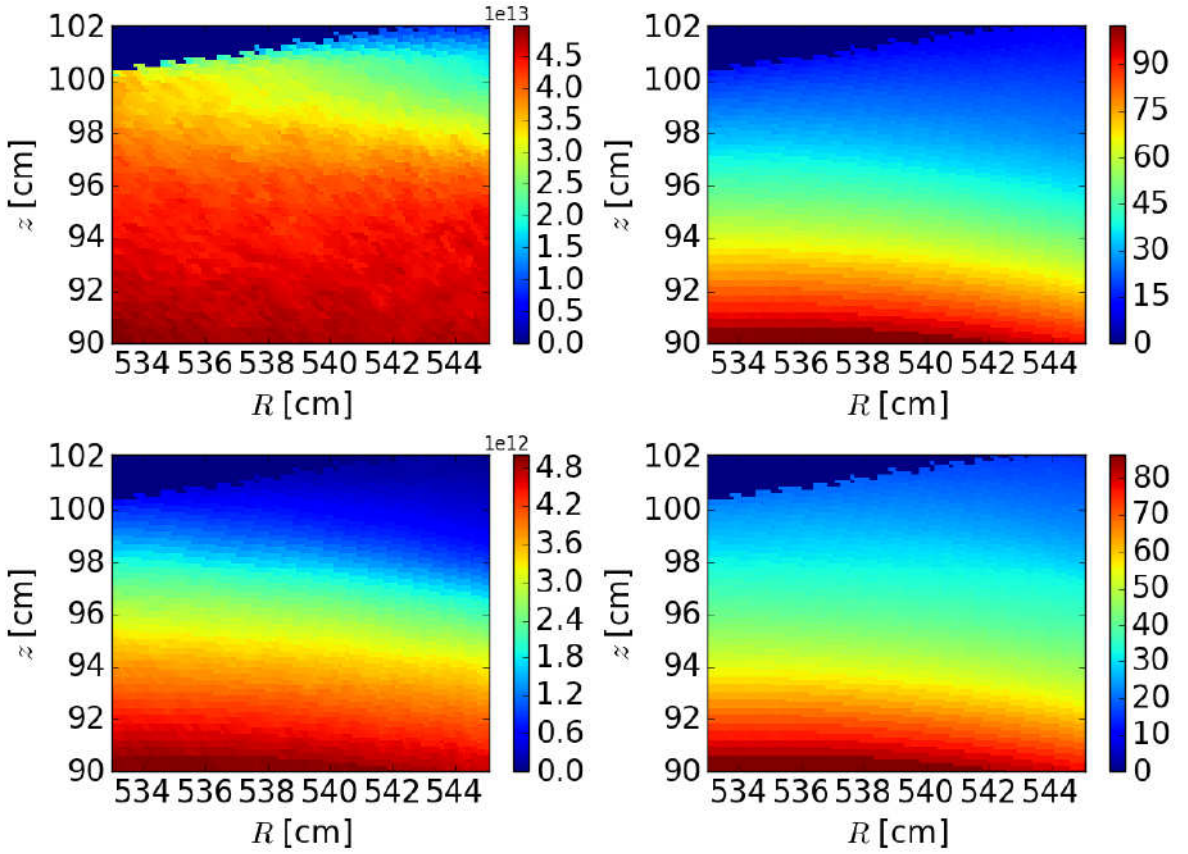

Figure 22: Background plasma parameters in front of the W7-X divertor, in the poloidal plane with $\varphi = 12.32°$. Left - n_e [cm^{-3}], right - T_e [eV]. Top - high density case, bottom - low density case (see text). While the temperature profile remains similar, electron density changes by an order of magnitude. $n_e = T_e = 0$ behind the divertor.

It turns out that grid resolution is a crucial issue for studies like the current one: while 1/10 of the whole machine has to be simulated to find equilibrated plasma profiles, the He diagnostic is applied to a small region and needs locally a fine resolution - the endoscope camera resolution is better than 1 mm according to [36]. This really calls for a local mesh refinement. EMC3 provides such an option through the introduction of different toroidal zones, in which the toroidal grid resolution may vary. However, that solution is not perfect since the He beam is also strongly localized poloidaly. Besides, the application was not possible since EMC3 lies outside of the scope of the current work.

There also exists (in development) an option for this task in EIRENE: each trilinear hexahedron in the EMC3 grid can be devided into six tetrahedra in the EIRENE grid. The resulting mesh could be further refined locally. However, a local refinement in 3D without drastic distortion of the grid is a challenging task and was not undertaken so far. In future, a fine local tetrahedron mesh may be the ideal solution.

A trade off between global grid resolution and run time of the code was made, which led to poloidal resolution of ~ 3 mm and toroidal resolution of $0.5° \approxeq 5$ cm. The toroidal resolution is still very unsatisfying and leads to artifacts, which are discussed later.

Unfortunately, a case with even higher upstream density could not be obtained in satisfying resolution due time. This forces us to postpone the application of the diagnostic to the experimentally important high density case to future work.

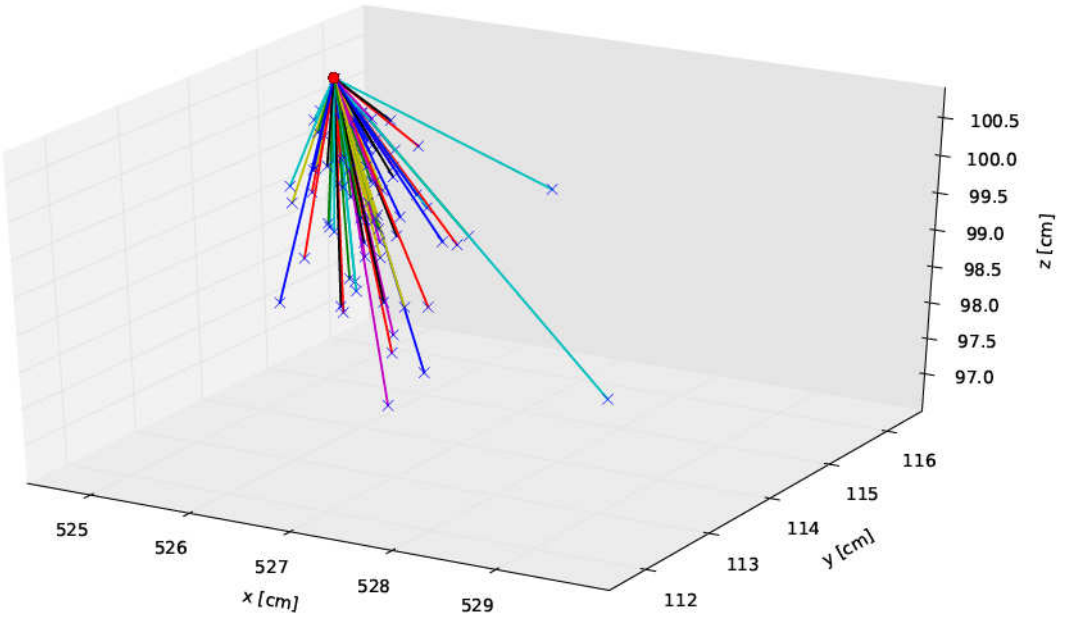

Figure 23: 200 He test particle trajectories in form. II (only ionization). $5 \cdot 10^{13}$ cm^{-3} upstream density, 10 MW heating power case. The red circle marks the nozzle entrance, blue cross - ionization point.

8.5 Resulting test particle trajectories

With the above specified input parameters, Monte-Carlo histories $\omega_i^n = (x_0, ..., x_n)$ can be generated. $i \in [1, N]$ counts test particles. EIRENE provides the option to write out explicitly phase space points along the Markov chain: for arbitrarily many test particles, including coordinates, velocities and species, $x_j = (\mathbf{r}_j, \mathbf{v}_j, s_j)$. The reaction type at any collision point is also given.

This option enables us to check individual steps in the simulation. It also allows us to perform manual statistics on these histories, without the use of estimators.

Note that if the only allowed process is ionization (form. II), the histories are trivial: $n \equiv 1$, $s \equiv \mathrm{He}(1^1S)$, $\mathbf{r}_{i,j=0} \equiv \mathbf{r}_\pi$, $|\mathbf{v}_{i,j=0}| \in \Gamma(v_\pi)$. At $\mathbf{r}_{i,j=1}$, particles are ionized and the history ends.

In Figure 23 trajectories, hence position space coordinates of 150 such MC histories are plotted. While the EMC3 grid is aligned with the magnetic field to simplify charged particle tracking, neutral particles in EIRENE are not influenced by any fields. Therefore, they travel on straight lines between collisions and are simply tracked in 3D Cartesian space, where the origin marks the machine center. The red cross marks the nozzle entrance at the divertor, where the trajectories start. From the mean distance between the red and the blue cross, the mean free path λ can be estimated. Here, it is roughly

$$\lambda = \frac{v_\pi}{n_\mathrm{e} S_\mathrm{CR}}, \tag{103}$$

corrected for the inhomogeneity of n_e and S_CR.

The half angle of beam spread can be estimated by

$$\alpha_\sigma = \sqrt{\frac{1}{N} \sum_{i=1}^{N} \left(\hat{e}_\pi \cdot \frac{\mathbf{r}_{i,n} - \mathbf{r}_{i,0}}{|\mathbf{r}_{i,n} - \mathbf{r}_{i,0}|} \right)^2}, \tag{104}$$

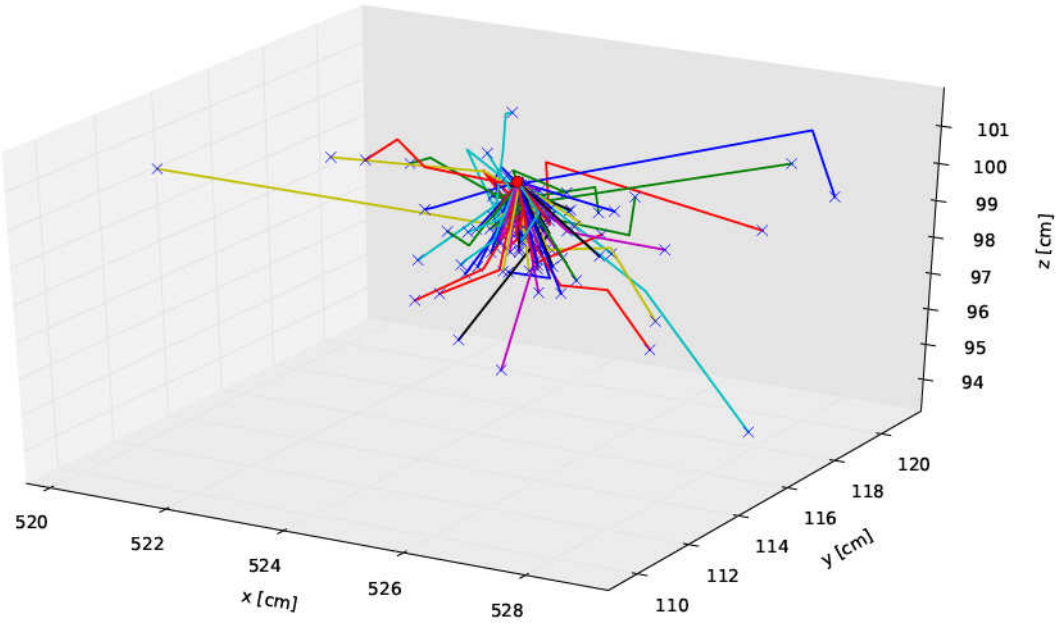

Figure 24: 200 He test particle trajectories in form. II + elastic p-He collisions. $5 \cdot 10^{13}$ cm^{-3} upstream density, 10 MW heating power case. The red circle marks the nozzle entrance, blue cross - ionization point. Note the different scales on the axes compared to fig. 23.

which means we find the standard deviation of individual trajectory angles with mean angle 0. In the case of pure form. II, this obviously corresponds to $\alpha = 20°$. However, elastic collisions noticeably modify α_σ - the corresponding trajectories are depicted in Figure 24 (with different axes than in fig. 23). The effect is rather small in the small density case, there $\alpha_\sigma \approx 24°$. But in the higher density case, $\alpha_\sigma \approx 35°$! This means, the beam is scattered significantly for $n_e > 10^{13}$ cm^{-3}.

For us, the important response, or observable, is the resulting He density in the plasma, since it is needed as input for the emissivity[†]. It is estimated for each grid cell from ω_i^n by tracking the time of flight of particles through them. Hence, although individual MC histories are known very well in real space, some spacial resolution is lost on a too coarse grid.

In formulation II, the only tracked species is He(1^1S), so that $n(1^1S)$ is the helium density. In formulation I, $s_{i,j=0}$ =He(1^1S), but He(2^1S) and He(2^3S) emerge due to electron collisions. We have to distinguish then between ground state and meta-stable densities.

[†]Although line ratios are He density independent in form. II, emissivities of single lines are not.

9 Synthetic spectroscopy

In the course of the present work, the EIRENE post processing diagnostic module, previously limited to hydrogenic species, was extended to treat arbitrary species - provided appropriate atomic data are available. The module will be shortly explained in chapter 9.1. As a possible application, we propose an algorithm for the evaluation of the applicability of the helium beam diagnostic:

1. Simulate the helium beam with EIRENE for a given plasma, including meta-stable states, elastic scattering and other relevant processes.
2. Apply collisional-radiative model to obtain emissivity in 3D.
3. Construct synthetic camera views with line integrals.
4. Reconstruct the plasma parameters from the synthetic views, using an experimentally applicable model.
5. Improve model if necessary.

Step 1 was shown in chapter 8, it already can tell about basic properties of the beam-plasma interaction. Chapter 9.2 demonstrates steps 2 and 3. The third step elucidates the applicability of a given camera set in the 3D geometry. Step 4 is presented in chapter 9.3, but taking a shortcut around step 3 - allowing to separate geometrical factors from the reconstruction process. Hence, we use emissivity ratios instead of intensity ratios. The reconstruction procedure is described in chapter 7.6. It is applied for each pixel individually. Step 5 is left to future work.

Since the full set of electron impact transition cross sections from the R2008 database [4] became available in the CR code only recently, see chapter 3.2.3, V2005 data [18] are used instead here. Although chapter 7.3 points out a significant difference in the application to the experiment, we expect no impact on the results from the present chapter: in contrast to the line intensity ratios, the difference in absolute light intensity between the two models is not as pronounced. And as pointed out in chapter 3.2.3, the reconstruction procedure is not affected either, as long as it is self consistent. In future, usage of the R2008 database is envisaged, for both the synthetic emission evaluation and the plasma parameter reconstruction.

9.1 The synthetic diagnostic module

The synthetic diagnostic module consists mainly of two parts: calculating the 3D emissivity profile and calculating line of sight integrals for the camera view. The starting point is the helium density $n_{\mathrm{He}}(\mathbf{r})$ on the three dimensional grid, obtained via an estimator applied to test particle trajectories. The module's input includes:

- Number and coordinates of the lines of sight. The coordinates are defined through two points in Cartesian space.
- Definition of observed transitions $p \rightarrow q$, including their number, wavelength, Einstein coefficient A and threshold energy ΔE.
- Corresponding data sets for the observed transitions. Here, we use population coefficients[†], tabulated vs density and temperature in a format similar to the ADF11 ADAS format (see chap. 5.2.2).

[†]Note: as input for EIRENE, population coefficients are defined in dimensionless form as ratios $\tilde{R}(p)$ and $\tilde{r}(p)$ of excited state equilibrium density to their "parent" density, i.e., here to the ground state and meta-stable densities, for formulations II and I, respectively

Compared to the extensive intensity (64), emissivity is the related intensive property, given by

$$\varepsilon(\mathbf{r}, p \to q) = n(\mathbf{r}, p) A(p \to q) \tag{105}$$

for a transition $p \to q$. $n(p)$ is the excited state density and A the related Einstein coefficient. The excited state density is given by either formulation I or II (chap. 2.2 or 2.3).

In form. II, neglecting recombination, the emissivity becomes

$$\varepsilon(\mathbf{r}, p \to q) = R_1\left(T_\mathrm{e}(\mathbf{r}), n_\mathrm{e}(\mathbf{r}), p\right) n_\mathrm{e}(\mathbf{r}) n(\mathbf{r}, 1^1S) A(p \to q), \tag{106}$$

and we can associate helium density with ground state density, $n_\mathrm{He} = n(1^1S)$.

More generally, in form. I,

$$\varepsilon(\mathbf{r}, p \to q) = \left(r_1(\mathbf{r}, p) n(1^1S) + r_2(\mathbf{r}, p) n(2^1S) + r_3(\mathbf{r}, p) n(2^3S)\right) n_\mathrm{e}(\mathbf{r}) A(p \to q). \tag{107}$$

Here, we have to distinguish between ground state and meta-stable densities. For the He beam, the recombination term containing the ion density is neglected, so that ionization provides a particle sink. In the EIRENE post processing routines the electron density factors are already contained in coefficients $\tilde{R}$ and $\tilde{r}$ read from its external databases

Then, for isotropic emitters, the light intensity I [photons/s/cm^2/rad] for individual camera pixels is calculated via line integration from the camera postion across the plasma

$$I = \frac{1}{4\pi} \int_{P_1}^{P_2} \mathrm{d}s\, \varepsilon(s) = \frac{1}{4\pi} \sum_k \Delta s_k \varepsilon_k, \tag{108}$$

which is equivalent to summation of emissivities in grid cells k along the line of sight, weighted by the distance Δs_k actually going through the cell. Internally, the sum is evaluated by tracing virtual particles along the line of sight. The same equivalence of line of sight and view cone integrals is also used in [45]. Unfortunately, a satisfactory toroidal grid resolution could not be achieved in the course of this work, limiting the quality of the synthetic diagnostic reconstruction.

9.2 Camera views and emissivity

Using the synthetic diagnostic, we are able to simulate endoscope camera views at the upper divertor for the setup described by O. Neubauer *et al.* [36]. The background plasma was specified in chapter 8.4 and shown in Figure 22.

There is only one horizontal view (meaning perpendicular to the He beam, which starts at the upper divertor plates), through which the helium beams can be observed – M51_J_3535: the camera is located in module 51, port J, and '3535' specifies the angle of the first mirror. A synthetic image of the 706.5 nm line intensity (on a logarithmic scale) is shown in Figure 25. The five 'steps' correspond to beams through five different gas nozzles, injected simultaneously. Due to the low toroidal resolution, grid cells are highly elongated in horizontal direction in the image.

Notice how the emission from different nozzles overlaps in this view. In the experiment, reconstruction of the emission profile is only possible by tomography, with an additional endoscope in the L-port. This procedure can be supplemented by the simulation, where we have the emission profile on the whole 3D grid (although a better grid resolution is desirable). For example,

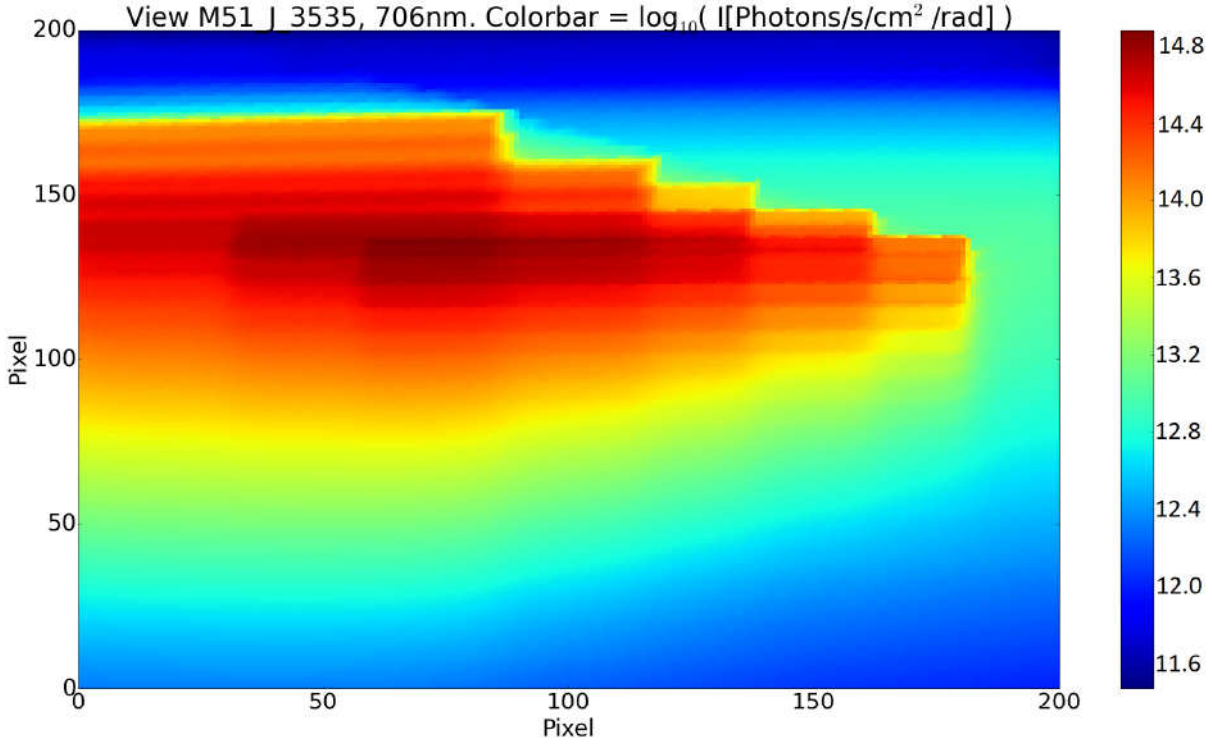

Figure 25: Synthetic image of the 706.5 nm line intensity (logarithm) for the endoscope view M51_J_3535. Background plasma obtained with $P_{\mathrm{SOL}} = 10$ MW and $\langle n_{\mathrm{e}} \rangle_{\mathrm{LCFS}} = 5 \times 10^{13}$ cm^{-3}. Five beams injected simultaneously, p-He elastic scattering included, formulation II, recombination neglected.

the contribution of each grid cell along the line of sight to the intensity of any pixel can be viewed - demonstrated in Figure 26.

However, in the simulation we have even more freedom: unlike in the experiment, we can place the virtual camera at any position in the simulation space - even inside the hot plasma. This allows us to take pictures directly of the emission in the poloidal plane, as demonstrated in Figure 27. There, since we are in the poloidal plane, we can assign physical coordinates to the axes. The divertor is clearly visible, limiting the plasma volume. The five helium beams are now clearly separable, starting at the divertor and propagating into the plasma nearly in parallel.

One possible application of the synthetic diagnostic is to estimate the applicability of the real diagnostic in different plasma scenarios. In the current work, we were able to test it in two cases: high and low density. Figure 28 compares the helium emission in both simulations. From here information can be already extracted: the beam penetration reduces significantly with higher electron density. The exact distance depends on the contrast tolerable in the experiment. Additionally, as calculated in chapter 8.5, the beam becomes rather a cloud at higher density.

Unfortunately, the low toroidal resolution impairs the quility of the pictures: it is the reason for the 'bulkiness' of Figure 28. The beam spreads radially due to toroidal grid cell curvature, which makes further evaluation difficult. Integrated camera views, however, are not the only way to extract information on the helium emission – the 3D emissivity profile can be printed in the output as well. Figure 29 compares the emissivity in the two different density cases. To separate geometrical effects, further analysis is based on poloidal emissivity profiles.

While Figures 25 - 27 used formulation II, Figures 28 and 29 were prepared in formulation I. The difference is not noticeable with the naked eye in synthetic camera (or emissivity) views,

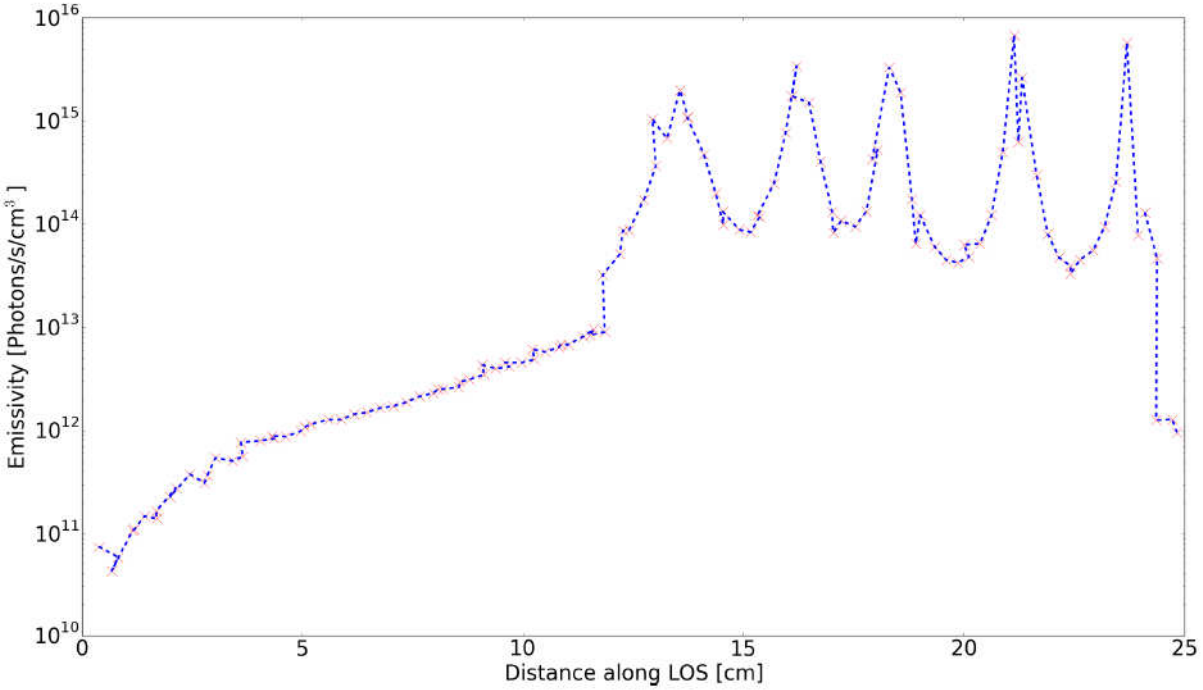

Figure 26: Emissivity profile along the line of sight for a pixel $(i, j) \approx (140, 70)$ in Figure 25, with vertical index i and horizontal index j. Due to memory shortage, the emissivity was obtained in a simulation with only 20×20 pixels instead of 200×200, making an exact comparison between the figures complicated (memory optimization is needed here). Nevertheless, the integral over the profile provides the intensity for a given pixel (in the lower resolution simulation).

but is crucial for correct modeling of the experiment at lower density, as demonstrated in the next chapter. This is the first example of how a forward calculation in EIRENE can supplement the experimental model.

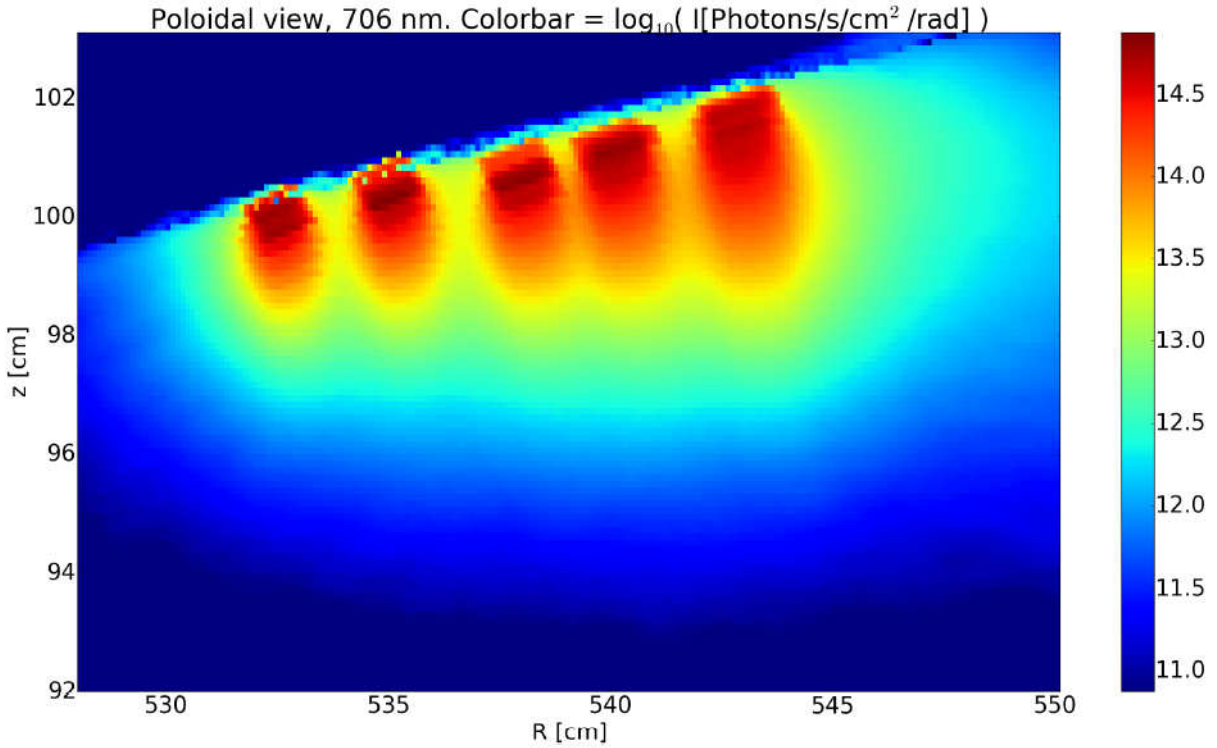

Figure 27: Synthetic image of the 706.5 nm line intensity (logarithm) in the poloidal plane at $\varphi = 12.32°$. Virtual camera is placed 1 m away from the plane. Background plasma obtained with $P_{\mathrm{SOL}} = 10$ MW and $\langle n_{\mathrm{e}} \rangle_{\mathrm{LCFS}} = 5 \times 10^{13}$ cm^{-3}. Five beams, injected simultaneously at the divertor, propagate downwards. p-He elastic scattering included, formulation II, recombination neglected. Here, the total particle flux, for five beams, is the same as for a single beam simulation, unlike in the experiment.

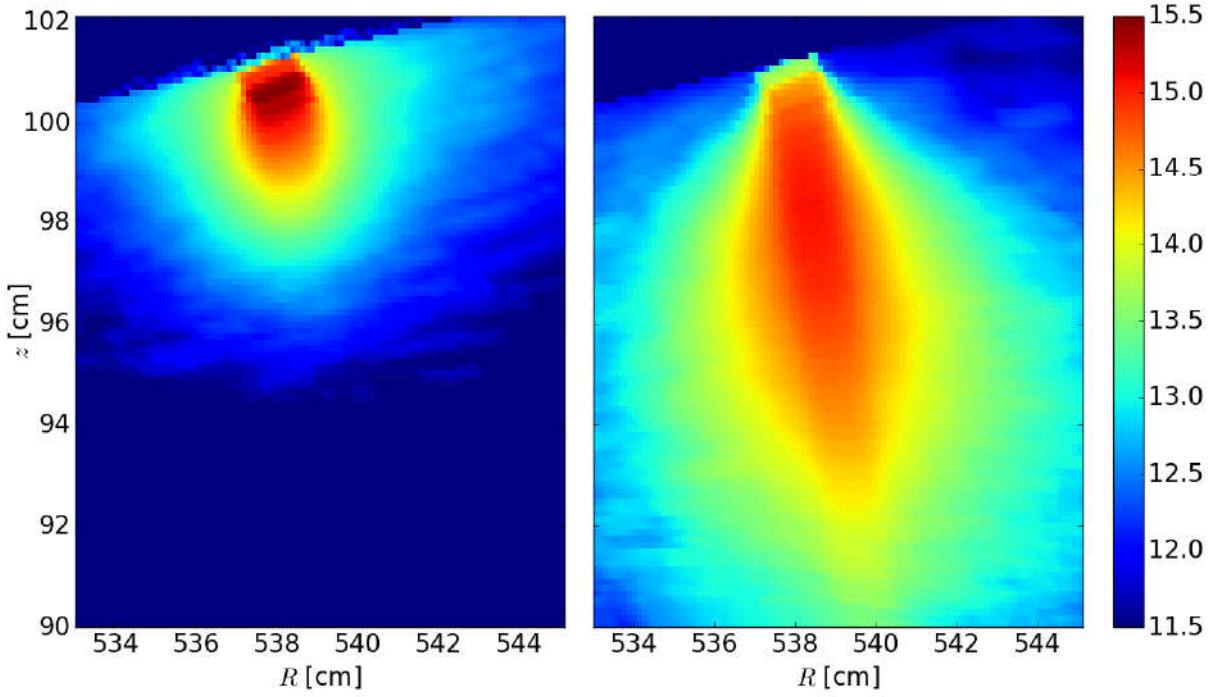

Figure 28: Synthetic image of the 706.5 nm line intensity (decadic logarithm) in the poloidal plane at $\varphi = 12.32°$. Virtual camera is placed 1 m away from the plane. Left - $P_{\mathrm{SOL}} = 10$ MW and $\langle n_{\mathrm{e}} \rangle_{\mathrm{LCFS}} = 5 \times 10^{13}$ cm^{-3}, right - $P_{\mathrm{SOL}} = 1$ MW and $\langle n_{\mathrm{e}} \rangle_{\mathrm{LCFS}} = 5 \times 10^{12}$ cm^{-3}. p-He elastic scattering included, formulation I, recombination neglected.

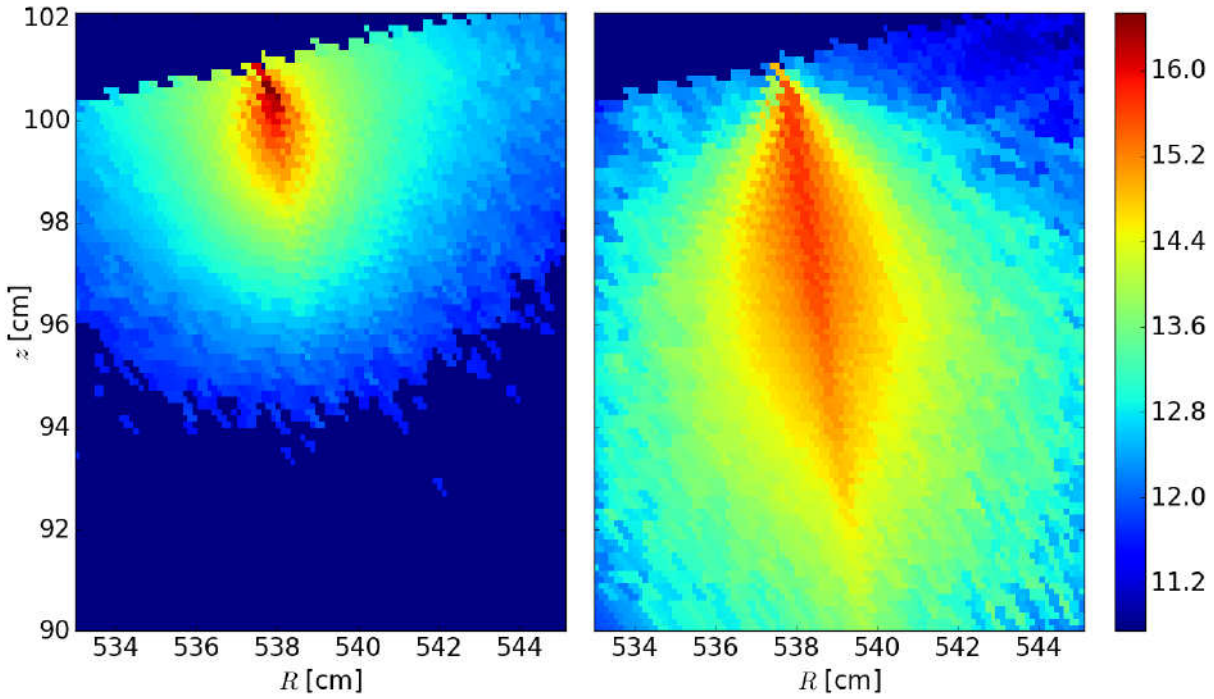

Figure 29: Decadic logarithm of the 706.5 nm line emissivity, $\log_{10}(\varepsilon\ [1/s/cm^3])$, in the same poloidal plane as in fig. 28 and with the same simulation parameters. Contrary to line emission intensity, emissivity is an intrinsic quantity and therefore contains no geometrical effects.

9.3 Reconstruction of T_e and n_e

This chapter demonstrates to what extent the reconstruction of T_e and n_e is possible from measured $R^m_{T_e}$ and $R^m_{n_e}$, according to chapter 7.6. Here, we intend to focus on atomic rather than geometrical effects. Therefore, line intensity I (64) is replaced by emissivity (105) in equations (66) and (67). In other words, the reconstruction is based on Figure 29 instead of 28. To demonstrate the first simple version of the 'diagnostic evaluation algorithm', the forward calculation is performed in formulation I, while reconstruction relies on formulation II. The necessary metastable densities (see chapter 7.4) are available in the forward calculation. The initial plasma profiles are described in chapter 8.4.

The result for the high density case is demonstrated in Figure 30. We focus on the axis in beam direction - the vertical axis. Hence, for the view as in Figure 29 (left), the vertical T_e profile is plotted at $R = 537.85$ cm. The divertor is at $z \gtrsim 101$ cm (the offset in the recovered profile behind the divertor is due to technical reasons and can be easily avoided). Because of a finite penetration depth of the beam, the initial profile can not be recovered where no radiation is emitted - below 94 cm. Otherwise, the reconstruction works well with sufficiently many Monte Carlo test particles in the forward simulation, justifying formulation II here. None of the variance reduction methods in EIRENE are activated in this example. The same is observed for n_e.

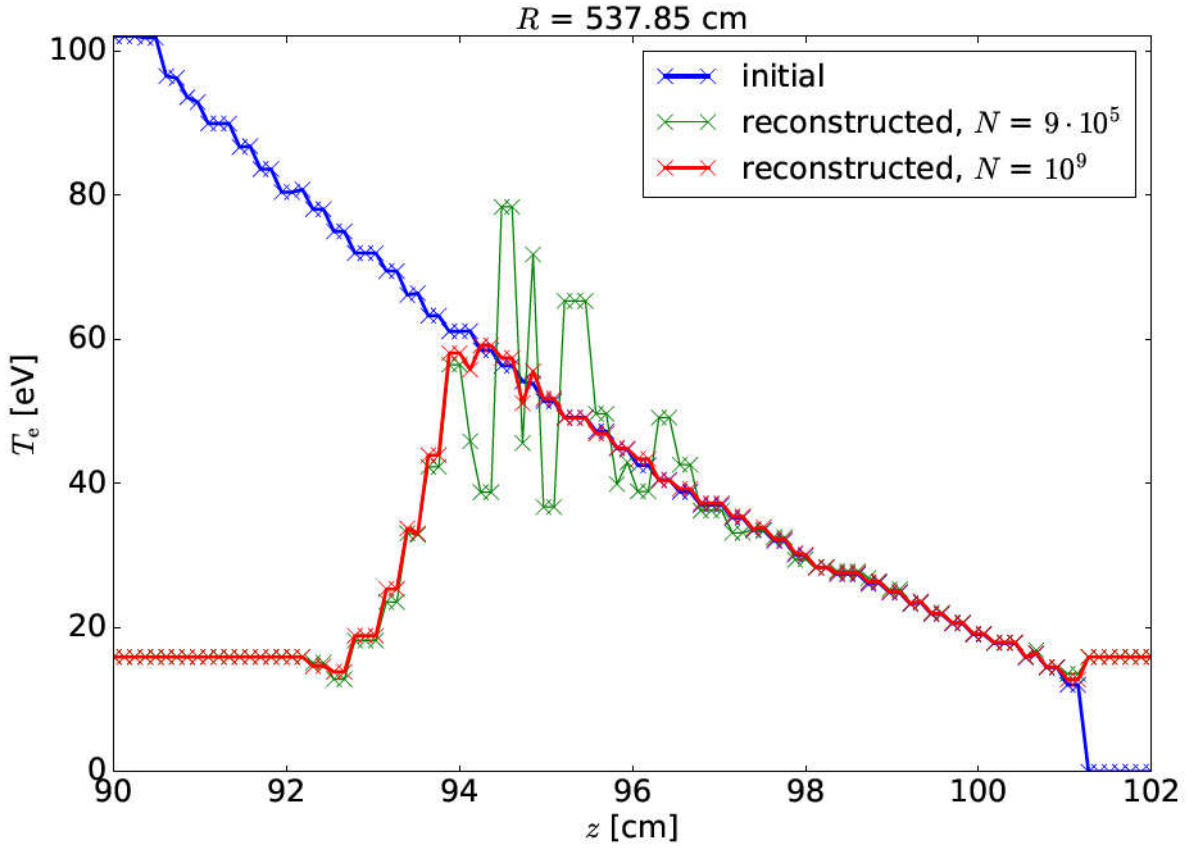

Figure 30: T_e reconstruction (according to chap. 7.6) in the high density case ($P_{SOL} = 10$ MW and $\langle n_e \rangle_{LCFS} = 5 \times 10^{13}$ cm^{-3}) from synthetic He beam diagnostic along vertical axis z (divertor at $\gtrsim 101$ cm). $\varphi \equiv 12.32°$ and radius fixed. N is the number of Monte Carlo test particles in the forward simulation.

However, the number of test particles required for a precise forward calculation of the emissivity - which allows precise reconstruction - is rather high. The computation of 10^9 particle trajectories requires 8 computational hours on a single processor, but that time is reduced sub-

stantially if the code is run in its MPI-parallelized mode. Also conventional variance reduction methods available in EIRENE could drastically reduce N, but this has not be tried here. In contrast, $9 \cdot 10^5$ particles and their emission are computed in a few minutes on a single core. Since the noise in Figure 30 is random, such a simulation can still be used for quick estimates of the emission.

The run time of the synthetic diagnostic itself depends on the number of virtual pixels (lines of sight) rather than test particles. For 100×100 pixels, it takes around three minutes (on a single core). Hence, for pre-computed He densities, additional diagnostic runs can be performed much quicker if separated.

The reconstruction is run for each pixel. For 10^4 pixels, it takes around two hours on a single core until $f < 10^{-8}$ in eq. (76), but only 20 minutes on eight cores.

Coming back to the physical problem: at $n_e > 10^{13}$ cm^{-3}, formulation II suffices. The precise reconstruction indicates that in fact meta-stable states of helium are nearly in equilibrium with the ground state, in the forward transport calculation. The situation is different at $n_e \lesssim 2 \times 10^{12}$ cm^{-3}: as already discussed by Brix [3, chap. 2.5.1], the meta-stable density is significantly different from the CR-equilibrium there. This can be seen in Figure 31: assuming equilibrated meta-stable states in formulation II, electron temperature is overestimated at $z \gtrsim 98$ cm. The effect is significant, since it is independent of the number of MC test particles in the forward calculation. In fact, according to Figure 22, $n_e \lesssim 2 \times 10^{12}$ cm^{-3} at $z \gtrsim 98$ cm. However, n_e can be reconstructed correctly for all z.

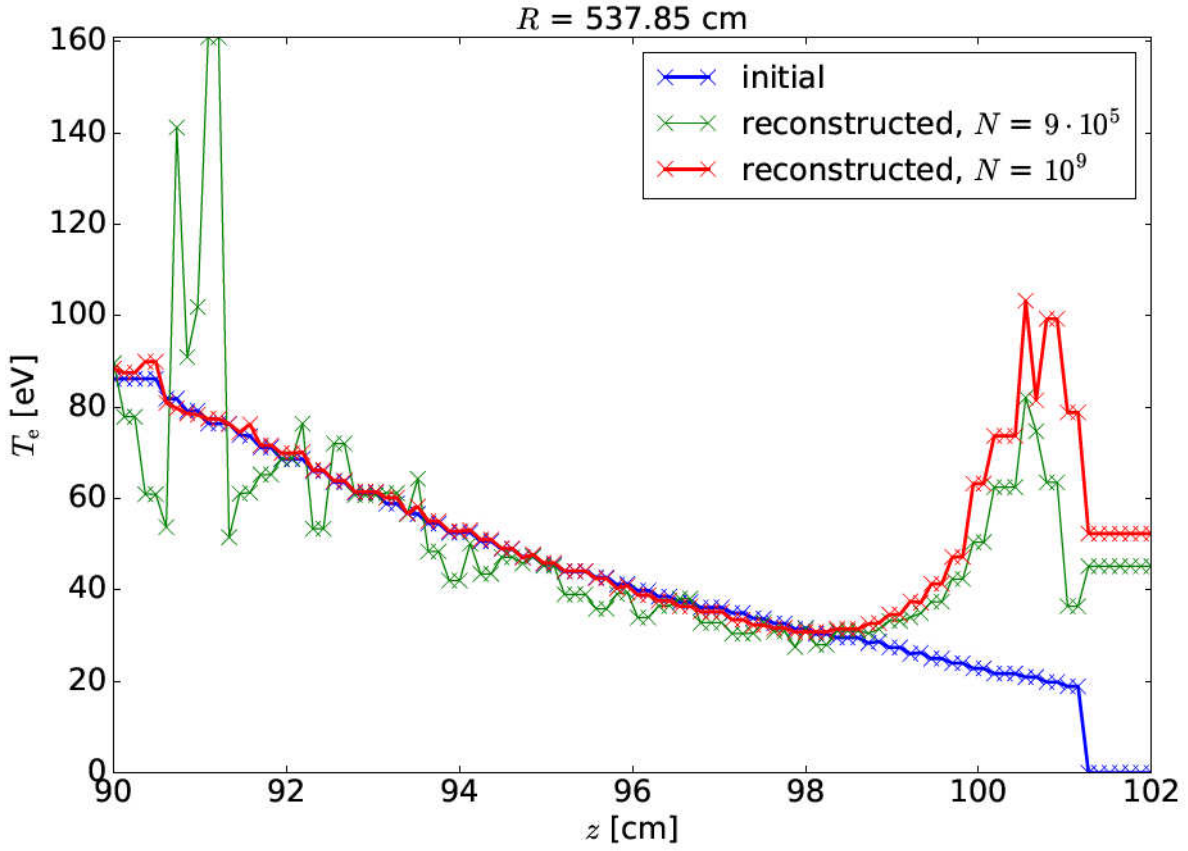

Figure 31: Same as fig. 30, but for the low density case ($P_{SOL} = 1$ MW and $\langle n_e \rangle_{LCFS} = 5 \times 10^{12}$ cm^{-3}).

On the other hand, because of the larger penetration depth, T_e and n_e profiles can be recon-

structed deeper into the plasma. The reconstruction perpendicular to the beam axis is less interesting: it works well with enough test particles, but for low N noise rises significantly with distance from the axis.

9.4 Discussion

In this chapter, we have discussed the extended synthetic diagnostic module in EIRENE and the results which can be obtained with it. In conclusion, the applicability of the He beam was evaluated at all five steps of the suggested algorithm:

1. The beam was simulated using the atomic database implemented in [1]. In fact, we find the explicit inclusion of meta-stable states in formulation I necessary at $n_e \lesssim 2 \times 10^{13}$ cm^{-3}, as also earlier discussed by Brix [3, chap. 2.5.1]. The included elastic p-He scattering allows the estimation of beam divergence. Further inelastic processes, as discussed in chapter 8.3, as well as recombination, may have to be included in future, too – especially for the experimentally interesting maximum density case at $n_e \gtrsim 10^{14}$ cm^{-3}.

2. The 3D emissivity was calculated and can be accessed in the output. We performed reconstruction of plasma parameters (step 4) using emissivity ratios, which allows separation of geometrical and atomic effects. Avoidance of spurious geometrical effects is especially interesting on non-isotropically coarse computational grids: it allows to study atomic beam properties precisely in the poloidal plane while saving resources in toroidal direction.

3. We were able to calculate synthetic endoscope signals as well as poloidal camera views and the corresponding emissivity profiles along lines of sight. This can help with the adjustment of the diagnostic in the experiment, especially for testing of the foreseen tomographic reconstruction. However, for a precise comparison with the experiment, two things must be improved: a finer toroidal grid resolution must be achieved and, for traceability, the full electron impact transition data R2008 [4] must be used. The latter has only recently been achieved, see chapter 3.

4. We have performed the reconstruction of initial plasma parameters from emissivity profiles. While emissivity was calculated in formulation I, formulation II was used for the reconstruction – allowing the study of the equilibration of He meta-stable states. Significant difference is found depending on plasma density: at higher n_e, $\sim 2 \times 10^{13}$ cm^{-3}, the emission is strongly localized close to the divertor. Formulation II is sufficient here. On the other hand, reconstruction of the temperature profile is not possible assuming equilibrated meta-stable states close to the divertor at $n_e \lesssim 2 \times 10^{13}$ cm^{-3}. This implies a shift of the application region depending on plasma density.

5. While improvement of the experimental diagnostic lies outside of the scope of the current work, it was undertaken in [33] and [34] for inclusion of meta-stable states and in [34] for inclusion of radiation trapping. The forward calculation implemented here may be used to verify such elaborate procedures.

   So far, we were not able to analyze the experimentally interesting maximum density case, with $n_e \gtrsim 10^{14}$ cm^{-3} in front of the divertor. This mainly requires a converged steady state plasma solution but poses no challenge to the synthetic diagnostic.

   Since the observed transitions can be freely selected in the code input, the synthetic diagnostic module can be easily extended to other spectral lines – only the corresponding population coefficients have to be stored in a database.

10 Conclusion and outlook

The goal of this work was to develop a numerical simulation of the helium beam diagnostic for the stellarator Wendelstein 7-X and thereby evaluate its experimental application. For this purpose, the collisional-radiative model as implemented by Goto [1] was re-examined and its results – CR coupling and population coefficients – can now be utilized by the EIRENE code, replacing there the earlier Helium CR database by Fujimoto [2]. The synthetic diagnostic module of EIRENE was extended to more general handling of species and transitions, allowing a more flexible post-processing evaluation of spectral emission.

The effective CR coefficients as well as the completely state resolved atomic data have been made accessible at the HYDKIN web page [8], so that they may be compared for various experimental situations. Using the solver at the web page and the dimension reduction tool [29], we were able to reconstruct the solution of G2012 for the meta-stable resolved and unresolved effective CR coefficients from the underlying completely state resolved atomic data. The effective rate coefficients were compared to those already used by EIRENE, produced by the older Fujimoto code [2]. The differences between the two can be traced back to individual atomic transitions with the help of the online linear sensitivity analysis tool of HYDKIN.

We have found significant differences due to newer atomic data, data parametrization (fits vs. tables) and the magnetic field effect. For Wendelstein 7-X, the explicit magnetic field dependence can be omitted: only a correction of the $(T_e, n_e)-$dependent data was required. However, this correction is not sufficient for higher $B-$field machines like ITER.

We were not able to identify a reference for electron impact excitation data in one of the two available atomic datasets (except a private communication [18]). Although the data set V2005 [18] is appealing due to its comprehensiveness, we recommend the usage of R2008 [4] instead. Its full implementation was previously hindered by a combination of poor low energy asymptotic behavior of some fit expressions near threshold and the integration routine. These issues have been overcome, allowing now usage of the complete data set. For comparison, cross sections from both data sets are accessible at HYDKIN [8]. Both data sets were made available for EIRENE by supplementing its external databases.

Throughout this work, we now fully utilize the internationally evaluated data set [4]. Nevertheless, it remains unreliable at very small temperatures due to the poor behavior of some fits at very low energies. Additionally, chapter 7 indicates the importance of higher excited energy eigenstates, for which no evaluated data are available. Hence, the helium atomic data base still shows potential for improvement.

We do not expect a tremendous impact on the overall behavior of helium plasmas and impurities due to the new data in transport simulations, since CR rate coefficients and cooling rates in the condensed formulation II were not substantially affected. Yet, the change in the population density distribution may be crucial for the interpretation of spectroscopic data.

Comparing the CR model by Goto [1] to the one by Brix [3], we find only modest consensus. This is not surprising considering multiple revisions of [3], e.g. [35, 42]. Surprisingly the discrepancy becomes significantly larger if we reduce the number of energy eigenstates in model [1] to those used in [3] – which indicates the relevance of upper excited states. This also questions the empirical adjustment of individual atomic cross sections in the reduced model by Brix [3], which, apparently, empirically compensated the absence of the higher exited states in the

model, at least for certain experimental conditions.

Applying atomic data to the interpretation of beam emission spectroscopy requires multiple approximations. We naturally try to use as little data as possible to make the application fast and transparent. However, the validation of such a reduced model in the experiment is difficult, since the measured plasma is also largely unknown – except if it was measured with other diagnostics. Uncertainty reduction through comparison to other diagnostics was undertaken by [35]. In contrast, with the implementation of the synthetic diagnostic in EIRENE, we at least can verify the consistency in a CR model on a known – simulated – plasma. As a first example, we have demonstrated when it is a valid approximation to assume equilibrated meta-stable states for data interpretation and when this is not the case.

In future, going to detached plasma conditions (high densities), the effect of recombination can be readily studied. A direct implementation of the model in EIRENE (without prior parametrization) is foreseen. This should allow to study the effect of opacity quite explicitly, in contrast to [34], as well as photon reflection at wall surfaces, taking advantage of the existing photon transport module [7]. Given corresponding atomic data, inelastic heavy particle collisions can be studied. Other spectral lines and absolute line intensities (proposed by [35]) can be studied as further options to improve the diagnostic. Additionally, this computational tool might be useful to support the cumbersome alignment of the diagnostic in the experiment at W7-X, which can be especially difficult in a stellarator.

11 References

[1] M. Goto. Collisional-radiative model for neutral helium in plasma revisited. *Journal of Quantitative Spectroscopy and Radiative Transfer*, **76** (3–4), 331 (2003).

[2] T. Fujimoto. A collisional-radiative model for helium and its application to a discharge plasma. *Journal of Quantitative Spectroscopy and Radiative Transfer*, **21** (5), 439 (1979).

[3] M. Brix. *Messung von Elektronentemperatur und -dichte mittels Heliumstrahldiagnostik im Randschicht-plasma eines Tokamaks*. Ph.D. thesis, JÜL-Report 3638, Forschungszentrum Jülich (1999). Revisited in: [42].

[4] Y. Ralchenko, R. Janev, T. Kato *et al.* Electron-impact excitation and ionization cross sections for ground state and excited helium atoms. *Atomic Data and Nuclear Data Tables*, **94** (4), 603 (2008).

[5] B. Schweer, G. Mank, A. Pospieszczyk *et al.* Electron temperature and electron density profiles measured with a thermal He-beam in the plasma boundary of TEXTOR. *Journal of Nuclear Materials*, **196-198**, 174 (1992).

[6] S. Brezinsek, A. Huber, S. Jachmich *et al.* Plasma Edge Diagnostics for TEXTOR. *Fusion Science and Technology*, **47** (2), 209 (2005).

[7] EIRENE. `http://www.eirene.de/`. Last visited on September 24, 2017.

[8] HYDKIN. `http://www.hydkin.de/`. Last visited on September 24, 2017.

[9] D. Reiter, M. Baelmans and P. Börner. The EIRENE and B2-EIRENE Codes. *Fusion Science and Technology*, **47** (2), 172 (2005).

[10] Y. Feng, F. Sardei and J. Kisslinger. 3D fluid modelling of the edge plasma by means of a Monte Carlo technique. *Journal of Nuclear Materials*, **266-269**, 812 (1999).

[11] T. Fujimoto. *Plasma Spectroscopy*. Oxford University Press (2004). ISBN 0 19 8530285.

[12] P. T. Greenland and D. Reiter. Collisional-Radiative Models Re-examined. *Contributions to Plasma Physics*, **38** (1-2), 302 (1998).

[13] G. W. F. Drake and Z.-C. Yan. Energies and relativistic corrections for the Rydberg states of helium: Variational results and asymptotic analysis. *Physical Review A*, **46** (5), 2378 (1992).

[14] J.-J. A. M. van der Mullen. Excitation equilibria in plasmas: a classification. *Physics Reports*, **191** (2-3), 109 (1990).

[15] H. Griem and R. Lovberg. *Plasma Physics*. Methods in Experimental Physics. Elsevier Science (1971). ISBN 9780080859866.

[16] E. Fermi. *Nuclear Physics*. University of Chicago Press (1950).

[17] I. Bray. Convergent close-coupling method for the calculation of electron scattering on hydrogenlike targets. *Phys. Rev. A*, **49**, 1066 (1994).

[18] L. A. Vainshtein. Private communication (2005).

[19] A. J. Dixon, M. F. A. Harrison and A. C. H. Smith. A measurement of the electron impact ionization cross section of helium atoms in metastable states. *Journal of Physics B: Atomic and Molecular Physics*, **9** (15), 2617 (1976).

[20] M. Génévriez, J. J. Jureta, P. Defrance *et al.* Absolute cross section for electron-impact ionization of He($1s2s\,^3S$). *Phys. Rev. A*, **96**, 010701 (2017).

[21] Y. Ralchenko, R. Janev, T. Kato *et al.* Cross section database for collision processes of helium atom with charged particles. 1. Electron impact processes. *NIFS-DATA–59, Japan* (2000).

[22] Y. Ralchenko. Private communication (2017).

[23] M. Galassi, J. Davies, J. Theiler *et al. GNU Scientific Library Reference Manual (3rd Ed.)* (2016). ISBN 0954612078.

[24] R. W. Freund and R. H. W. Hoppe. *Stoer/Bulirsch: Numerische Mathematik 1*. Springer-Verlag GmbH (2007). ISBN 978-3-540-45390-1.

[25] `http://www.mymathlib.com/quadrature/gauss_laguerre.html`. Last visited on November 3, 2017.

[26] OPEN-ADAS. `http://open.adas.ac.uk/`. Last visited on September 24, 2017.

[27] R. W. P. McWhirter and A. G. Hearn. A Calculation of the Instantaneous Population Densities of the Excited Levels of Hydrogen-like Ions in a Plasma. *Proceedings of the Physical Society*, **82** (5), 641 (1963).

[28] M. Rack, D. Reiter, F. Hasenbeck *et al.* A fluid-kinetic approach for 3D plasma edge transport in He plasma. *Nuclear Fusion*, **57** (5), 056011 (2017).

[29] A.-C. Weger. Dimensionsreduktion linearer Differentialgleichungssysteme der Reaktionskinetik. Bachelor Thesis, unpublished (2016). Fachhochschule Aachen.

[30] M. Vaaßen. Sensitivitaetsanalyse an zeitlich instationären linearen Systemen: Propagation von Unsicherheiten in plasmachemischen Modellen. Bachelor Thesis, unpublished (2015). Fachhochschule Aachen.

[31] M. A. Bautista, V. Fivet, P. Quinet *et al.* Uncertainties in Atomic Data and their Propagation through Spectral Models. I. *The Astrophysical Journal*, **770** (1), 15 (2013).

[32] T. Barbui, M. Krychowiak, R. König *et al.* Feasibility of line-ratio spectroscopy on helium and neon as edge diagnostic tool for Wendelstein 7-X. *Review of Scientific Instruments*, **87** (11), 11E554 (2016).

[33] J. M. M. Burgos, O. Schmitz, S. D. Loch *et al.* Hybrid time dependent/independent solution for the He I line ratio temperature and density diagnostic for a thermal helium beam with applications in the scrape-off layer-edge regions in tokamaks. *Physics of Plasmas*, **19** (1), 012501 (2012).

[34] M. Goto and K. Sawada. Determination of electron temperature and density at plasma edge in the Large Helical Device with opacity-incorporated helium collisional-radiative model. *Journal of Quantitative Spectroscopy and Radiative Transfer*, **137**, 23 (2014).

[35] M. Krychowiak, M. Brix, D. Dodt *et al.* Bayesian modelling of a thermal helium beam for measurement of electron density and temperature in the W7-X divertor plasma. *Plasma Physics and Controlled Fusion*, **53** (3), 035019 (2011).

[36] O. Neubauer, W. Biel, G. Czymek *et al.* Diagnostic setup for investigation of plasma wall interactions at Wendelstein 7-X. *Fusion Engineering and Design*, **96**, 891 (2015).

[37] D. Hoeschen. Private communication (20.06.2017).

[38] M. Griener, O. Schmitz, K. Bald *et al.* Fast piezoelectric valve offering controlled gas injection in magnetically confined fusion plasmas for diagnostic and fuelling purposes. *Review of Scientific Instruments*, **88** (3), 033509 (2017).

[39] S. Kajita, N. Ohno, S. Takamura *et al.* Comparison of He I line intensity ratio method and electrostatic probe for electron density and temperature measurements in NAGDIS-II. *Physics of Plasmas*, **13** (1), 013301 (2006).

[40] J. Huba. NRL Plasma Formulary. Washington, DC: Naval Research Laboratory (2016).

[41] O. Marchuk. Private communication (2017).

[42] O. Schmitz, I. L. Beigman, L. A. Vainshtein *et al.* Status of electron temperature and density measurement with beam emission spectroscopy on thermal helium at TEXTOR. *Plasma Physics and Controlled Fusion*, **50** (11), 115004 (2008).

[43] D. Hartmann. Stellarators. *Fusion Science and Technology*, **53** (2T), 44 (2008).

[44] R. Dewar and S. Hudson. Stellarator symmetry. *Physica D: Nonlinear Phenomena*, **112** (1), 275 (1998). Proceedings of the Workshop on Time-Reversal Symmetry in Dynamical Systems.

[45] H. Frerichs, F. Effenberg, O. Schmitz *et al.* Synthetic plasma edge diagnostics for EMC3-EIRENE, highlighted for Wendelstein 7-X. *Review of Scientific Instruments*, **87** (11), 11D441 (2016).

Jül-4407 · Februar 2018
ISSN 0944-2952

Mitglied der Helmholtz-Gemeinschaft